Adjoint Sensitivity Studies of Tropical Cyclone Intensity Measures

By

Zoë A. Brooke Zibton

A dissertation submitted in partial fulfillment of
the requirements for the degree of

Doctor of Philosophy
(Atmospheric and Oceanic Sciences)

at the
UNIVERSITY OF WISCONSIN-MADISON
2022

Date of final oral examination: 04/25/2022

The dissertation is approved by the following members of the Final Oral Committee:
Michael C. Morgan, Professor, Atmospheric and Oceanic Sciences
Gregory Tripoli, Professor, Atmospheric and Oceanic Sciences
Stephanie A. Henderson, Assistant Professor, Atmospheric and Oceanic Sciences
Brett T. Hoover, Adjunct Faculty, Atmospheric and Oceanic Sciences
Christopher Davis, Senior Scientist, National Center for Atmospheric Research

Abstract

Adjoint Sensitivity Studies of Tropical Cyclone Intensity Measures

by Zoë A. Brooke Zibton

An adjoint sensitivity analysis evaluates how small perturbations in a numerical weather prediction model forecast trajectory change a specific aspect of a model forecast state at the trajectory's final time (known as a response function). Provided the selected response function accurately represents the physical property the user is interested in investigating, an adjoint sensitivity study can provide insight into the key dynamical processes influencing the response function. Perturbations to the initial state can be derived from adjoint sensitivities and then integrated forward in time to gain explicit understanding of the processes which evolve to ultimately change the response function.

Areal averaged surface pressure and volume-averaged low-level kinetic energy (KE), and tropical cyclone (TC) vortex associated kinetic energy (VAKE) are considered as response functions measuring TC intensity. Each response function is tested for its appropriateness in representing TC intensity and then the sensitivities of each response function are compared to elucidate key differences across response functions and their impact on the forecast trajectory. The VAKE response function performed more optimally than the KE response function in intensifying the TC by multiple metrics, including sea level pressure and vorticity.

Perturbations to adjoint sensitivities were partitioned to reveal how their distributions influence the response function. While results reveal the largest sensitivities at the initial time are in the lower troposphere, partitioning perturbations derived from these sensitivities into upper and lower tropospheric parts reveals that upper rather than lower tropospheric perturbations lead to a more robust change in TC intensity. This result suggests the existence of a "top-down" pathway for TC intensification. Furthermore, results include the observation that the highest sensitivities to wind are collocated within inertially weak or unstable regions suggesting that TC intensity is most sensitive to wind perturbations in regions of weak inertial stability surrounding the TC.

Acknowledgements

First, I have to say thank you to my advisor Michael, without whom I would not be writing this. Over the years you've provided me support and guidance in research and life. You've pushed me to succeed and reminded me to acknowledge my accomplishments along the way. In addition, you brought levity to a stressful journey with (bad) puns and a drawn-out conversation on whether a hotdog is a sandwich.

To the other members of my committee, I appreciate your thoughtful comments and suggestions that have helped develop my dissertation. Brett, who helped pull me into the world of adjoints, your elegant ability to describe complex ideas is something I strive to attain. Greg, you inspire me to think creatively and challenge the way things have previously been done. Stephanie, your questions make me think deeper and inspire new ideas. Additionally, your guidance outside of my dissertation and teaching, on career and life advice has provided great perspective. Chris, you've provoked me to broaden the scope of my thinking and have provided guidance to make my work more tangible.

I am grateful to have built such a strong community within the AOS Department and campus over both my graduate and undergraduate career. Dr. Dan Vimont, you've been part of this journey since day one. Thank you for teaching me in courses and guiding me through teaching my first course. A PhD within the AOS department is not complete without thanking Pete Pokrandt for not just fixing computer problems but being a kind and caring person who'd let you rant about your day. The High Impact Weather Group - both current and past faculty, staff, and fellow students - your support, advice, and community have been immeasurable. Particularly, past members Dr. Melissa Breeden and Dr. Alex Goldstein, who whether they agreed or not became my go-to's for all sorts of advice. And my past and current lab mates, Craig Oswald, Zhaoxiangrui He, Karimar Ledesma Malanado, and Chen Nuo (plus Alex) - you have made the journey far more interesting and enjoyable. I'm glad to have been part of such a supportive and collaborative group.

I appreciate and need to thank the many people who helped me turn my desire for an AOS mentorship program into a reality. And to Alicia Hoffman for making me feel a little more normal by initiating another new program in the department when we're already too involved. And to my incoming graduate cohort - particularly those who stuck around for their PhDs as we braved higher education during a global pandemic (Juliet, Kelton, Miguel, Julia, Vijit, and Maggie). I am so grateful to have gone through a program with such intelligent, supportive, and kind graduate students who are too many to name. Lastly (but not least), the amazing office staff who have made logistical miracles happen.

I also need to acknowledge my amazing friends and family outside of AOS who have been by my side throughout this journey. Without my friendships, my life would be a lot duller, and I'd be lost. Thanks for taking me out of my head and celebrating both large and small achievements over the years. My number one is my dad, who always makes me feel supported, loved, and intelligent - and can calm my nerves on any stressful day. Thank you for being you and supporting me. My brother, aunts, and uncles - you may not know what I do every day but continue to cheer me on regardless. I also can't forget my pup Eddy - while she can't read this, she has provided me countless moments of joy over the last 2.5 years.

This dissertation is dedicated to my mother. She taught me from a young age to stand up for what I believe in and chase my dreams. Every day I strive to be as bold, caring, and passionate as she was.

This project is possible due to the support from NSF awards: AGS-1851152 and AGS-2114620

Contents

List of Figures

List of Tables

Chapter 1

Introduction

1.1 Overview

Winds, storm surge, and freshwater flooding associated with tropical cyclones (TCs) can result in catastrophic impacts to lives, property, and commerce – particularly for land-falling TCs. Accurate, timely forecasts of these weather systems are necessary to prepare for and mitigate their impacts. Numerical weather prediction (NWP) forecast accuracy of TCs is measured as a comparison of track and intensity forecasts with observations or analyses, and is influenced by a variety of mechanisms, including growth of errors from imperfect initial conditions and evolving errors from imperfect model physics (Rappaport et al., 2009). Because the mechanisms influencing TC track have been well-researched, a consensus has emerged about key steering mechanisms (e.g., Chan 2005). Tropical cyclone track accuracy has improved considerably over the last few decades due to a combination

of better observations and improved data assimilation of those observations (Soden et al. 2001; Burpee et al. 1996; Tuleya and Lord 1996; Aberson and Franklin 1999), improved dynamical models (Kurihara et al., 1998) and an enhanced understanding of physical processes and mechanisms that govern their motion (Wang et al. 1998; Emanuel 1999). Intensity forecasts, however, are influenced by a variety of mechanisms that remain poorly understood, and consequently, there is space for improvement of TC intensity forecasts (e.g.,Wang and Wu 2004; Rappaport et al. 2009; Kaplan et al. 2010; DeMaria 2014). From this need, there has been a renewed focus on forecast intensity change and effective methods for further improvements (e.g., NOAA's Hurricane Forecast Improvement Program; Gall et al. 2013, Marks and Coauthors 2019).

While all TC intensity forecasts are a challenge, TC rapid intensification (RI) is a particularly interesting area of research (Houze, 2010). Tropical cyclone RI is defined as an increase in the maximum sustained winds of a TC of at least 30 knots in a 24-hour period (Kaplan and DeMaria, 2003) or a deepening in pressure of 42 hPa or greater in a 24-hour period (Holiday and Thompson, 1979). Stronger TCs tend to have gone through the process of RI, making their predictability of particular importance (DeMaria and Kaplan, 1999). Furthermore, it is hypothesized that with a warming climate, the likelihood of RI will increase, particularly before landfall (Emanuel, 2017), enhancing the need to better understand RI.

Numerous factors contribute to whether an NWP forecast can accurately capture the observed intensity, including model resolution, model initial and boundary conditions,

model physics and parameterizations, and the representation of the physical processes governing TC development. As model capabilities and computer resources improve, some of the factors can be addressed. Observations are routinely taken to capture the current state of the atmosphere through a variety of observation methods to improve and verify model forecasts. Specific observational field campaigns can be deployed to gather high-quality data for a particular phenomena, which is especially important in data sparse oceanic regions (Majumdar et al., 2011). Targeted observational field campaigns use a variety of techniques to observe specific regions of the atmosphere considered important for the phenomena being studied, which allows for the effective deployment of observing resources. Numerous targeted observation techniques have been applied to plan aircraft reconnaissance missions such as synoptic reasoning (Burpee et al., 1996), ensemble variance (Lorenz and Emanuel 1998; Aberson 2003), ensemble sensitivity (Ancell and Mass 2006; Torn and Hakim 2008; Hakim and Torn 2008; Brown and Hakim 2015), ensemble transform Kalman filter (Majumdar et al., 2002), singular vectors (Pu et al. 1997; Pu and Kalnay 1999), and adjoint sensitivity (Doyle et al., 2014). From these targeted observation campaigns, in addition to routine observations of the atmosphere, it is understood that by better knowing and assimilating the conditions in particular regions of the TC or its environment, improvements can be made to the numerical forecast through small changes to NWP model initial conditions.

1.2 Tropical Cyclone Structure

Favorable environments for TCs to develop and sustain themselves have been identified by Gray (1968): warm sea surface temperatures (greater than 26.5), high moisture content, weak vertical wind shear of the horizontal wind, and in the tropics, but poleward from the equator (between 5° and 20°), such that the planetary vorticity is nonzero. Tropical cyclones are localized vortices with elevated cyclonic potential vorticity (PV) concentrated in the inner core region near the radius of maximum winds (RMW) with large radial gradients (Wang and Wu, 2004). This is considered the primary circulation of the TC. Consistent with thermal wind balance, the low-level circulation decreases vertically, reversing into an anticyclone in the upper troposphere in a well-developed TC. In addition to the primary circulation, the secondary circulation is an in-up-out structure is denoted by inflow near the surface, strong updrafts within the inner core and radial outflow in the upper troposphere and lower stratosphere.

Tropical cyclone outflow (typically between 150-250 hPa) is characterized by low PV, high entropy air moving radially outward from the deep moist convective updrafts of the TC eyewall. The outflow is eventually cooled radiatively (Emanuel, 1986). Within the outflow layer, narrow channels of outward moving air are referred to as "outflow channels" or "outflow jets" (Merrill and Velden, 1996). A robust outflow supports the intensification of a TC, as mass must be evacuated from the surface low to maintain or deepen the low pressure system (Barrett et al., 2016). The inertial stability within the outflow layer dictates how expansive the outflow can be, as weak inertial stability implies

an imbalance of the Coriolis, horizontal centrifugal, and horizontal pressure gradient forces allowing outflow to accelerate more freely away from the storm core (Rappin et al., 2011). Strong inertial stability results in the outflow performing work against the ambient environment, which is resistant to change, out to the Rossby radius of deformation. The inertial stability on an isentropic surface, can be defined from Petterssen (1953):

$$I_p^2 = \frac{1}{2}\left[(\zeta_\theta + f)^2 - D_\theta^2\right] \tag{1.1}$$

where I_p^2 is the inertial stability, f is the planetary vorticity, ζ_θ is the relative vorticity on an isentropic surface, and D_θ is the total deformation on an isentropic surface. For a given latitude and isentropic surface, the sign of inertial stability can be interpreted as a balance between the magnitude of the relative vorticity and total deformation. For example, around the TC in the lower troposphere, I_p^2 is characterized by high inertial stability in the core decreasing rapidly outward, due to the radial decay of the strong cyclonic vortex. As the vortex decays, the flow becomes dominated by low-level deformation resulting in low inertial stability (Fig 1.1). Outside of the TC, the ambient environment's inertial stability is weakly positive. In the upper troposphere, surrounding a TC with a developed, anticyclonic outflow, circulation can be characterized by weak and typically asymmetrical inertial stability. The asymmetric, weak I_p^2 in the outflow identifies optimal regions for mass evacuations from the TC. The work expended on the environment reduces the kinetic energy available to overcome frictional dissipation in the inflow, consistent with the finding in Merrill (1988) that the azimuthal mean radial outflow is stronger for

intensifying TCs relative to steady or weakening ones. As TCs develop and intensify, they interact with their environment (e.g., Wu and Cheng 1999). Tropical cyclones in the Atlantic are particularly prone to interact with synoptic scale features, such as interactions with an upper-tropospheric trough that enhances the outflow jet leading to more enhanced convection of the inner core TC (Holland and Merrill, 1984).

As TCs mature, they come into gradient balance establishing a relationship between the central pressure and the near surface wind speed above the boundary layer(Emanuel, 1986). Traditionally, either of these two metrics is used to denote TC intensity, with implications for how much damage to property and life is expected of the storm were it to make landfall. However, the physical understanding that links together the wind speed and central pressure has been limited, leaving questions for their interchangeable use. Chavas et al. (2017) explored this relationship and found that discrepancies in comparing these two metrics are due to the fact that surface wind speed does not account for storm size; central pressure is a better measure for capturing intensity, as it is fundamentally an integrated measure of maximum wind speed and storm size. Central pressure thus is a better intensity metric, if the need is to indicate hazards associated with the TC.

Tropical cyclone intensity is historically defined by the strength of surface winds and/or the minimum central pressure of the storm by the National Hurricane Center (Rappaport et al., 2009). Holland and Merrill (1984) defined a TC's strength as the magnitude of the cyclonic circulation in the region outside the inner core. A TC's intensity can

also be defined by the strength of the overturning thermal circulation, as typically represented through the conceptual model of the Carnot Cycle (Emanuel, 1986). Denoted as a secondary circulation to the TC, there are four legs of the circulation (1) surface inflow toward the TC core representing diabatic expansion, (2) upward mass transport and initial outward expansion, representing moist adiabatic expansion, (3) diabatic compression and subsidence forced by radiational cooling, and (4) moist adiabatic subsidence. Through this circulation, energy from the ocean is transported into the upper troposphere and lower stratosphere; the extracted energy from the Carnot heat engine goes into the rotational component of the TC, which is the primary swirling rotation about the core (Emanuel, 1986). The conversation surrounding how to define a TC's intensity, or potential intensity, has been a long-established conversation that has limited discussion of the physical understanding that links the different definitions (Chavas et al., 2017). Furthermore, discussions in the TC community have considered the intensity through the context of its impacts (e.g., storm surge, flooding) as those metrics may be more directly understandable to populations impacted by landfalling TCs.

1.3 History of TC Intensity Prediction

Tropical cyclone model forecasts by both dynamical and statistical models add understanding to how TCs form and maintain their intensity. The first dynamical model of a tropical cyclone was a simple axisymmetic model, which included moist processes (Ooyama, 1969). The purpose of this model was to complement the existing observational knowledge of TCs using three homogenous layers of air that represent the upper and lower

troposphere and a shallow boundary layer. Anthes (1972) developed a three-dimensional numerical model of tropical cyclones, noting that while two-dimensional models have been successful, a three-dimensional model can include effects of asymmetry and how the movement (track) influences the development. Foci of model development include the improvement of horizontal grid spacing, by using grid staggering, an explicit water vapor cycle, and a formulation of the horizontal diffusion processes. These additions allow for the study of the hurricane's water vapor budget and the simulation of non-convective latent heat release, resulting in a more realistic horizontal diffusion of heat, water vapor, and momentum. Asymmetries in the outflow layer also are shown in three-dimensional models to result from dynamical instabilities, with the source of eddy kinetic energy being the mean azimuthal flow.

The first application of statistical models to predict hurricane intensity using forecast data is the Statistical Hurricane Intensity Prediction Scheme (SHIPS; DeMaria and Kaplan 1994). The SHIPS prediction is derived for predicting intensity change at lead-times of 12, 24, 36, 48, and 72 hours using a standard multiple linear regression relating climatology, persistence, and synoptic predictors. This contrasts with earlier versions of statistical models that solely rely on the relationship between climatology and/or persistence. The predictors used in early applications of SHIPS were the difference between current intensity and an estimate of the maximum potential intensity (MPI; Emanuel 1988) based on sea surface temperatures (SSTs), the vertical wind shear of the horizontal winds, current intensity, and the eddy momentum flux convergence at 200 hPa, which provides a measure for whether the large scale environment is acting to increase or decrease the azimuthally

averaged tangential wind of the storm. Additional predictors included information such as date of year, distance to land, and initial latitude and longitude. The model was tested using a jackknife procedure, where regression coefficients are determined with all the forecasts for each storm removed from the sample. Compared to applications of statistical models that only used climatology and persistence (SHIFOR; Statistical Hurricane Intensity FORecast), SHIPS reduced intensity errors by 10-15% and error differences were statistically significant at all forecast times. However, the forecast only explains 50% of the variability of the observed intensity change. Likely this can be attributed to the lack of mesoscale features included (i.e. concentric eyewalls) and that SSTs are assessed using climatology. The application of SHIPS has evolved to include versions that model decay after landfall (e.g.,Kaplan and DeMaria 1995; Kaplan and DeMaria 2001).

The SHIPS – Rapid Intensity Index (RII) was developed from the initial SHIPS technique, with the aim to predict the probability of RI (Kaplan and DeMaria 2003; Kaplan et al. 2010; Kaplan et al. 2015). In the first implementation of SHIPS-RII (Kaplan and DeMaria, 2003), sixteen predictors are used, including location, date, large scale environmental variables, and persistence to forecast the probability of RI occurring. The large-scale environmental variables are averaged within a near proximity of the cyclone (e.g., r = 200-800 km, r<= 1000 km) and include: sea surface temperature, 850-200 hPa vertical shear, 200 hPa zonal wind, 200 hPa temperature, 850-700 hPa relative humidity, 850 hPa relative vorticity, 200 hPa eddy angular momentum flux convergence, and the pressure of the center of mass layer for which the environmental winds best match the current storm motion. As observations, understanding, and tools have progressed,

the list of predictors has expanded, notably including assimilated satellite data such as brightness temperatures (Kaplan et al. 2010; Kaplan et al. 2015). It has been found that RI guidance could be made for different thresholds and forecast periods to provide more targeted RI information (Demaria et al., 2021). For each ocean basin specific set of predictors and weights are assigned, as each basin has unique attributes for TC development. Onderlinde and DeMaria (2018) developed a new tool for RI prediction the Deterministic to Probabilistic Statistical Model (DTOPS), which uses forecast guidance from five models that are frequently used in tropical cyclone forecasting: European Centre for Medium-Range Weather Forecasts (ECMWF), Global Forecast System (GFS), Hurricane Weather and Research Forecasting (HWRF), Logistic Growth Equation Model (LGEM), and SHIPS. The intensity forecast change from these models, in addition to geographic or multi-model information about the storm are compiled in a list of Atlantic and East Pacific basin specific cases from 2011-2017. This information was compared with Best Track intensity change and used binomial logistic regression to calculate the regression coefficients for each model or parameter. These coefficients are inputted into a multi-model regression prediction scheme (Onderlinde and DeMaria, 2018).

1.4 Sensitivity studies of TC intensity

The *sensitivity* of a numerical weather forecast defines how potential changes to model configuration or the initial and boundary conditions influence the model forecast state ($\mathbf{x}$) at later times. Initial condition sensitivity analysis is an objective method to evaluate how changes to the initial conditions affect a later forecast, such as the TC intensity.

Two of the leading methods of sensitivity techniques involve the use of adjoint and ensemble sensitivity. An adjoint sensitivity study involves the evaluation of how ***any*** small changes in a forecast trajectory change a specific aspect (e.g., the response function) of a model forecast state at all times prior to the time the response function is defined (Errico, 1997). This makes the adjoint model forecast sensitivity evaluation efficient *for a given response function*. The adjoint will be discussed in more detail in Chapter 2.

Ensemble sensitivity analysis (ESA) involves the use of a collection of model forecasts, chosen to sample the probability density function of the model state (Ancell and Mass 2006; Hakim and Torn 2008). The collection of forecasts differ by slight changes to initial conditions or model configuration. Ensemble sensitivity is calculated from the of the ensemble mean response function with the state vector for each ensemble member divided by the variance of the state vector, resulting in a linear relationship between the response function and initial conditions (Ancell and Mass 2006; Torn and Hakim 2008; Hakim and Torn 2008). Ancell and Mass (2006) calculated that adjoint and ensemble-based sensitivity analysis are equal when the initial degrees of freedom are uncorrelated, such that individual points may be considered independently. However, this never happens in reality as it is too computationally expensive to create that many ensemble members, thus the ensemble sensitivity is the projection of the analysis error covariance matrix onto the adjoint sensitivity field divided by the variance (Ancell and Mass, 2006). In their study, Ancell and Mass (2006) noted that ensemble sensitivities were typically synoptic scale, tropospheric-deep structures, that tilt modestly up-shear, and found near major synoptic

features, while adjoint sensitivities are predominantly small-scale, localized, and in the lower troposphere, with large, up-shear, vertical tilts.

The size an ensemble is limited by computational cost, leading to a potential drawback in using ESA, as insufficient sampling of the phase space of the model may result in spurious correlations that make the resulting sensitivities non-physical (e.g., "correlation is not causation"), meaning correlations may not have any dynamical significance (Hakim and Torn 2008; Gombos et al. 2012). A high percentage of significantly sensitive cases indicate that a predictable relationship truly exists in the data that is not an artifact of the ensemble sampling. Adjoint techniques allow for the evaluation of the sensitivity of a single variable (e.g., the sensitivity of intensity to the meridional wind) and evolve a perturbation of that variable alone without reference to changes in other variables. A benefit of using adjoint-based techniques, rather than ensemble-based techniques includes the computational cost of running a large number of ensemble members, as, when configuring an ensemble, the user does not know *a priori* the necessary size of an ensemble – making this selection subjective. The calculation of ensemble sensitivities must ensure the members properly simulate the growth of initial uncertainty due to chaos within their solution while also accounting for substantial uncertainty (and error) due to model imperfections or simplifications, the latter is also a requirement for adjoint techniques. This can be especially computationally expensive to determine systematic biases to your prediction system. A benefit of the ensemble approach is the lack of reliance on linearity constraints present in adjoint sensitivity studies (Ancell and Mass, 2006), as an adjoint model is defined as the transpose of the tangent linear model (Errico, 1997). While the

linear constraint does impact an adjoint study's configuration, it is possible through careful considerations of resolution, duration, and parameterizations to avoid breaking this tangent linear assumption (e.g., Errico 1997; Doyle et al. 2012). Methods to address these constraints are in addressed in the next chapter.

Another benefit of using adjoint rather than ensemble sensitivity is the potential for "forecast fracture", where model solutions from consecutive runs valid at the same time vary considerably (Sanders, 1992). Too much spread in the ensemble variance can result in poor performance of the evolved initial perturbations to change the response function (Hakim and Torn, 2008). This can result in ESA studies selecting ensemble members that perform well to ensure the correlations are not degraded (Chang et al., 2013). Adjoint sensitivity studies do not give multi-modal solutions since its calculation involves the use of a single nonlinear forecast trajectory; as a consequence there is no need for the statistics to converge to ensure a robustness of results. If there were fractures in the ensemble that has two or more fundamentally different forecast scenarios (as measured by the response function), the mean of the ensemble can be limited in its usefulness (Chang et al., 2013). Using an adjoint, one could test the potential of model fracture by applying an iterative technique of making multiple small perturbations to the initial state to see how small nudges in either direction (i.e., to strengthen/weaken the system) could result in changes to the forecast (Goldstein, 2018). This can give instructive information about the envelope of predictability, and whether there is a tendency/higher likelihood that the storm would intensify or weaken.

There are few studies using adjoint sensitivity diagnostics applied to TC intensity. Ito et al. (2011) used adjoint sensitivity in a cloud-permitting, non-hydrostatic, axisymmetric model to examine the sensitivity of 1hr intensity forecasts for a mature TC to heat flux and surface wind stress. They found at this short timescale, both stronger near surface friction and a reduction in moist air supply in the exterior region of the TC can serve to strengthen the tangential velocity. Chu et al. (2011) used the Weather Research and Forecasting (WRF) model and its adjoint to apply adjoint sensitivity techniques to a TC that had undergone rapid intensification (RI), finding low-level moisture exerts a strong influence on the final time forecast intensity. These sensitivities to moisture were verified by perturbing and evolving the areas of sensitivity with assimilated idealized observations. Doyle et al. (2012) used the Coupled Ocean-Atmosphere Mesoscale Predication System and its adjoint to address the role of initial state wind, temperature, and moisture perturbations on tropical cyclogenesis in a developing and non-developing case. Adjoint diagnostics identified low-level moisture and temperature perturbations were of greater importance than perturbations to the wind fields, and through perturbing the initial conditions found a "bottom up" development process occurred. He (2018) the WRF model and its adjoint, initiated with a surface pressure response function to evaluate the initial condition sensitivity. The analysis found low-level sensitivities were the most important for development, with a "bottom up" process occurring as in Doyle et al. (2012). The TC intensity was more sensitive to the primary than secondary component of the horizontal wind fields, as well as strongly sensitive to low-level potential temperature and water vapor.

The breadth of previous studies is limited in the number and type (RI or non-RI TC) of cases studied and diagnostic tools applied. With the exception of Doyle et al. (2012), most studies consider a single metric to define intensity. Furthermore, the justification for how the response function was selected is limited in how it best describes TC intensity in previous studies. When using an adjoint model, there will always be "an answer", however, whether that answer has any relevance to your question is not certain. This results in the need to carefully consider the response function used to initiate the adjoint model in order to ensure the answer will be relevant. Doyle et al. (2019) performed a study of extratropical cyclone "Desmond" that evaluated adjoint sensitivities using multiple response functions for different aspects of the storm, not intending to measure the same characteristic, to understand limitations to predictability on high-impact cyclones. Results showed regions of overlap and juxtaposition of sensitivities across response functions, highlighting the importance of carefully defining the forecast aspect of interest for adjoint model sensitivity.

1.5 Research Questions

This work investigates of how perturbations designed to intensify a TC influence the physical processes that lead ultimately to intensification and compares how those perturbations and processes change based on various definitions of intensity. The investigations and comparisons will be assessed by analyzing the dynamical and thermodynamical evolution of adjoint-informed perturbations designed to elicit TC intensification. Ultimately,

this work intends to aid in the understanding of the various pathways to TC intensification. These objectives will be addressed using a case study approach informed by computing the adjoint sensitivities of TC intensity measures to the initial conditions of NWP model simulations and diagnosing and describing the subsequent evolution of the perturbed forecast.

The research questions (RQs) to be considered include:

RQ1: How does the sensitivity of various TC intensity measures change based on the definition of TC intensity?

RQ2: What is the relationship between pressure and wind based TC intensity measures (i.e., are decreases in (average) minimum sea level pressure necessarily associated with increases in maximum low-level winds and/or relative vorticity?)

RQ3: What is the role of upper tropospheric processes on TC intensity change?

To address these research questions, this study will investigate the evolution of adjoint-derived perturbations to the model initial state using the Weather Research and Forecasting (WRF) model (Skamarock and Coauthors, 2008) and its adjoint (Zhang et al., 2013). The foundational approach to answer the research questions will use the "sensitivity-perturbation-response-diagnosis" (SPRD) procedure, which employs adjoint-derived sensitivities to elicit particular responses in the tropical cyclone simulation for which diagnoses of the perturbed cyclone development can be conducted. Chapter 2 contains the technical approach used to address the RQs. Chapter 3 through Chapter 5 address each

the RQs. Chapter 6 synthesizes the results of these studies and discusses future directions and applications of this research.

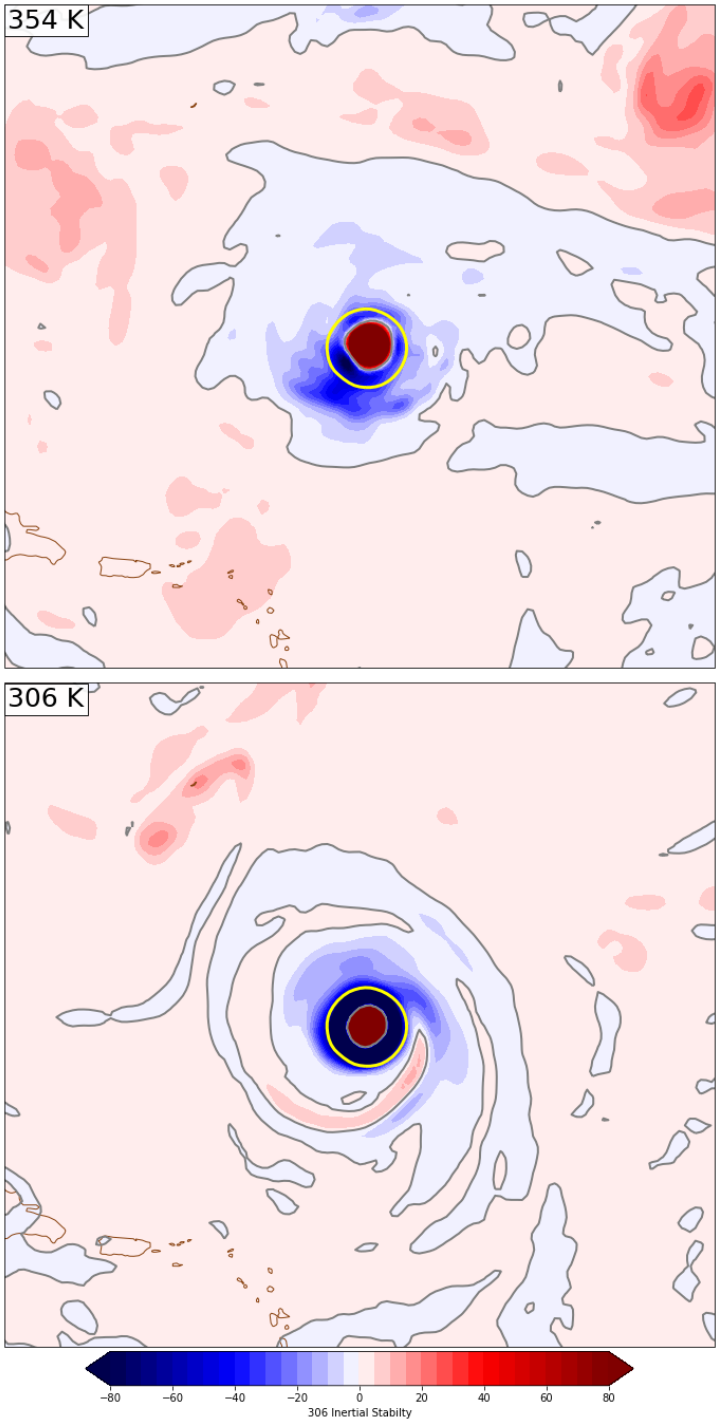

FIGURE 1.1: Simulated inertial stability on 354 K and 306 K isentropic surface (fill; $5\text{x}10^{9}$ s^{-2}), zero line of inertial stability (grey), and the 1004 hPa sea level pressure contour (yellow, for spatial reference).

Chapter 2

Technical Approach

2.1 Dynamical sensitivity analysis

Sensitivity analysis is a measure of the effect of *a priori* changes to the inputs on a chosen function of the outputs. Sensitivity analysis can be derived from changes in model parameterization (Ratnam and Kumar, 2005), or assumed importance of a forecast feature (e.g., synoptic reasoning; Aberson 2003) that is altered *a priori* to observe the impact on a forecast. These approaches to sensitivity analysis involve potential changes to a wide range of potential parameters and/or variables in the forecast. Each change has an associated computational cost to investigate and, to determine significance, must be implemented one at a time. Dynamical sensitivity analysis differs from other sensitivity analysis techniques as the sensitivities elucidate dynamical features important for changing an aspect of the forecasted atmosphere. Particularly, adjoint-based dynamical

sensitivity analysis is capable of generating an estimate of the impact of any perturbation to the initial state on a chosen aspect of the forecast state, within the constraining assumptions (see section 2.1.1).

2.1.1 Nonlinear model, tangent linear model and adjoint model

Given a set of initial and boundary conditions, a numerical weather prediction (NWP) model is a numerical solver of a system of nonlinear partial differential equations that evolve the atmospheric state forward in time to produce a future forecast state. The nonlinear model (NLM), represented as M, propagates an initial model state x, forward in time. ($\mathbf{x}_{\text{in}}$). The initial state represents initial conditions and contains necessary boundary conditions. The model propagates the initial state to a future model state $\mathbf{x}_{\text{out}}$, where

$$\mathbf{x}_{\text{out}} \;=\; M(\mathbf{x}_{\text{in}}) \tag{2.1}$$

The NWP model is typically nonlinear and includes explicit and parameterized physics and moisture schemes that can be turned on and off by, given the spatial and temporal evolution of the forecast state. These parameterization schemes serve to approximate atmospheric processes on scales not resolved by the chosen model discretization.

The tangent linear model (TLM) is derived from the nonlinear model by linearizing the time-tendency equations about a nonlinear NWP model trajectory, called the basic state or control trajectory. Given perturbations to the initial conditions of the basic state trajectory, the TLM calculates future perturbations evolved along the *full physics*

trajectory of the NWP model defined by the basic state:

$$\mathbf{x}'_{\mathrm{f}} = \mathbf{L}\mathbf{x}'_0 \tag{2.2}$$

where $\mathbf{x}'$ is the perturbed state vector, f is the final model state, 0 is the initial model state, $\mathbf{x}$ and $\mathbf{L}$ is the TLM linear operator, called the "tangent linear propagator" (e.g., Hoover and Morgan 2010). The adjoint model is defined as the transpose of the TLM approximation to the nonlinear NWP model, linearized about the forecast trajectory of the NLM. Adjoint models evaluate the gradient of a specific forecast aspect (known as a *response function*, R) with respect to changes in the model state ($\mathbf{x}$) at earlier times by evolving the gradient $\partial R/\partial \mathbf{x}$ (or $\widehat{\mathbf{x}}$) "backward" in time along the NLM trajectory:

$$\frac{\partial R}{\partial \mathbf{x}_0} = \mathbf{L}^{\mathrm{T}} \frac{\partial R}{\partial \mathbf{x}_f} \tag{2.3}$$

The response function is a measurable characteristic of the forecast that must be differentiable with respect to the model state (Errico, 1997) but is otherwise at the discretion of the user. The adjoint model is initialized using the gradient of the response function with respect to the model final-time forecast state. For this study, response functions measuring TC intensity are considered. The adjoint evolves the sensitivity gradient "backward" along the trajectory of the NLM to compute the sensitivity of R to prior times in the model forecast. Specific examples of response functions used are in Section 2.1.2.

From a single adjoint integration, the adjoint model evaluates most efficiently the sensitivity of a chosen response function to all input parameters (Errico, 1997). The impact of any arbitrary perturbation ($\mathbf{x_0'}$) initial condition on the response function can be evaluated by taking the inner product of the sensitivity gradient with the perturbation:

$$\delta R = \left\langle \frac{\partial R}{\partial \mathbf{x_0}},\ \mathbf{x'_0} \right\rangle \tag{2.4}$$

where δR is considered the prescribed change. The prescribed change is evaluated against an estimate from the evolved nonlinear difference in the forecast ($\Delta R = R_p - R_c$). Linearity is perfectly held when $\Delta R = \delta R$, meaning the perturbations to the initial state ($\mathbf{x'_0}$) evolved exactly as prescribed (δR). This deviations from perfect linearity can represented as the linearity ratio (LR) to quantify the relationship between the evolved change (ΔR) and the prescribed change (δR):

$$\mathrm{LR} = \frac{\Delta R}{\delta R} \tag{2.5}$$

The accuracy and utility of adjoint models for dynamical case studies are constrained by the assumption of the tangent linear evolution of perturbations and the use (or absence) of simplified physics for nonlinear processes, such as moist convection. These assumptions restrict the quantitative accuracy of the adjoint-derived sensitivity gradients for highly nonlinear phenomena, like TCs, to around 48 hours (Hoover and Velden, 2020). Using a sophisticated adjoint model is beneficial for extending the utility over which sensitivities are quantitatively useful in TCs (e.g., Doyle et al. 2011, Doyle et al. 2014). The

approximation $\Delta R \cong \delta R$ is due to non-linearities that evolve in the NLM (e.g., convection, shifting track of the storm). If the difference in this approximation is small, the underlying assumptions of the adjoint are held.

The behavior of perturbation evolution can also be computed using the TLM, by comparing how the perturbation in the TLM and the perturbation defined by the difference between the perturbed and unperturbed nonlinear model trajectory simulations evolve. Qualitative and quantitative comparisons of the perturbations from the TLM and NLM can give insights into what is causing linearity to be lost. This can done be quantitatively by comparing the expected change (δR) from the TLM with the actual change (ΔR) in the nonlinear model, where the resulting comparison is an approximation for the correlation between the TLM and NLM perturbations. Further qualitative analysis can be performed by comparing changes in the model state to investigate reasons for differences between the TLM and NLM perturbations; for example, if the speed of propagation is faster in the TLM than the NLM, the linearity would be low even if the magnitude and distribution of the perturbed states are consistent.

2.1.2 Response functions

The response function is a measurable characteristic of the forecast that must be differentiable with respect to the model state (Errico, 1997) but is otherwise at the discretion of the user. An adjoint sensitivity study can provide useful information about the final time forecast characteristic at earlier times, but only if the selected response function

accurately represents the physical property the user is interested in investigating. Improper attribution of sensitivities is also possible, if the user makes assumptions about the relationship of the sensitivities and their co-location with the forecast trajectory. This concern is outlined by Hoover and Morgan (2011) for tropical cyclone steering. Previous adjoint sensitivity studies for tropical cyclone intensity change predominantly define intensity in terms of the (1) sea level pressure (Langland et al. 1995; Chu et al. 2011) or (2) the low-level wind fields (e.g., Doyle et al. 2011; Ito et al. 2011), either from the vorticity (Vukicevic and Raeder, 1995) or kinetic energy (Doyle et al. 2011; Doyle et al. 2012) within a lower-tropospheric volume region surrounding the storm center.

In the presented work, three response functions are used:

1. (Minus) the average *surface pressure* of dry air: the response function (R_1) is a model state variable that is a proxy for sea level pressure:

$$R_1 = \frac{1}{N} \sum_{i,j \in D} -\mu_{ij} \tag{2.6}$$

where μ is the dry air in a model column extending from the surface to the top of the model. These values are summed over N grid points in a horizontal domain D indexed zonally by i, and meridionally by j over a defined region centered on the maximum vorticity at 850 hPa. The negative sign is included to such that the sign sensitivities is consistent with other response functions, such that a positive perturbation to a positive sensitivity would result in increasing R_1. An increase in R_1 through perturbing the initial

conditions would correspond to lower pressure on average in that domain.

2. The average kinetic energy: the response function (R_2) is defined as:

$$R_2 = \frac{1}{N} \sum_{i,j,k \in D} \frac{1}{2}(u_{ijk}^2 + v_{ijk}^2) \tag{2.7}$$

where u and v are the zonal and meridional components of the horizontal wind with the same horizontal domain D as described for R_1 and indexed vertically by levels k. The KE response function is similar to the response function used in previous studies (Doyle et al., 2012), which measures the kinetic energy of the winds in the domain centered on the storm. An increase in R_2 results in stronger winds when the response function is defined.

3. The *vortex-associated kinetic energy* (VAKE) response function (R_3) measures the kinetic energy associated with the vorticity of the cyclone defined as:

$$R_3 = \frac{1}{N} \sum_{i,j,k \in D} \frac{1}{2}(u_{\zeta_{TC}ijk}^2 + v_{\zeta_{TC}ijk}^2) \tag{2.8}$$

where ζ_{TC} is the vertical component of vorticity associated with the TC with the same domain D as described for R_2. The response function VAKE (R_3) was developed to address a potential issue with R_2 and is discussed in detail in Chapter 4.

By defining and averaging the response functions over a domain centered around the TC, changes in the response functions are less sensitive to small displacements in the storm

track and small, local extrema from evolved perturbations. While not an exhaustive list of potential response functions for tropical cyclone intensity, these capture a range of metrics all with their own benefits and drawbacks.

2.1.3 Derived Sensitivities from State Variables

An adjoint model produces the sensitivity of a response function to the model state variables (i.e., temperature, pressure, winds, moisture). In addition to sensitivity to model state variables, derived sensitivities to vorticity and divergence ($\widehat{\zeta}$ and $\widehat{\delta}$ respectively; Kleist and Morgan 2005) can also be computed, as they are potentially more insightful to consider since they can be directly related to synoptic features (e.g., vorticity and divergence extrema associated with mid-latitude upper-tropospheric weather systems, tropical Kelvin waves, or changes in the outflow layer inertial stability - where vorticity in the outflow layer is a surrogate for inertial stability). These sensitivities are directly calculable from the sensitivities to the horizontal wind components ($\widehat{u}$ and $\widehat{v}$) as in Kleist and Morgan (2005):

$$\nabla^2\widehat{\zeta} \;=\; -\left(\frac{\partial\widehat{v}}{\partial x} \;-\; \frac{\partial\widehat{u}}{\partial y}\right) \text{ and } \nabla^2\widehat{\delta} \;=\; -\left(\frac{\partial\widehat{u}}{\partial x} \;+\; \frac{\partial\widehat{v}}{\partial y}\right)$$

Additionally, perturbations can be constructed from adjoint sensitivities to elucidate the physical significance of these sensitivities.

2.1.4 Optimal perturbations

The coincidence of synoptic scale features with sensitivities alone is insufficient to ascribe dynamical significance to that feature (Langland et al., 1995). The coincidence of sensitivities to a state variable with Eulerian tendencies in that variable implies dynamical significance. Numerical simulations can be perturbed using adjoint-informed optimal perturbations (e.g., Doyle et al. 2012; Hoover 2015). Adjoint-derived sensitivity gradients, $\partial R/\partial \mathbf{x}$, can be used to objectively calculate the optimal perturbations to the initial conditions of the model to produce a prescribed change in the response function at the final time. These perturbations are considered optimal as they require the minimum amplitude change in energy, as defined by a moist static energy norm (Ehrendorfer et al., 1999):

$$e \;=\; \tfrac{1}{2}\left\langle \mathbf{x'_0},\, \mathbf{W}\mathbf{x'_0} \right\rangle \;=\; \tfrac{1}{2}\left[u'^2_{ijk} \;+\; v'^2_{ijk} \;+\; \frac{c_p}{T_0} T'^2_{ijk} \;+ RT_0 \left(\frac{p'_{ij}}{p_0}\right)^2 \;+\; \varepsilon \frac{L_v^2}{c_p T_0} q'^2_{ijk} \right] \tag{2.9}$$

where the weighting matrix, $\mathbf{W}$, determines the initial time amplitude or norm, u', v', T', p', and q' are the perturbed zonal flow, meridional flow, potential temperature, perturbation (i.e., non-static) pressure at the surface, and specific humidity, respectively. The reference state for potential temperature is (T_0; 300.00 K) and for pressure (p_0; 1000.00 hPa), c_p is the specific heat at constant pressure, R is the dry air constant, and L_v is the latent heat of condensation per unit mass. The scalar coefficient ε controls the relative weighting of the moist static energy term, $\varepsilon \frac{L_v^2}{c_p T_0} q'$, within the norm. The above energy-based norm equation represents the combined perturbation kinetic energy, perturbation

available potential energy, perturbation elastic energy, and perturbation latent (heat). Constraining equation 2.9 by the prescribed change (equation 2.4) results in the optimal change in the initial state wind, temperature, pressure, and/or moisture, based on your choice of response function R and by the ΔR desired using a Lagrange multipliers technique. This technique investigates the sensitivity of R to initial perturbations since the perturbations are defined *a priori* to change the response function. The Lagrange multiplier used to constrain the problem is defined as derived in Errico (1997):

$$L = e - \lambda \left(\delta R - \langle \frac{\partial R}{\partial \mathbf{x}_0}, \mathbf{x}_0^{'} \rangle \right) \tag{2.10}$$

Where the perturbation initial state ($\mathbf{x_0^{'}}$) is unknown. Through differentiation of L with respect to λ yields:

$$\triangle R = \lambda \frac{\partial R}{\partial \mathbf{x}_0} \mathbf{W}^{-1} \frac{\partial R}{\partial \mathbf{x}_0} \tag{2.11}$$

which can be written as, with respect to λ:

$$\lambda = \frac{\frac{\partial R}{\partial \mathbf{x}_0}}{\langle \frac{\partial R}{\partial \mathbf{x}_0}, \mathbf{W}^{-1} \frac{\partial R}{\partial \mathbf{x}_0} \rangle} \tag{2.12}$$

Optimal perturbations are obtained by differentiation of L with respect to $\mathbf{x_0^{'}}$ and with the solution $\partial L / \partial \mathbf{x_0} = 0$:

$$\frac{\partial L}{\partial \mathbf{x}_0} = 0 = \mathbf{W^{-1}} \mathbf{x}_0 - \lambda \frac{\boldsymbol{\partial} R}{\boldsymbol{\partial} \mathbf{x}_0} \tag{2.13}$$

Solving for the initial condition perturbations yields:

$$\mathbf{x}_0^{'opt} = \lambda \mathbf{W}^{-1} \frac{\partial R}{\partial \mathbf{x}_0} = \delta R \frac{\mathbf{W}^{-1} \frac{\partial R}{\partial \mathbf{x}_0}}{\langle \frac{\partial R}{\partial \mathbf{x}_0}, \mathbf{W}^{-1} \frac{\partial R}{\partial \mathbf{x}_0} \rangle} \tag{2.14}$$

From this expression, it is evident that the initial perturbations ($\mathbf{x}_0' = \{u',\ v',\ T',\ p',\ q'\}$) are directly proportional to the initial time adjoint-derived sensitivity gradient in the limiting case, where the terms in $\mathbf{W}$ are constants.

The validity of a adjoint model's estimate of the sensitivity is measured by comparing the evolved nonlinear perturbation to the initial state by taking the dot product of the sensitivity gradient at time τ with the perturbed model state at the same forecast time τ:

$$\delta R = \langle \frac{\partial R}{\partial \mathbf{x}_\tau}, \mathbf{x}_\tau^{'} \rangle \tag{2.15}$$

If linearity is held, this dot product should equal the prescribed change in response function used to initialize the adjoint model, ΔR. Any deviations are due to the limitations discussed previously. Linearity can also be calculated through the correlation of the NLM simulation difference and the TLM perturbations, where a high correlation indicates that the linear assumptions used to define the adjoint model are upheld.

2.2 WRF-ARW and WRFPLUS configurations

The Weather Research and Forecasting (WRF) — Advanced Research WRF (ARW) forward model (Skamarock and Coauthors, 2008) and its adjoint (Zhang et al., 2013),

available through WRFPLUS (version 3.8.1) are used to simulate TCs and their environment, compute sensitivity gradients based on prescribed response functions for the TC intensity, and to perturb the initial state, based on those sensitivity gradients, to diagnose key processes that influence the intensification of a TC.

The WRF-ARW is a nonlinear, fully compressible, non-hydrostatic with a terrain-following hydrostatic pressure coordinate, full physics NWP model with Arakawa C-grid grid staggering. The model uses 2nd and 3rd order time integration and 2nd to 6th order advection schemes in both the horizontal and vertical. The WRF-ARW can be run in a variety of configurations using both idealized and real data simulations for case studies or near real-time forecasts. The simulations are run on a Lambert Conformal map projection. The WRFPLUS contains both the forward, nonlinear model and its adjoint of the WRF-ARW. The adjoint is capable to run in a stand-alone mode to calculate sensitivity gradients, or to accompany WRF 4D-variational data assimilation (through WRFDA) to minimize the distance between the model state and observations at the time in which the observations appear in the assimilation time window. The physical parameterizations available for the WRF and its adjoint are in Table 2.1.

The WRF adjoint, available through WRFPLUS, contains the adjoint of most moist physical processes for large-scale condensation and the adjoint of a simplified cumulus scheme (Xiao et al. 2008; Chu et al. 2011). The advantage of using the WRF and its adjoint is it's highly adaptable and is generally a standard NWP model for higher resolution, limited domain modeling. Furthermore, its adjoint can easily be initiated

with a variety of response functions. Disadvantages can be the canned nature of the model, finding the ideal configurations for model physics settings, and grid spacing to both ensure the development of the TC while meeting the constraints of linearity.

Physics Option	WRF scheme name	WRFPLUS scheme name
Cloud microphysics	Goddard microphysics	Large-scale condensation
Longwave Radiation	RRTM (Rapid Radiative Transfer Model)	None
Shortwave Radiation	Goddard shortwave	None
Surface Layer	MM5 similarity	None
Land Surface	Noah land surface model	Noah land surface model
Planetary Boundary Layer	Yonsei University	Yonsei University
Subgrid cumulus parameterization	Kain-Fritsch	Simplified scheme

TABLE 2.1: WRF and WRFPLUS Physics Scheme options used in the nonlinear model and adjoint model simulation within this work.

Tests were conducted with the outlined model set up to investigate the role of horizontal and vertical resolution on the simulation's forward trajectory and adjoint sensitivities. The vertical model spacing in all cases is evenly spaced, with simulations using either 41 or 64 terrain-following vertical levels from the surface to 50 hPa. The horizontal resolution was tested at both 18 and 30 km. Additionally, the model time step was varied from 30 to 90 seconds. Output of the model trajectory from simulations, which is necessary to initialize the adjoint, is saved every 30 seconds to 3 minutes, depending on model timestep and resolutions. Specific cases are discussed in Chapters 3, 4, and 5.

Previous adjoint studies (e.g., Doyle et al. 2011; Doyle et al. 2012; Hoover 2015; Reynolds

et al. 2016) have demonstrated the effectiveness and appropriateness of adjoint applications for TC dynamics at resolutions comparable or coarser resolutions to simulations outlined here.

2.3 Initial Condition Data

Model initial and boundary conditions are configured using the WRF Preprocessing System (WPS). The WRF-ARW simulations are initialized using the National Center for Environmental Predictions (NCEP) FNL (Final) operational global analysis on 0.25° x 0.25° latitude-longitude grid available from the National Center for Atmospheric Research (NCAR) Research Data Archive (RDA) as dataset ds083.3. The data used from this archive include NCEP's Global Forecast System (GFS) every 6 hours (0000, 0600, 1200, 1800 UTC daily) and short-term (3 hour) forecasts of the GFS from those 6 hourly analyses. Through this configuration, boundary conditions are updated every 3 hours. Additional analysis is completed using the isobaric and surface ERA5 reanalysis on 0.25°x 0.25° latitude-longitude grid available from NCAR's RDA as ds633.0.

When using GFS data in WPS, the user has an option to represent sea level pressure: PRMSL is *pressure reduced to mean sea level* and MSLET is *mean sea level pressure using eta reduction.* The first, MSLET, uses unsmoothed atmospheric fields and computes below ground extrapolated temperature by relaxing Laplace's equation. The second, PRMSL, for legacy reasons spectrally truncates fields to T80 (approximately 150km effective resolution) everywhere (Hart and Cowan, 2018). This results in a much smoother

sea level pressure field than obtained by MSLET. Additional tests were completed to determine whether the initial sea level pressure structure, particularly important for the TC vortex, influences the simulated forecast trajectory and/or the adjoint sensitivities.

Chapter 3

Identifying sources of tropical cyclone intensity change

3.1 Overview

Adjoint sensitivity studies provide information about how a forecast metric (i.e., response function) changes with changes to the initial state. From this relationship, perturbations to the initial conditions can be constructed to evaluate the impact of small changes to the initial state. The perturbation evolution can additionally be evaluated to identify physical processes changing in the basic state trajectory at times prior to the response function being defined. Adjoint sensitivity analysis has few previous applications with tropical cyclones using a case study approach, particularly when evaluating intensity metrics. The following case study evaluates an established surface pressure intensity metric to

investigate how small changes to the initial state grow and change physical processes, ultimately changing the TC intensity forecast. Additionally, in this chapter the role of perturbing only the upper troposphere or lower troposphere based on adjoint sensitivities is evaluated. These experiments seek to evaluate if perturbing only the upper troposphere or lower troposphere alone can result in the prescribed intensification.

An established framework to evaluate expected TC intensity change is the Statistical Hurricane Intensity Prediction Scheme (SHIPS) and the SHIPS Rapid Intensity Index (SHIPS-RII). As discussed in section 1.3, SHIPS and SHIPS-RII evaluate a combination of current conditions, including satellite data, persistence metrics, and model forecast data. Through historical data sets, an established statistical relationship between these metrics and expected intensity change has been established to relate each variable to TC intensity through a weighted coefficient. Aspects of this framework are used in the present study, particularly, evaluating the change of synoptic scale variables in the horizontal and vertical range used in SHIPS(RII). The metrics evaluated are the average 200 hPa temperature and divergence within a 1000 km radius, the 850 hPa relative vorticity within a 1000 km radius, the 700-850 hPa average relative humidity within a 200 - 800 km radius, the 200-850 hPa vertical shear of the horizontal winds within a 200 - 1000 km radius, and the precipitable water within a 100 - 200 km radius. These variable definitions can also be found in Appendix A. While the regression coefficients established within SHIPS and SHIPS-RII literature cannot be used, the general relationship (e.g., sign of change) and magnitude of change can provide insights into changes of physical processes. Additionally,

the distribution of change and the physical implications are evaluated within the context of this case study.

3.2 Case Study: Florence (2018)

Hurricane Florence (2018) originated as a convectively active tropical wave, which moved off the west African coast on 30 August and became a hurricane in the Lesser Antilles (Stewart and Berg, 2019). Undergoing two distinct rapid intensification (RI) periods, the first on 4 September in less than favorable large-scale conditions (15–20 kt of southwesterly vertical wind shear, mid-level relative humidity $< 50\%$, sea surface temperature $< 27°C$), which was not well forecasted by operational models. Subsequently, Florence underwent a period of rapid weakening due to shear associated with a mid-to-upper level shortwave trough passing just north of Florence. A second period of RI, beginning 9 September, occurred in more favorable conditions (vertical shear 5-10 kt) and consequently was better predicted. During the second period of RI, outflow jets formed in the northwestern and southeastern quadrants of the hurricane that allowed for the further intensification of the hurricane. Florence subsequently weakened again, due in large part to traversing a shallow layer of warm water. Florence eventually made landfall in the coastal Carolinas as a Category 1 hurricane, however, the slow translation speed and orographic barriers near the coast resulted severe flooding (Stewart and Berg, 2019).

3.2.1 Synoptic Overview

This study focuses on a 36-hour period associated with the second RI period, initialized at 0000 UTC 9 September, using the Weather Research and Forecasting (WRF; Skamarock and Coauthors 2008). The WRF adjoint, available through WRFPLUS (Zhang et al., 2013), contains the adjoint of physical processes for large-scale condensation scheme and the adjoint of a simplified cumulus scheme (Xiao et al. 2008; Chu et al. 2011). The WRF was initialized using the National Center for Environmental Predictions (NCEP) FNL (Final) operational global analysis on 0.25° x 0.25° latitude longitude grid available from the National Center for Atmospheric Research (NCAR) Research Data Archive (RDA) as dataset ds083.3. Further details about model configuration can be found in Section 2.2. The numerical simulation was run at 18 km horizontal grid spacing. This grid spacing is consistent with the few other adjoint-based tropical cyclone studies (e.g., Doyle et al. 2011; Doyle et al. 2012; Reynolds et al. 2016). The model was configured with 40 layers of evenly spaced vertical levels, from the surface to 50 hPa.

The storm does not reach the same intensity or intensification rate as observed, however, it is consistent with the experimental the Navy Research Laboratory COAMPS-TC model (CTCX), the Global Forecast System (GFS) Model Forecast (AVNO), and the Finite-Volume Cubed-Sphere Dynamical Core model (FV3G). These model forecasts are run at finer grid spacing, nested 45-15-5 km, 13 km, and 13 km, respectively. Tracing the track and intensity, the track forecast is consistent with the best track. After 36 hours, the simulation has developed a hurricane with a central pressure of 968.1 hPa and maximum

surface wind of 78 kt. While the WRF simulation does not capture the correct intensity or intensification rate, the synoptic environment is consistent with analysis. Furthermore, the simulation is not expected to replicate the Hurricane Florence (2018) rather simulate an environment capable of supporting a TC, which the simulation successfully does.

At the initial model time, to the southwest of Florence there the average relative humidity is low (40-60%). The advection of low water vapor content air into the near storm environment limits the potential for storm development (Fig 3.1). Tied to the remnants of a passing short-wave trough, the asymmetric vertical shear surrounding Florence is higher in the simulation than in observations and to the north of the storm (10-30 ms^{-1}) (Fig 3.1). This shear is also associated with a developing outflow jet of the storm (Fig 3.1). The outflow in this case study is identified by the equivalent potential temperature (θ_e) that enters at the base of the eyewall. In the control simulation this value is 354 K, which in the upper troposphere is situated between 150 - 200 hPa. An anticyclone is located to the east of Florence, additionally to the southeast is a developing tropical storm which becomes Hurricane Isaac (2018).

As the simulation advances, the 200 hPa potential vorticity (PV) in the proximity of the TC is predominantly negative, with winds showing an asymmetric, anticyclonic circulation indicating the developing outflow (Fig 3.2). The near proximity of the TC with a passing extratropical trough indicates a possible interaction and aid in developing an outflow jet to evacuate mass from the TC. The 850 hPa equivalent potential temperature in the TC core shows a expanding pool of high θ_e air. To the northeast of the TC there is

relatively low θ_e air that persists throughout the simulation. Additionally, to the west of the TC there is band of minimum θ_e that is being advected about the TC. Notably, the sea level pressure becomes more asymmetric at forecast hour 36, as it borders the ridge to the east. The red box shown in the figure denotes the response function domain at the final time.

The adjoint model was initiated with the gradient of the response function (minus) the dry air surface pressure, $R = -\mu$, defined in eqn. 2.6. The response function domain is defined within a horizontal 20 by 20 grid box ($\sim$ 360 by $\sim$ 360 km) centered on the minimum μ at forecast hour 36.

3.2.2 Sensitivities

The 850 hPa sensitivity to water vapor is maximized near the TC (Fig 3.3). The strong positive sensitivity, as indicated in teal, suggests if a positive water vapor perturbation (i.e., increase the water vapor) in an annulus around the core and to the west of the TC, 36 hours later the perturbation dry air mass in a column (μ), a proxy for sea level pressure (SLP) would be lower. Additionally, the sensitivity to wind (vectors) indicate making the 850 hPa generally more cyclonic at this time would deepen the surface pressure 36 hours later. The strong positive sensitivity to water vapor is coincident with a minimum in the average relative humidity (Fig 3.3), suggesting the drier lower tropospheric air is impacting the surface pressure 36 hours into the forecast. Adjoint sensitivities can be used to make an optimal initial condition perturbation projecting onto this sensitivity feature to verify this suggestion.

The 200 hPa sensitivity to potential temperature similarly is maximized near the TC (Fig 3.4). The negative sensitivity to the north of the TC indicates cooling the 200 hPa air in the proximity of the passing trough to its west and south. This would extend the trough closer to the TC, allowing for the TC outflow to favorably interact with of the jet streak on the downstream side of the trough. Analyzing a cross section through the TC (Fig 3.5), the sensitivity to potential temperature and water vapor are highly coincident and the largest values are in the low to middle troposphere. To the west of the TC, large banded positive and negative sensitivities to potential temperature and water vapor are tilted towards the TC center. The low-level sensitivities to potential temperature and water vapor are broadly positive, which is physically consistent with a warmer, moister boundary layer leading to a more intense TC.

Figure 3.6 shows the derived sensitivity to 850 hPa vorticity, which broadly indicates increasing the cyclonic vorticity in the center and to the north and east of the TC while increasing the anticyclonic vorticity to the south and west. The vertical cross section of sensitivity to vorticity (Fig 3.7), taken over the same section as in (Fig 3.5), shows a largely positive sensitivity to vorticity at all levels with the exception of the strong negative sensitivity to the west, with a banded structure consistent with the distribution of sensitivities to potential temperature and water vapor (Fig 3.5). It is also evident in the sensitivity to meridional wind (Fig 3.8). The coincidence and orientation of sensitivity structures indicate a barotropic growth tilted upshear, which takes energy from the existing shear to grow both positive and negative vorticity (Nolan and Farrell, 1999). The tilted bands of positive and negative sensitivity structure seen in both dynamic and

thermodynamic variables are distributed in a helical pattern. Such a sensitivity structure has not been identified previously (to the author's knowledge).

3.2.3 Optimal Perturbations

Optimal perturbations u', v', t', and q' were constructed using the energy norm (eqn. 2.9) discussed in Chapter 2. The prescribed change (δR) to constrain the norm was a 1 hPa average change over the response function domain. The response function domain is a 20 by 20 grid box centered about the minimum perturbation dry air pressure (μ'). The value constraining value, δR, can be evaluated from the equation:

$$\delta R = \langle \frac{\partial R}{\partial \mathbf{x}_0}, \mathbf{x}_0^{'} \rangle \tag{3.1}$$

For each perturbed variable, the sum of the dot product between the variable adjoint sensitivity ($\partial R/\partial \mathbf{x}_0$) and the perturbed initial state ($\mathbf{x}_0^{'}$) result in the change of the total response function attributed to that variable. In the derived optimal perturbations, the prescribed change to the response function is predominantly attributed to a change in potential temperature ($\delta R = 0.66hPa$), zonal wind ($\delta R = 0.18hPa$), meridional wind ($\delta R = 0.15hPa$), and water vapor ($\delta R = 0.013hPa$), in descending order. All optimal perturbations are initially concentrated in the lower troposphere, with temperature and moisture perturbations maximized in the boundary layer. The initial changes in perturbed energy are concentrated in the lower troposphere (Fig 3.9). As time evolves, the change in perturbation KE shifts upward such that at the final time the largest change is around

200 hPa and associated with changes in the outflow layer of the TC Fig 3.9. Additionally, there is an increase in the low-level KE concentrated around 900 hPa, associated with an increase low-level wind speeds in the TC's circulation. The maximum in perturbation latent heat energy is at 900 hPa at the final time. The perturbation available potential energy has a local maximum at 900 hPa as well as a global maximum in the upper troposphere and lower stratosphere (extending from 300 hPa to the top of the model domain). At the final time, the minimum central pressure has decreased from 968.1 hPa to 966.7 hPa, a 1.4 hPa change. Additionally, on average within the response function domain, the average SLP has decreased 0.22. Through these metrics, the perturbed simulation has intensified the TC.

The normalized storm (difference divided by control value) relative averaged difference of SHIPS-related variables are shown in Fig 3.10. The variables are scaled, as described in the figure, to account for the relative change. The change in 850 hPa vorticity oscillates around zero throughout the simulation, increasing at the final time. Similarly, the 200 hPa divergence oscillates about zero with a large decrease at forecast hour 33, indicating convergence within the outflow layer. Similarly, the vertical shear increases throughout the simulation with a peak at forecast hour 33, consistent with the large change in 200 hPa divergence. The initial perturbed RH has decreased, as the low-level potential temperature has increased more than the water vapor, and increases relative to the control at all forecast times the RH increases. This contrasts at the final time when the precipitable water has decreased, though increased slightly at all times prior. The 200 hPa temperature increases throughout the simulation, in contrast to the Carnot heat engine

conceptual model that an intensifying TC will decrease the outflow level temperature to increase its efficiency.

Analyzing the horizontal distribution of select SHIPS-related metrics, Fig 3.11 shows the initial and evolving change in 850 hPa vorticity. The banded structure, as seen in the sensitivities, is evident around the TC. The evolved perturbations, 18 hours later, remain somewhat banded but smaller scale with a shift in the TC core to the southwest. The largest change is associated with local, elongated vorticity maxima. At forecast hour 36, the largest change is in the core, indicating a slight shift south and an increase in the vorticity (Fig 3.11). Additionally, the average perturbed 850 hPa vorticity within 1000 km of the TC increases, consistent with Fig 3.10.

At the initial forecast hour, the change in temperature is small and largely asymmetric around TC (Fig 3.12), cooling to the north and warming to the east and west. This is consistent the the sensitivity to potential temperature (Fig 3.4). As the perturbations evolve, at time forecast hour 18 the average change within 1000 km is slightly warmer particularly to the north of the TC. The dominant changes to the south are associated a shift and reorientation. At the final time, the perturbations have warmed the 200 hPa potential temperature to the north of the TC and around the core. To the south of the TC center, there is both warming and cooling. Some of this change is attributable to the change in position, as the TC center shifts southward.

3.2.4 Linearity

To test the validity of the tangent linear model (TLM) assumption for this case, the linearity ratio (LR; eqn. 2.5) of the prescribed change (δR) is evaluated against an estimate from the evolved nonlinear difference in the forecast (ΔR). The linearity ratio is 0.22, indicating that the tangent linear assumption is poorly held quantitatively. Analyzing the change in the R_μ (eqn. 2.6), the largest change is to the south indicating a deepening low pressure in addition to a southward shift (Fig 3.13). Comparing the nonlinear change in R_μ to the TLM perturbations it is evident that the loss in linearity is partially due to a smaller magnitude change in R_μ, as well as a difference in the orientation perturbations around the TC as the TLM shifts and deepens the northeast. The low linearity ratio creates questions for whether this particular case study is valid within an adjoint framework. Furthermore, it leads to questions regarding where and how the linearity is lost in the nonlinear model trajectory. It is hypothesized, that the low-level perturbations to potential temperature and water vapor will create (moisture) instabilities that will result in more convective, moist elements that are nonlinear in nature. The perturbations to the upper troposphere in contrast, are hypothesized to not be as linked to nonlinear elements and thus will retain their linearity ratio better. This is tested in in the following section.

3.3 Influence of upper and lower troposphere on intensity change

As shown in Fig 3.9, the all components of the optimal perturbations are concentrated in the lower troposphere. At the final time, the largest changes to kinetic energy (KE) and available potential energy (APE) are in the upper troposphere. The growth of perturbation energy from the lower troposphere to the upper troposphere motivates an investigation of whether the same change in the response function ($-\mu$) can be made through only perturbing either the upper or lower troposphere. If so, how do the physical processes and pathways to development change when the optimal initial perturbation is confined to either the upper or lower troposphere? Furthermore, as found in the previous section, the evolution of the perturbations was not sufficiently linear, based on the LR. Through partitioning the atmosphere we can test if the upper or lower optimal initial perturbation can better satisfy the tangent linear assumption.

3.3.1 Vertical Partition Optimal Perturbations

To investigate these questions, optimal perturbations based on the adjoint sensitivities described in section 3.2.2 are calculated. As in the full domain perturbed simulation, optimal perturbations u', v', t', and q' were constructed using the energy norm (eqn. 2.9) discussed in Chapter 2. For the following experiments, a local projection operator (LPO) is used to vertically partition the model atmosphere. Sensitivities outside of the specified model levels are set to zero using the LPO. The prescribed change (δR) to constrain the

norm was a 1 hPa average change over the response function domain. As the sensitivities in the upper troposphere are smaller in magnitude, perturbations were scaled to obtain the same prescribed change (δR). The three perturbed simulations will be referred to as 1) full perturbation experiment (FPE; LPO model levels 0 to 41), 2) lower perturbation experiment (LPE; LPO model levels 0 to 20), and 3) upper perturbation experiment (UPE; LPO model levels 21 to 41).

For the UPE, the upper troposphere perturbations are approximately 13 times larger than the full domain perturbations. For the LPE, the lower perturbations are 1.1 times larger than the full domain. This scale can be calculated as optimal perturbations at initialization are linearly related to the adjoint sensitivities. From the perturbation vertical energy structure, this change at initialization is shown in Fig 3.14, where the UPE has a notably larger fraction in the top half of the model atmosphere. After 12 hours, the full and lower perturbation energy structure are nearly identical, with the UPE perturbations still retaining a larger change in the upper troposphere. Another 12 hours later (forecast hour 24), the difference in the relative magnitude between simulations continues to narrow, with the upper perturbation experiment retaining a larger fraction of perturbation energy in the upper troposphere compared to the lower and full troposphere. At the final time (forecast hour 36), the the levels of maximum perturbation energies are similar across experiments, with the UPE (LPE) resulting in a larger fraction in the upper (lower) troposphere (Fig 3.14).

In the response function domain, the evolved average changes in the sea level pressure

(the differences in sea level pressure between perturbed and control non-linearly evolved initial conditions) for the UPE, LPE, and FPE are -0.85 hPa, -0.11 hPa, and -0.22 hPa, respectively. The lowest SLP however corresponds to the FPE (966.7 hPa) followed by the LPE (967.0 hPa), and UPE (967.6 hPa), recalling the minimum SLP in the control simulation is 968.1 hPa. This is due to a broadening UPE TC vortex and a westward shift (Fig 3.15a). The total change in the LPE and FPE are nearly identical, with a slight southward shift and deepening of vortex center (Fig 3.15b and (Fig 3.15c).

Analyzing the evolution of SHIPS-related variables for the LPE, the sign and distribution are nearly identical for the first 9 hours of the integration (Fig 3.16 and Fig 3.10). After 9 hours into the forecast, the LPE has higher 850 hPa vorticity, with larger amplitude oscillations about zero, with a large shift from positive to negative change 24 to 27 hours into the forecast, respectively. After 9 hours into the forecast, the 200 hPa divergence in the LPE oscillates about zero at a smaller amplitude than the FPE. The cause of this distribution likely is associated with the LPE perturbations not growing and extending as much into the upper troposphere compared to the FPE. The relative change 36 hours into the forecast for all variables shown in Fig 3.16 are a smaller relative change, smaller than in Fig 3.10.

The average change in the UPE (Fig 3.17) shows larger average changes for nearly all time steps compared to both the FPE and LPE. After the first time step, the 850 hPa vorticity is on average larger for the UPE than either the LPE and FPE indicating the perturbations in the outflow have extended downward rapidly to change the low-level

vorticity. The 850 hPa vorticity from 3 hours through 30 hours into the forecast is negative, becoming and remaining positive after 33 into the forecast. Consistent with the FPE, at forecast hour 33 the 200 hPa divergence change is negative and large. The RH has little change throughout the simulation, while the PW increases throughout the simulation. From the evolution of perturbed SHIPS-related variables, it is evident that the largest changes relative to the control simulation are from the UPE. While the UPE perturbation magnitude is larger, the prescribed change ($\delta R = 1hPa$) is constant for all three experiments suggesting that perturbations to the upper troposphere alone have a substantial impact on TC intensity change for this case.

Figure 3.18 shows the evolution of 850 hPa relative vorticity for UPE. After 3 hours into the forecast, small vorticity perturbations are already evident within the TC core (Fig 3.18b). As the simulation progresses, the perturbations increase and indicate a shift in position (relative to the control) of vorticity at the TC core and in outer bands. The upper perturbations used to initialize this simulation grow downwards to create change in the lower troposphere. At forecast hour 36, the largest change is a shift and increase to the west (Fig 3.18h). Comparing the UPE (Fig 3.18b)to the LPE (Fig 3.19b), the initial change in 850 hPa is larger but by 3 hours into the forecast, the largest magnitude changes are comparable (Fig 3.19b). The LPE vorticity evolution remains smaller on average throughout the remainder of the simulation, with a shift and increase in vorticity to the south 36 hours into the forecast (Fig 3.19h). The evolution of the FPE is nearly identical to the LPE.

The evolution of the average change the of SHIPS-related variables, including the increase in 200 hPa temperature and 200 hPa convergence, suggests changes to the outflow level. To investigate this, the 200 hPa change in PV across simulations is analyzed. In the UPE, except at forecast hour 3, the average change in the evolution of the 200 hPa PV is lower than the control simulation within approximately 1000 km of the TC center (Fig 3.21). Furthermore, the extent of the near zero and negative PV is broader, most notably from 12 hours into the forecast (Fig 3.21d) through 30 hours into the forecast (Fig 3.21g). This indicates an enhanced outflow, consistent with more mass evacuation above the surface low - a situation that supports intensification. The outflow remains asymmetric, elongated longitudinally particularly to the east. The change in the LPE 200 hPa PV is small at all times, as indicated in both in magnitude and distribution (Fig 3.22). The change in the FPE 200 hPa PV shows less change than the UPE, however, after 18 hours into the forecast the change in PV becomes negative and slightly broader than the control simulation (Fig 3.23). The difference in the 200 hPa PV across experiments are consistent with the change in average SLP shown in Fig 3.15, with the largest changes in the UPE compared to the FPE and the UPE.

To further understand the changes in the outflow level, the azimuthal average of both the azimuthal wind and radial wind are calculated from the TC center to a 1000 km radius. While not perfectly axisymmetric in the control simulation (shown in the contours) still shows a robust azimuthal (Fig 3.24) and radial (Fig 3.25) circulation developing from initialization through the final forecast hour. A benefit of looking at the change in the TC structure relative to the vortex center for each experiment is that positional shifts across

simulations can be accounted for, as each azimuthal averaged is calculated relative to the TC center in that simulation. The perturbation in the azimuthal wind at initialization, 3 hours into the forecast, and final forecast hour is shown in Fig 3.24 for all experiments. The change at initialization across all three experiments is small, as expected based on perturbation size and the asymmetries seen in the sensitivity patterns. At forecast hour 3, the differences become more pronounced, with the UPE indicating a decrease in the azimuthal wind in the region the outflow level anticyclone later develops in (Fig 3.24b). In both the LPE and UPE, at forecast hour 3, no substantial changes are seen in the upper troposphere. At forecast hour 36, the largest changes in the azimuthal wind are in the UPE (Fig 3.24c), indicating a more robust anticyclone has developed, slightly closer to the core of the TC than in the control simulation. Additionally, the change indicates that the depth of the cyclonic flow in the upper troposphere is weakening and broadening. A similar change is seen across all three simulations at the final time, with the LPE and FPE showing a smaller overall change. The vertical extent of the cyclonic vortex in the LPE and FPE does not show the same coherent signal of a weakening or lowering.

Similar to the perturbed azimuthal wind, the perturbed azimuthally averaged radial wind at initalization is small with no discernible organized structure (Fig 3.25) due to the cyclone's being not well organized at this time nor having an axisymmetric upper tropospheric structure. At forecast hour 3, the UPE, LPE, and FPE all show a slight decrease in the near-surface inflow near the core, though the UPE also shows a slight enhancement of the azimuthially averaged inflow in the lower troposphere (Fig 3.25b). For the UPE, in the upper troposphere, coincident with the maximum outward radial wind of

the control simulation, at this time, is a decrease in the radial wind. Below the decrease in radial wind is a maximum in perturbed outward radial flow that extends upward and outward from the TC center to 1000 km. The LPE and FPE both indicate a smaller, but still decrease in outward radial flow 3 hours into the forecast coincident with the upper troposphere radial maximum (Fig 3.25e&h). Unlike the UPE, both the LPE and FPE show a decrease in the outward radial wind in the upper troposphere. At forecast hour 36, the UPE has the largest change in the radial wind across simulations, maximizing in the outflow layer (Fig 3.25c). The change is consistent with what was seen in the change in azimuthal wind (Fig 3.24c), with a lowering of the maximum radial outflow. This is also seen in the LPE and FPE, except at a smaller magnitude. In the low-level radial wind, the inflow in the UPE has a broad increase in inward radial flow below the outflow layer. The LPE and FPE increase the inflow in a concentrated region in near the TC center.

The azimuthal average perturbations to the azimuthal and radial wind are consistent with the time evolution of the other fields analyzed within this chapter. Additionally, through the analysis of azimuthal average, it is identified that in the outflow level is lowering and broadening. This explains why the 200 hPa temperature on average is increasing in the SHIP-related time evolution. The similarities in distribution of perturbations to the azimuthal and radial wind in all three simulations at 36 hours into the forecast indicate role the response function used has on how optimal perturbations evolve.

3.3.2 Vertical Partition Linearity

As discussed in section 3.2.4, linearity ratio for the FPE is 0.22, indicating that the tangent linear assumption is poorly held quantitatively. Comparing the FPE to the LPE and UPE, the horizontal distribution of the response function value ($-\mu$) is shown in Fig 3.26. As expected from the change in SLP (Fig 3.15), the largest change is in the UPE with the FPE and LPE showing similar magnitude and distribution changes. The linearity ratio in the LPE is 0.090 and the linearity ratio in the UPE is 1.03. The near zero linearity ratio for in the LPE indicates two hypotheses: first, the LPE creates low-level moisture instabilities that result in nonlinear moist convective elements, which cannot adhere to the tangent linear assumption. Second, lower troposphere perturbations alone cannot result in TC intensity change. This is due to the enhanced low-level circulation converging mass faster than the outflow can evacuate mass (as seen the outflow level PV does not change much) resulting in an imbalance that restricts intensification. The high, nearly unity, linearity ratio in the UPE experiment indicates that the upper troposphere alone can change TC intensity. Contrasting with the LPE, the upper troposphere perturbation likely result in smaller moisture instabilities allowing the tangent linear assumption to be held. Additionally, it suggests that the enhanced outflow, as indicated by lower PV and more robust azimuthal and radial wind in the outflow layer, can lead to low-level development through enhanced mass evacuation.

Analyzing the TLM distribution of $-\mu$ in the respective experiments, all show the same location of maximum and minimum change in $-\mu$ and have the same average change in the

domain shown (1 hPa). This is expected as the experiments are linearly related. However, the UPE shows substantially larger extremes. As the TLM perturbation evolution is linear, the first hypothesis that the cause of the low linearity ratio is due to instabilities can not explain the differences in the extremes. This indicates that given a more robust outflow development in the low-level vortex can happen more readily and lead to larger changes in the surface pressure. An additional feature in the TLM perturbations is the shift in location as indicated by the dipole of maximum and minimum values. This shift is unanticipated, though understandable as the response function does not include information on how to structure the change in $-\mu$, only to increase $-\mu$ on average 1 hPa. The ability for the TLM track to shift add further considerations for evaluating the change in nonlinear perturbations. Additional consideration should be made on how the response function is defined to mitigate a shift in the TLM. Furthermore, the measure of linearity should be considered, such as including aspects of correlation between the evolved nonlinear difference of the response function and the TLM perturbations to investigate differences in spatial structure.

3.4 Conclusions

A case study of Hurricane Florence (2018) was performed to evaluate adjoint sensitivity analysis for TC intensity using a traditional surface pressure response function (-μ, minus the perturbation dry air mass in the column - a surrogate for surface pressure perturbation). Adjoint sensitivities at the initial time were optimally perturbed and evolved in the nonlinear and tangent linear model to evaluate the change in the perturbed simulation.

The adjoint sensitivity analysis suggests that TC intensity is particularly sensitive to the low-level temperature and winds, and to a lesser extent to moisture. While perturbations to the initial state maximize in the lower troposphere as the simulation evolves, the maximum perturbed energy grows into the upper troposphere and lower stratosphere. This upward growth motivates a vertical partitioning of the initial condition optimal perturbations. Three experiments were conducted to compare how perturbations to the full model domain (FPE) contrast to perturbations to only the upper (UPE) or lower (LPE) model domain. While the lowest sea level pressure is found in the FPE, on average the UPE decreases the SLP more and over a larger area. Furthermore, while the UPE satisfies the tangent linear assumption well, the FPE and LPE do not, even for a moist case.

From the evolution of the perturbed state, it is identified that the UPE better develops the outflow layer anticyclone and radial outflow, thereby helping evacuate mass from the low-level vortex. Viewed from a vorticity perspective, this better developed outflow supports lower-tropospheric vortex stretching thereby enhancing the spin-up of the low-level vortex. The initial perturbations in the LPE and FPE are largest in the lower troposphere and progressively extend to the upper troposphere. It is hypothesized that this reduces the TC's ability to intensify, as mass in the low-levels does not have a comparable outflow to support continued development. This hypothesis is supported through the evolved perturbations in the TLM. The TLM perturbations across all three experiments have the same horizontal distribution, however, the magnitude of the change is different. The UPE has substantially larger extremes in the response function domain perturbed -μ than in

the LPE or FPE. The TLM perturbations also show a shift in the track, this motivates further analysis of how the response function is defined.

Further case study experiments are necessary to evaluate whether this is a case dependent feature. Additionally, through the vertical partition in this chapter, optimal perturbations were re-scaled to prescribe the same change across all experiments. This vertical partitioning can also be completed without re-scaling perturbations to test whether the small perturbations to the upper troposphere alone continue to drive development and satisfy the tangent linear assumption well.

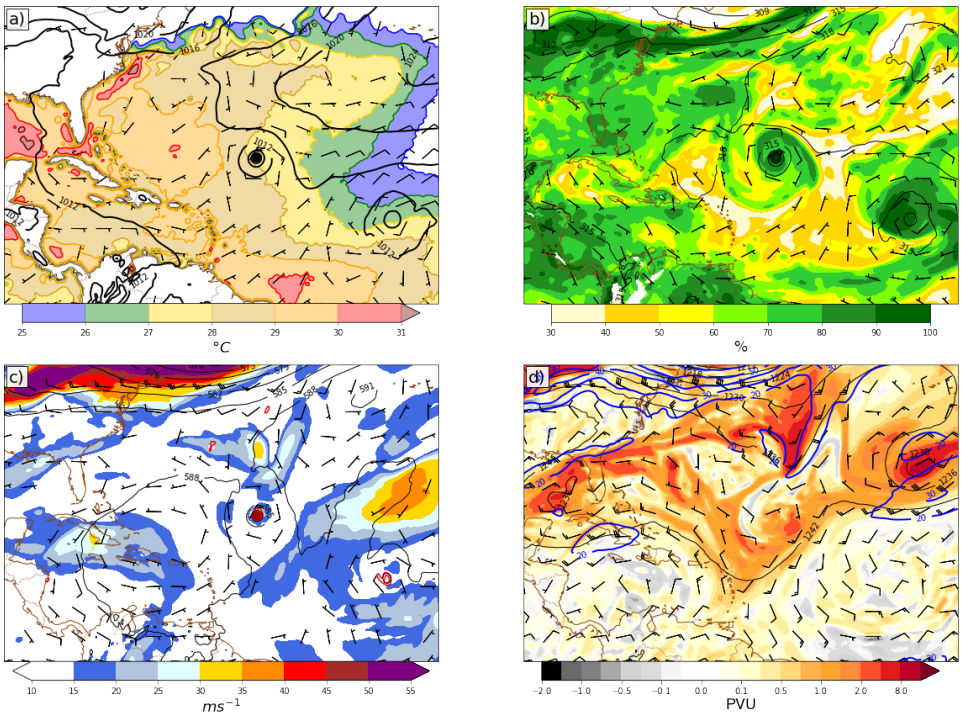

FIGURE 3.1: Valid 0000 UTC 9 September 2018 a) Sea surface temperatures (fill; $°C$), sea level pressure (black; hPa) and 10 m wind (barbs; ms^{-1}), b) 850-700 hPa average relative humidity (fill; %), 700 hPa geopotential height (black; m), and wind (barbs;ms^{-1}), c) 850–200 hPa vertical wind shear (fill; ms^{-1}), 500 hPa relative vorticity (red; $10^5 s^{-1}$), geopotential height (black; m), and wind (barbs;ms^{-1}), d) 200 hPa potential vorticity (fill; PVU), wind speed (blue; ms^{-1}), geopotential height (black; m), and wind (barbs;ms^{-1})

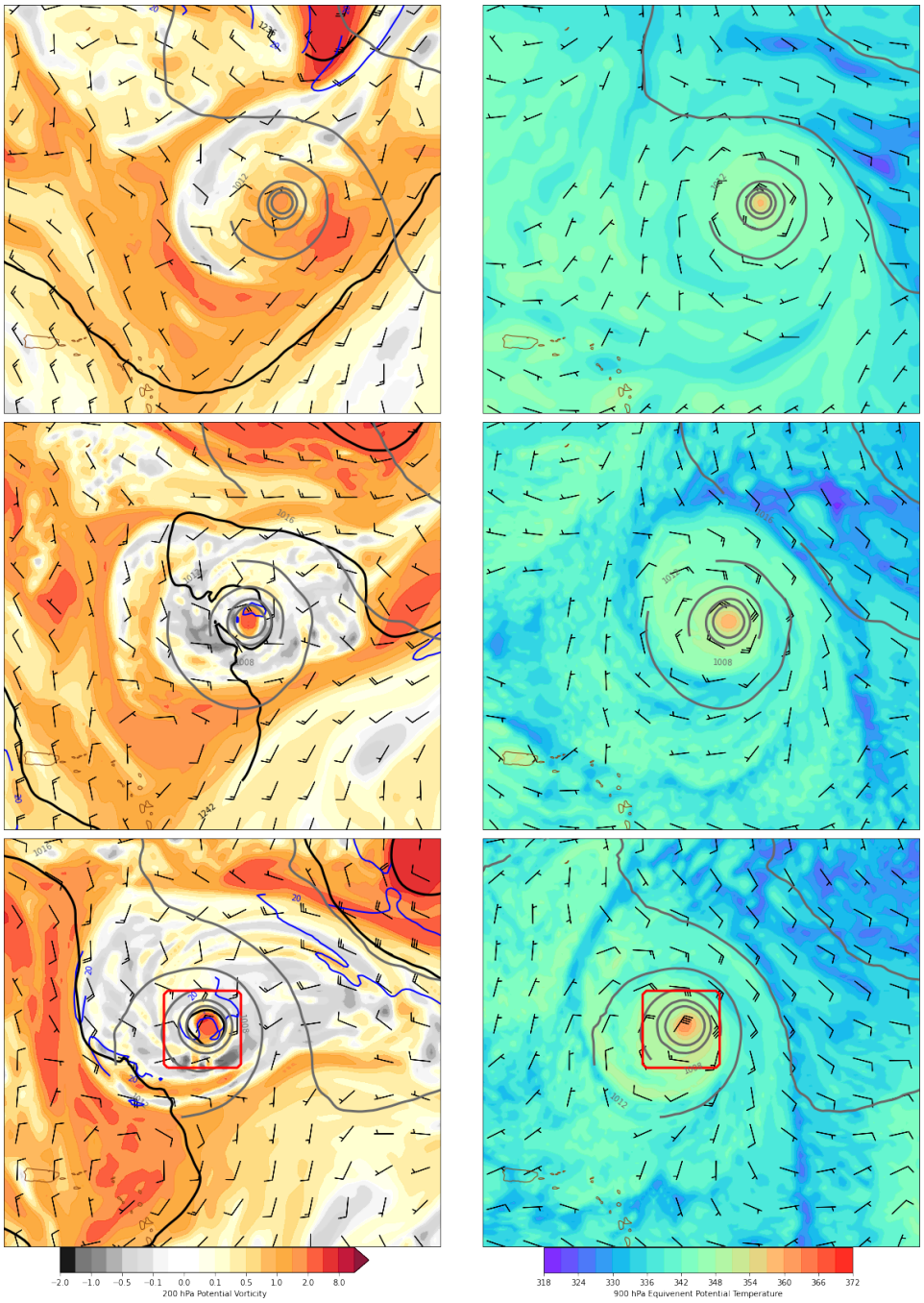

FIGURE 3.2: Right panels 200 hPa potential vorticity (fill; PVU), wind speed (blue; ms^{-1}), geopotential height (black; m), wind (barbs;ms^{-1}), and SLP (grey; hPa). Left panels 900 hPa equivalent potential temperature (fill; K), wind (barbs;ms^{-1}), and SLP (grey; hPa). Valid at a-b) 0000 UTC 9 September, c-d) 1800 UTC 9 September, and e-f) 1200 UTC 10 September. Red box denotes horizontal size and location of response function.

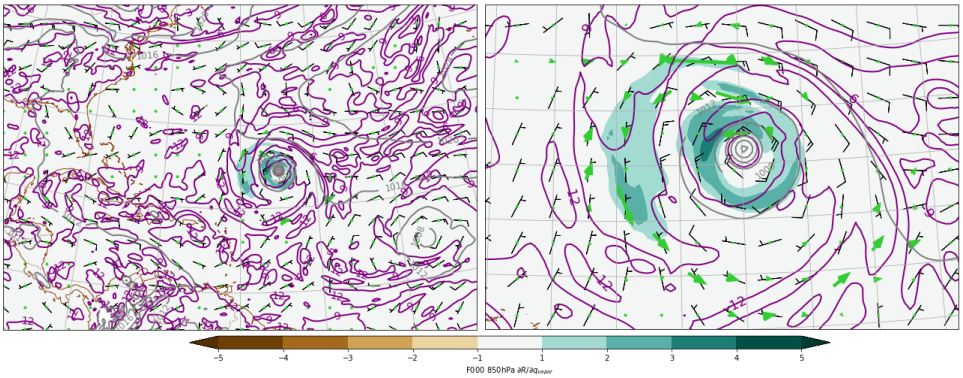

FIGURE 3.3: The 850 hPa adjoint sensitivity to water vapor (color scale by maximum value on that level; Pa / g kg^{-1}), sensitivity to horizontal winds (vectors; ms^{-1}), water vapor (solid purple line every 3 g kg^{-1}), sea level pressure (solid grey line every of 4 hPa) and wind (barbs; ms^{-1}) at initial time of valid at 0000 UTC 9 September 2018

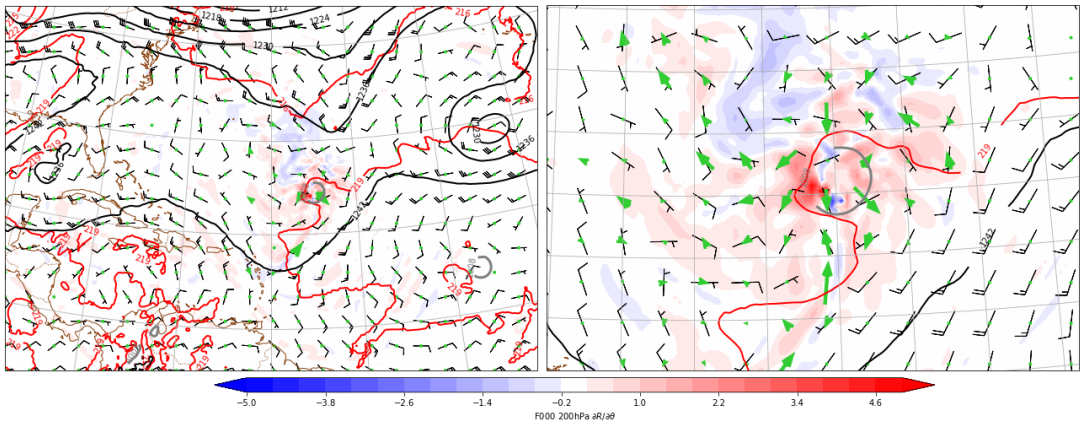

FIGURE 3.4: The 200 hPa adjoint sensitivity to potential temperature (color scale by maximum value on that level; Pa / K), sensitivity to horizontal winds (vectors), 200 hPa potential temperature (solid red line every 2 K), wind speed (solid blue line every 5 ms^{-1} above 15 ms^{-1}), geopotential height (solid black line every of 60 m) and wind (barbs; ms^{-1}) at initial time of valid at 0000 UTC 9 September 2018.

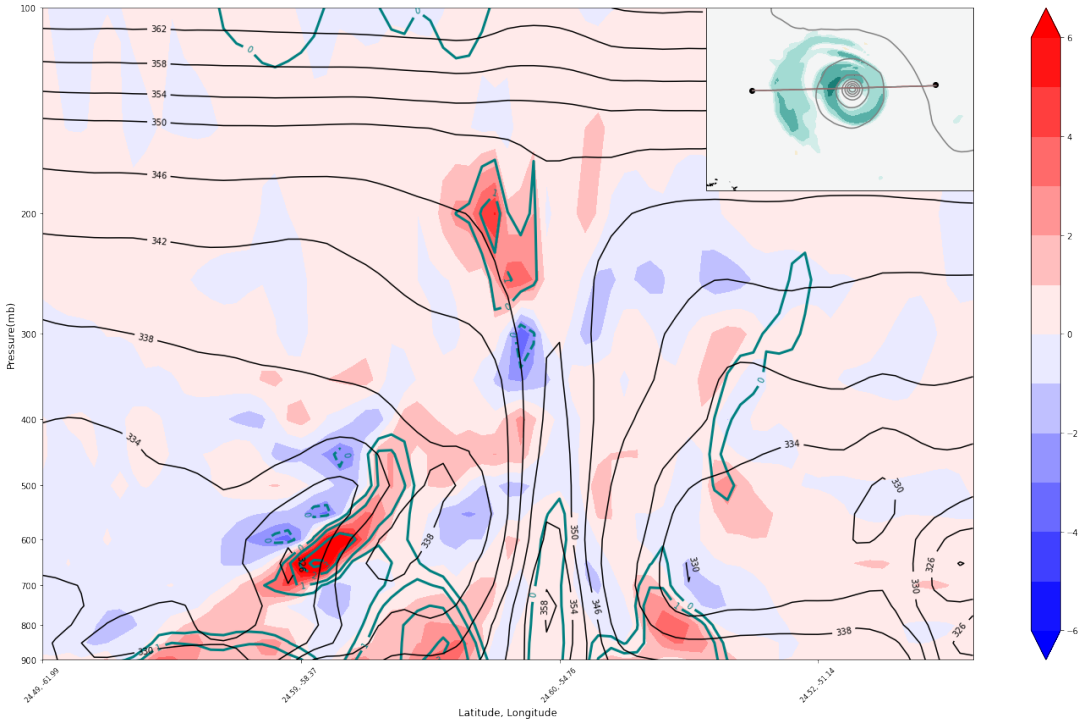

FIGURE 3.5: The adjoint sensitivity to potential temperature (fill, Pa / K), sensitivity to water vapor (teal every 1 g kg^{-1}), equivalent potential temperature (solid black line every 4 K). Inset is the 850 hPa adjoint sensitivity to water vapor and sea level pressure as in Fig 3.3, with the cross section orientation shown. Valid at 0000 UTC 9 September 2018.

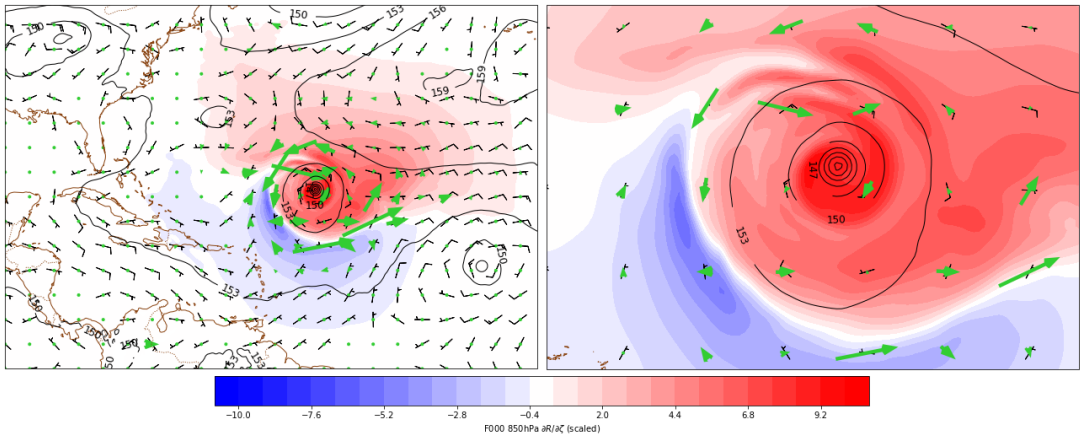

FIGURE 3.6: The 850 hPa adjoint sensitivity to vorticity (color scale by maximum value on that level; Pa / s^{-1}), sensitivity to horizontal winds (vectors), positive relative vorticity (solid orange line scale by 1e5 every 5 s^{-1}), geopotential height (solid black line every of 60 m) and wind barbs (ms^{-1}) valid at 0000 UTC 9 September 2018.

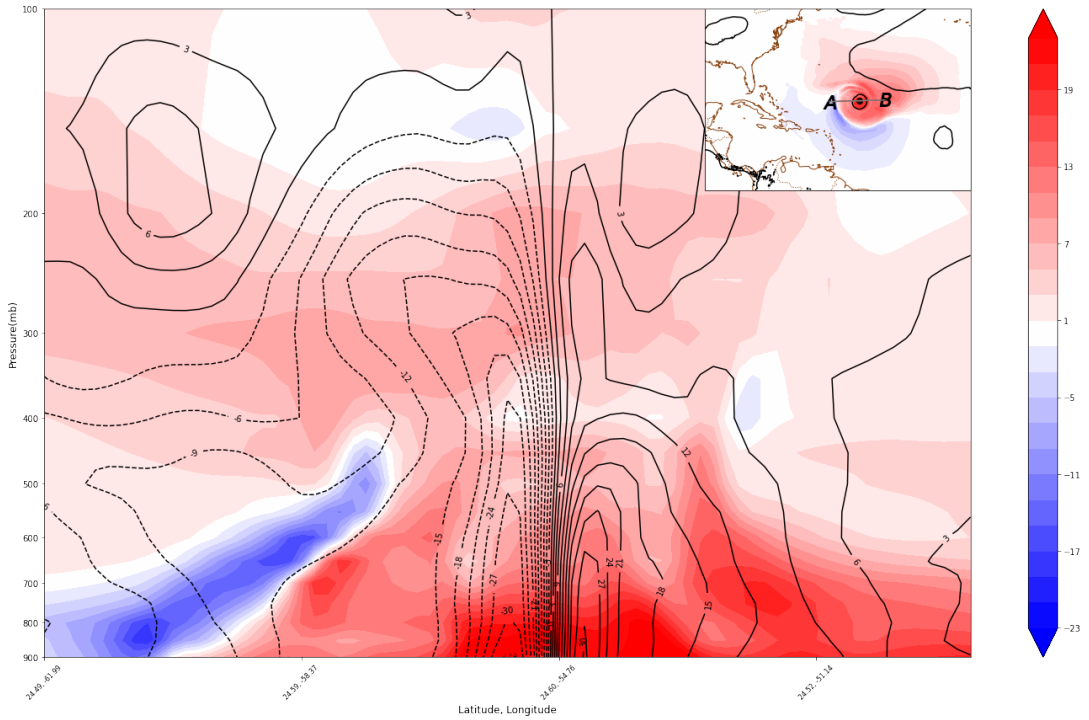

FIGURE 3.7: The adjoint sensitivity to vorticity (fill, Pa / s^{-1}), meridional wind (solid black line every 3 ms^{-1}). Inset is the 850 hPa adjoint sensitivity to vorticity and geopotential height as in Fig 3.6, with the cross section orientation shown. Valid at 0000 UTC 9 September 2018.

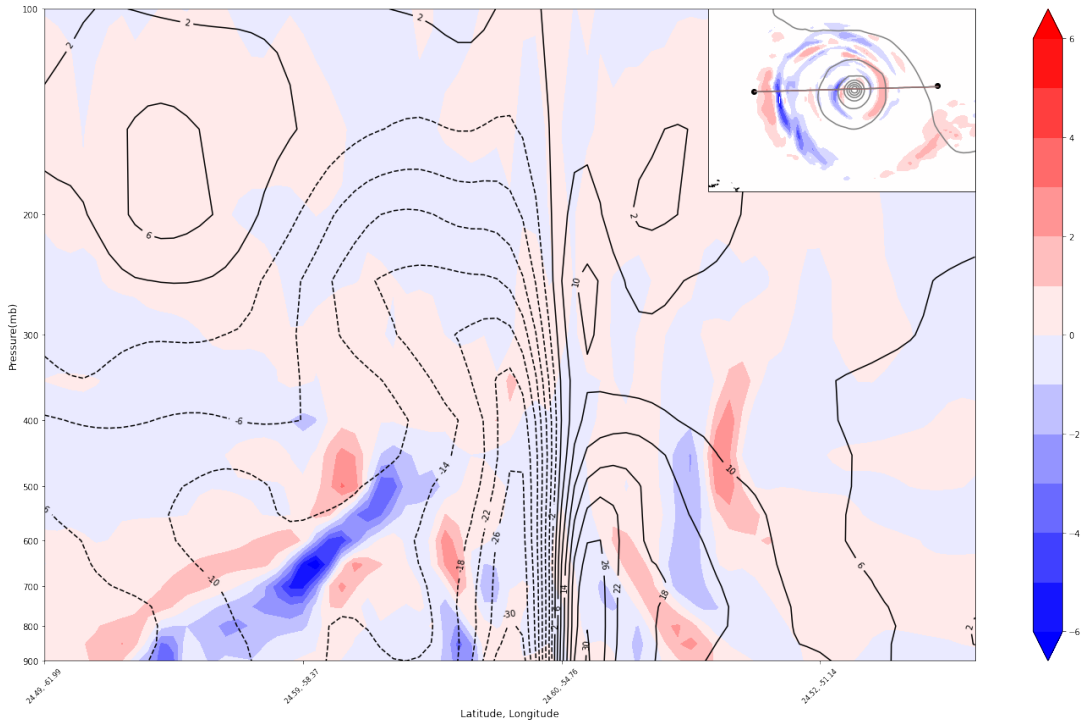

FIGURE 3.8: The adjoint sensitivity to meridional wind (fill, Pa / ms^{-1}), meridional wind (solid black line every 3 ms^{-1}). Inset is the 850 hPa adjoint sensitivity to meridional wind and SLP with the cross section orientation shown same as Fig 3.5. Valid at 0000 UTC 9 September 2018.

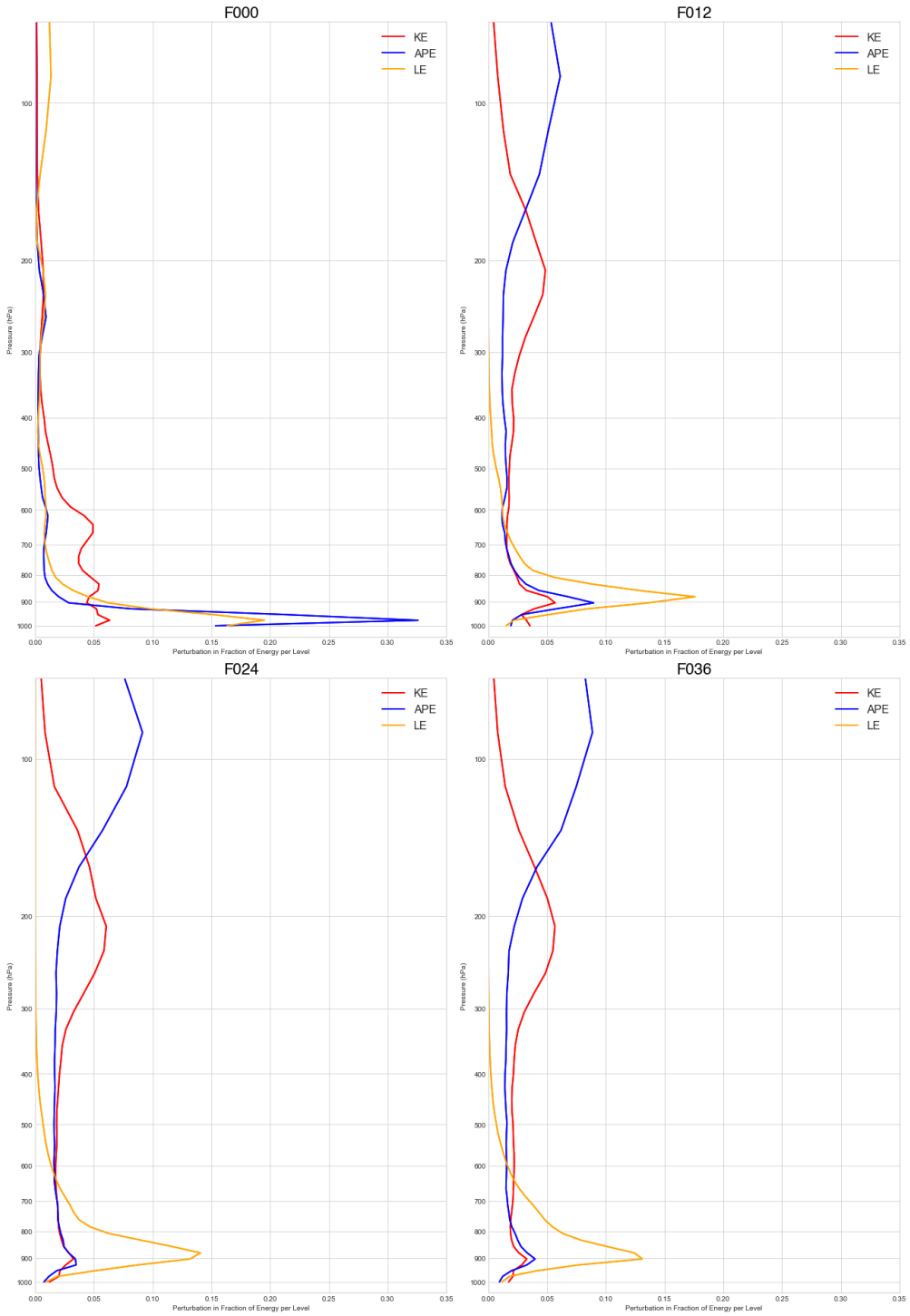

FIGURE 3.9: Perturbation of the kinetic energy (KE; red), available potential energy (APE; blue), and latent heat energy (LE; orange) normalized by the total change in their respective energy. Valid at forecast hours F00, F12, F24, and F36.

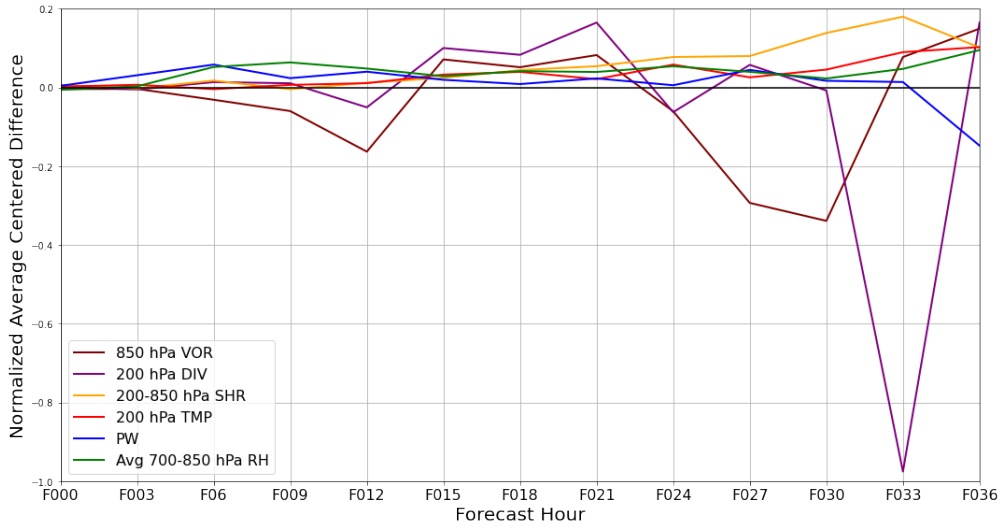

FIGURE 3.10: The normalized (difference divided by control value) storm relative averaged difference for each defined SHIPS-related variable. All values are calculated from a radius starting at the TC center, defined as the 850 hPa maximum vorticity. Variables 850 hPa relative vorticity (scaled by 1) from 0-1000 km radius (maroon), 200 hPa divergence (scaled by 1) from 0-1000 km (purple), 850 to 200 hPa vertical wind shear (scaled by 10) from 200-1000 km radius (yellow), 200 hPa temperature (scaled by 1000) centered from 0-1000 km radius (red), precipitable water (scaled by 10) centered from 100-200 km radius (blue), 700 to 850 hPa average relative humidity (scaled by 10) centered from 200-800 km radius (green). The values are scaled for ease of view.

.

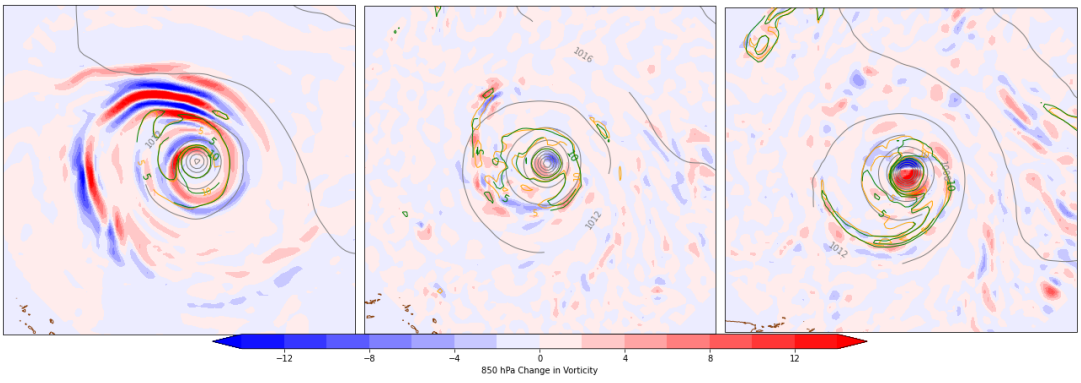

FIGURE 3.11: The 850 hPa vorticity (fill), control positive relative vorticity (solid green line scale by 1e5 every 5 s^{-1}), perturbed positive relative vorticity (solid orange line scale by 1e5 every 5 s^{-1} below 15), SLP (solid gray line every 4 hPa above 980 hPa). Valid at F00, F18, and F36. Perturbations at time F00 scaled by 10.

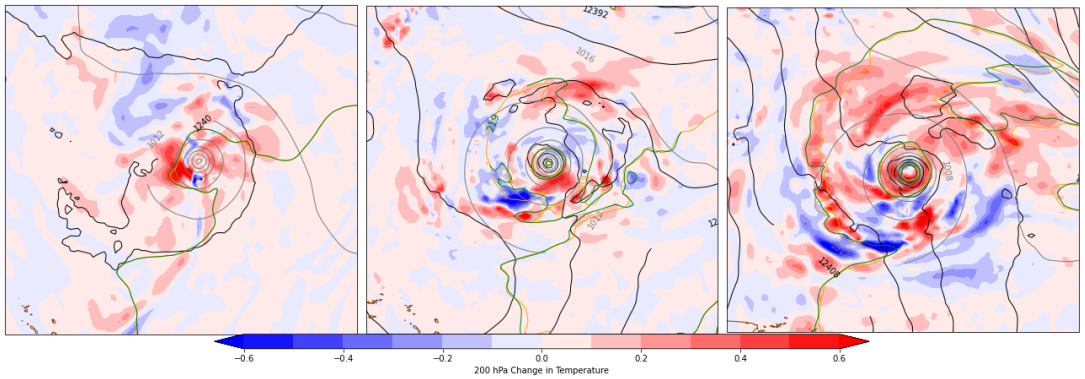

FIGURE 3.12: Perturbation 200 hPa temperature within 1000 km of TC center (fill; K), control temperature (solid orange line; K), perturbed temperature (solid green; K), SLP (solid gray line every 4 hPa above 980 hPa). Valid at F00, F18 and F36).

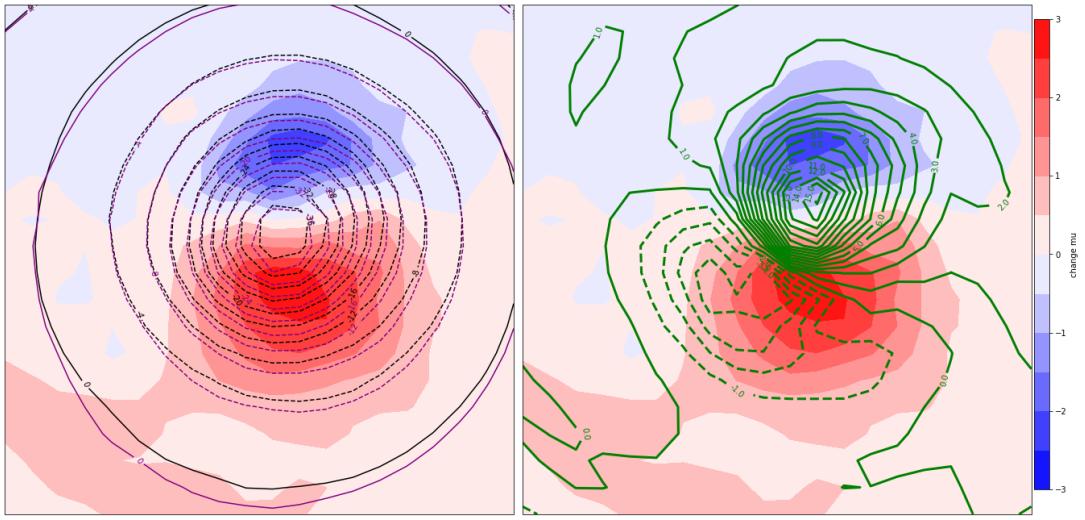

FIGURE 3.13: Valid 1200 UTC 10 September 2018 within response function domain. Change in response function ($-\mu$) (fill; hPa). Control simulation μ (black contour every 4 hPa), perturbed simulation μ (purple contour every 4 hPa), tangent linear perturbation (green contour every 1 hPa).

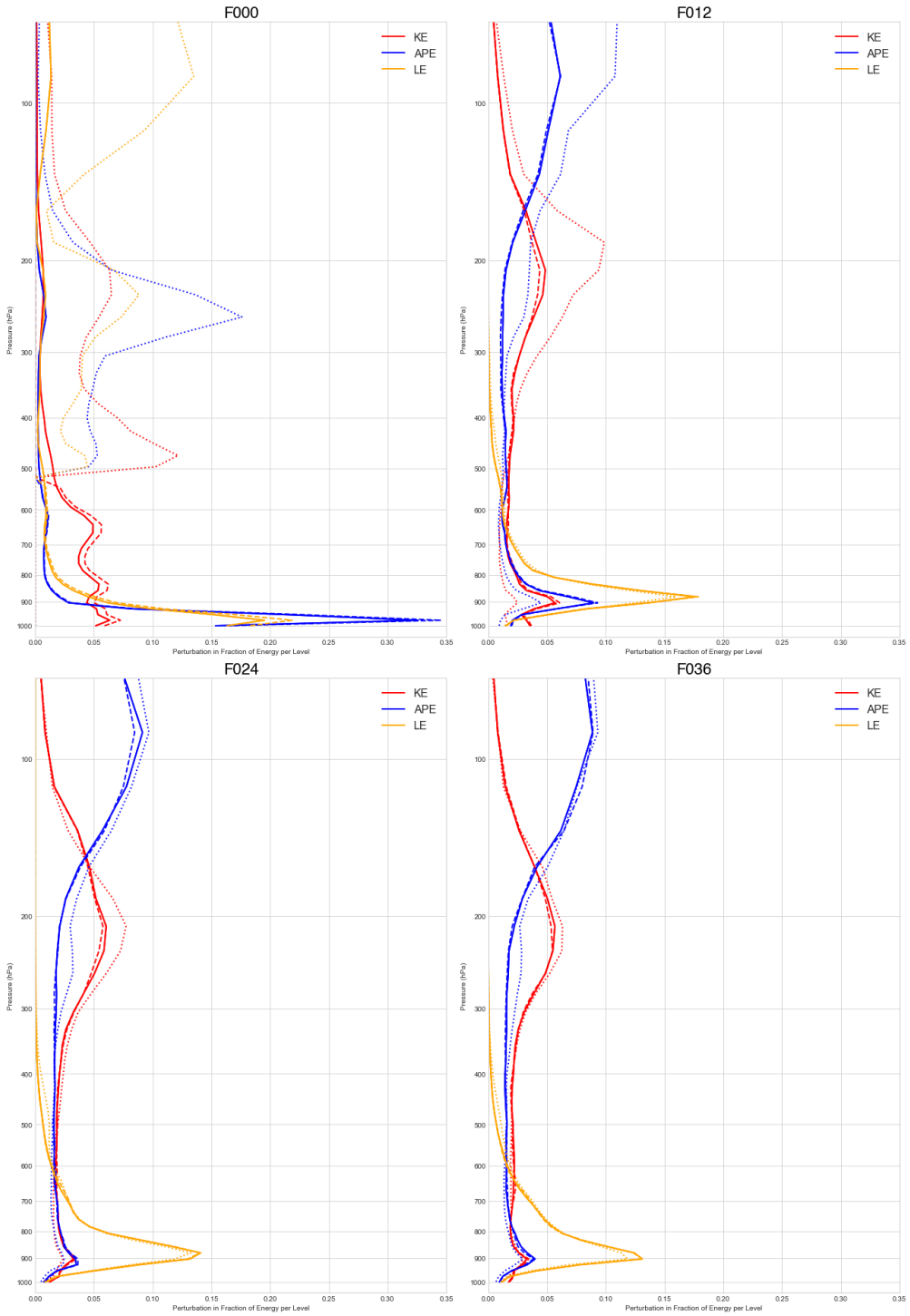

FIGURE 3.14: As in Fig 3.9, except with lower perturbations only (dashed line) and upper perturbations only (dotted line). Full domain perturbation is identical (solid line).

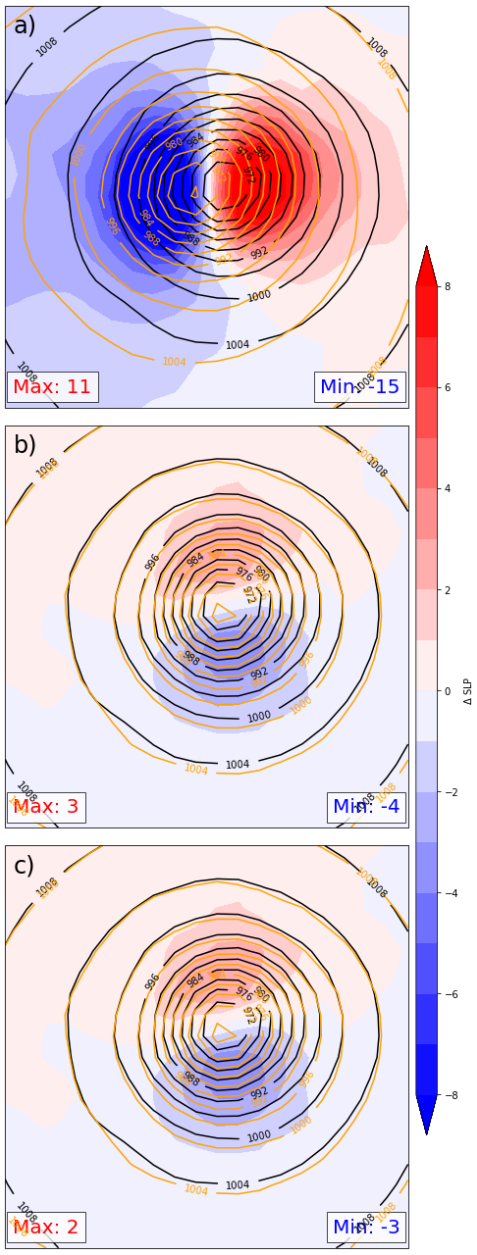

FIGURE 3.15: Valid 1200 UTC 10 September 2018 within response function domain for a) UPE, b) LPE, and c) FPE. Change in SLP (fill; hPa), control simulation SLP (black contour every 4 hPa), perturbed simulation SLP (orange contour every 4 hPa). Maximum and minimum values are from perturbed minus control of each respective simulation.

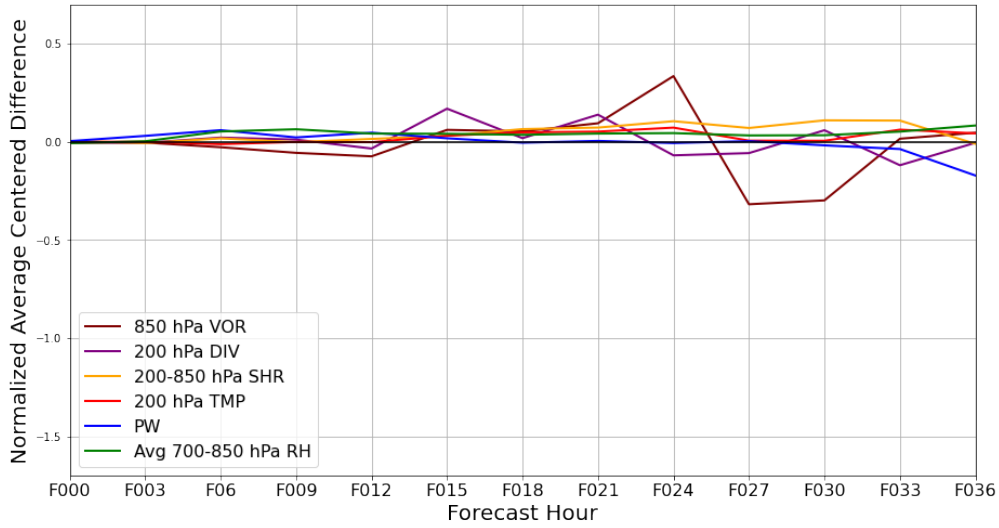

FIGURE 3.16: The normalized storm relative average difference for each defined SHIPS-related variable as in Fig 3.10 except in LPE.

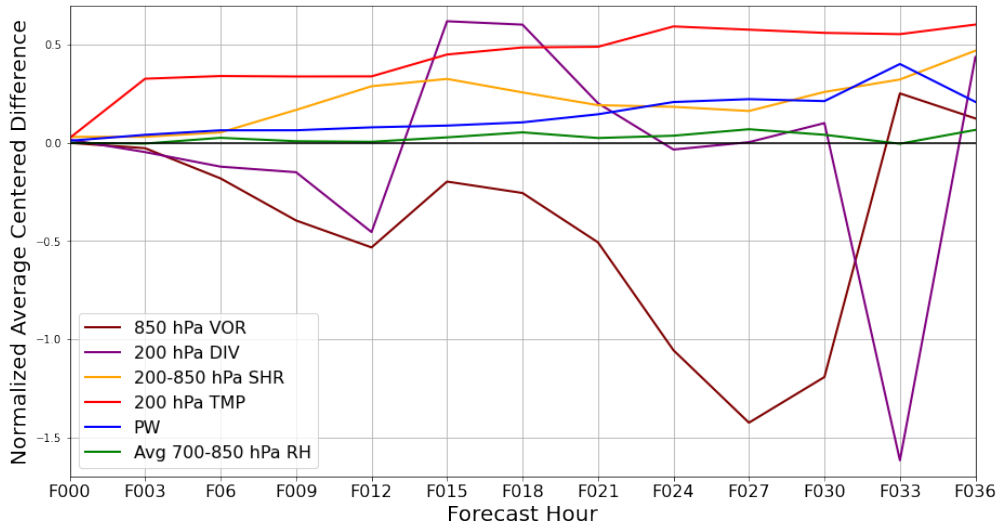

FIGURE 3.17: The normalized storm relative average difference for each defined SHIPS-related variable as in Fig 3.10 except in UPE.

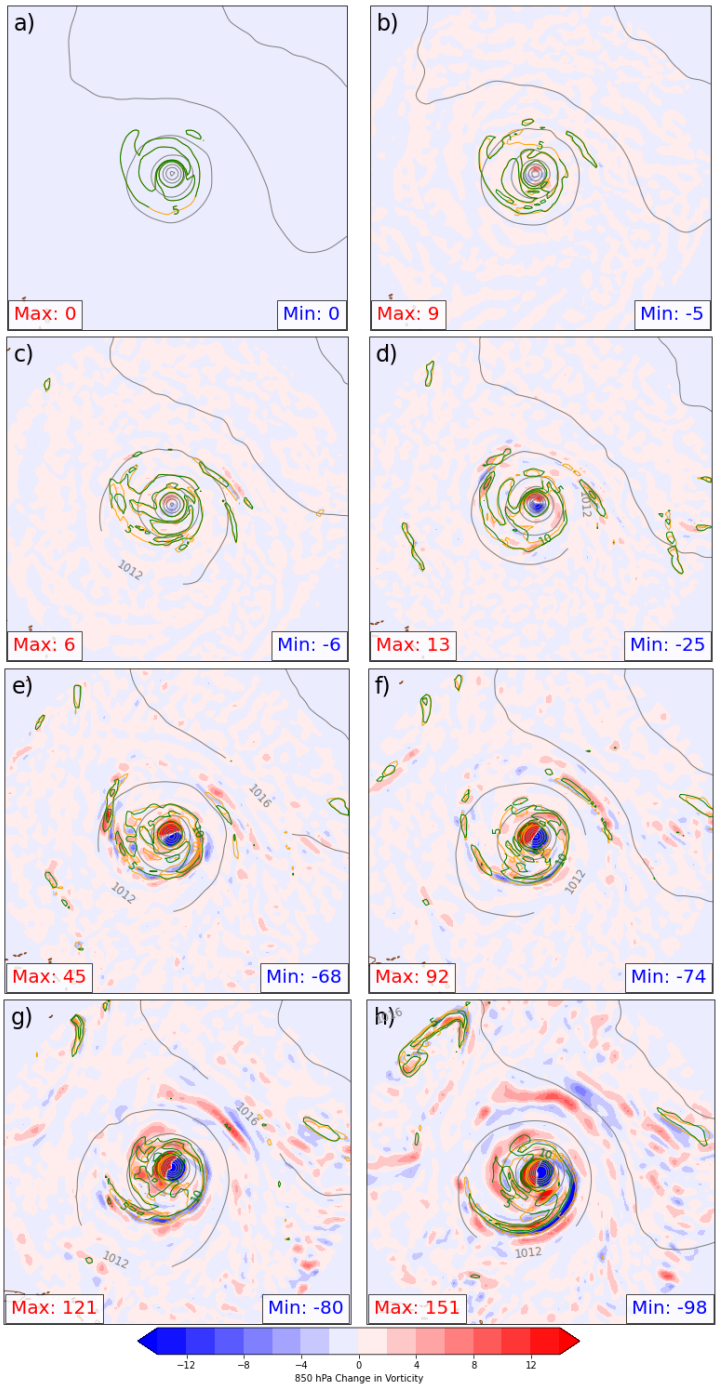

FIGURE 3.18: The 850 hPa vorticity as in Fig 3.11. Valid at a) F00, b) F03, c) F06, d) F12, e) F18, f) F24, g) F30 and h) F36. Maximum and minimum values are from perturbed minus control.

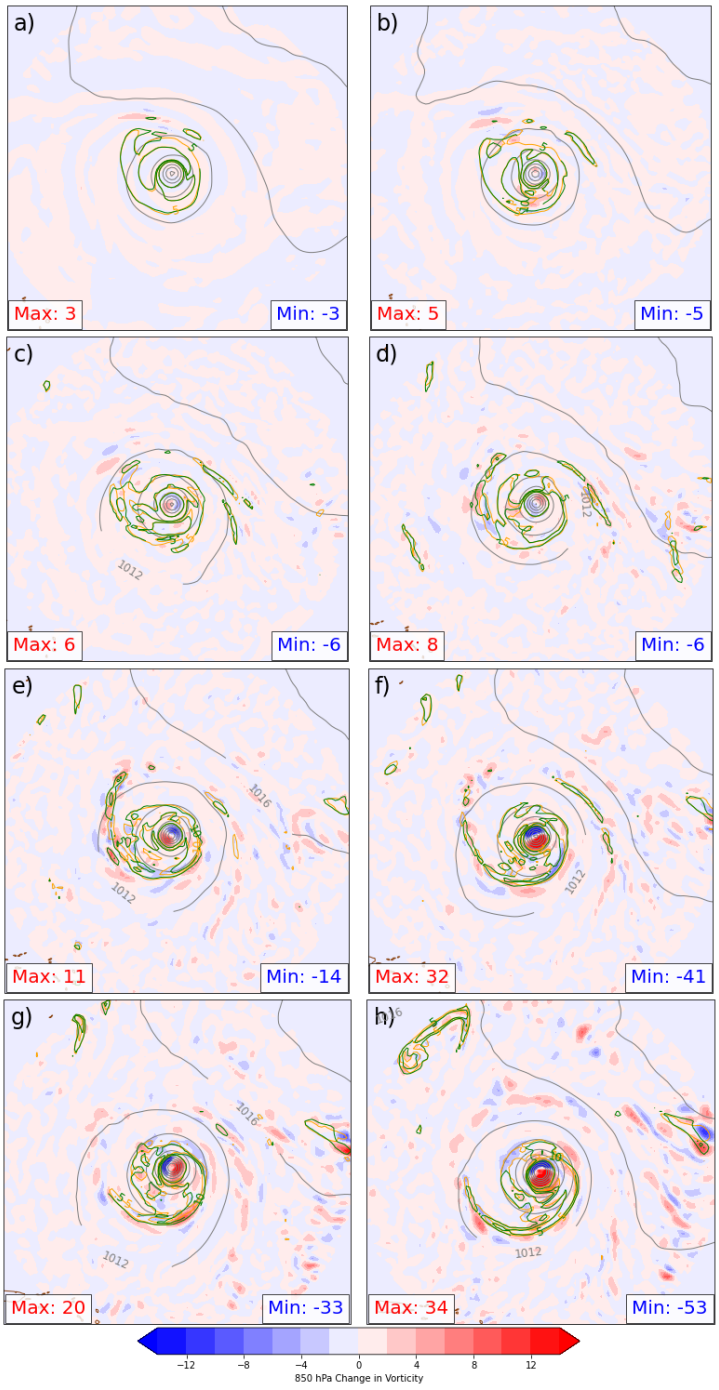

FIGURE 3.19: The 850 hPa vorticity as in Fig 3.11. Valid at a) F00, b) F03, c) F06, d) F12, e) F18, f) F24, g) F30 and h) F36. Maximum and minimum values are from perturbed minus control.

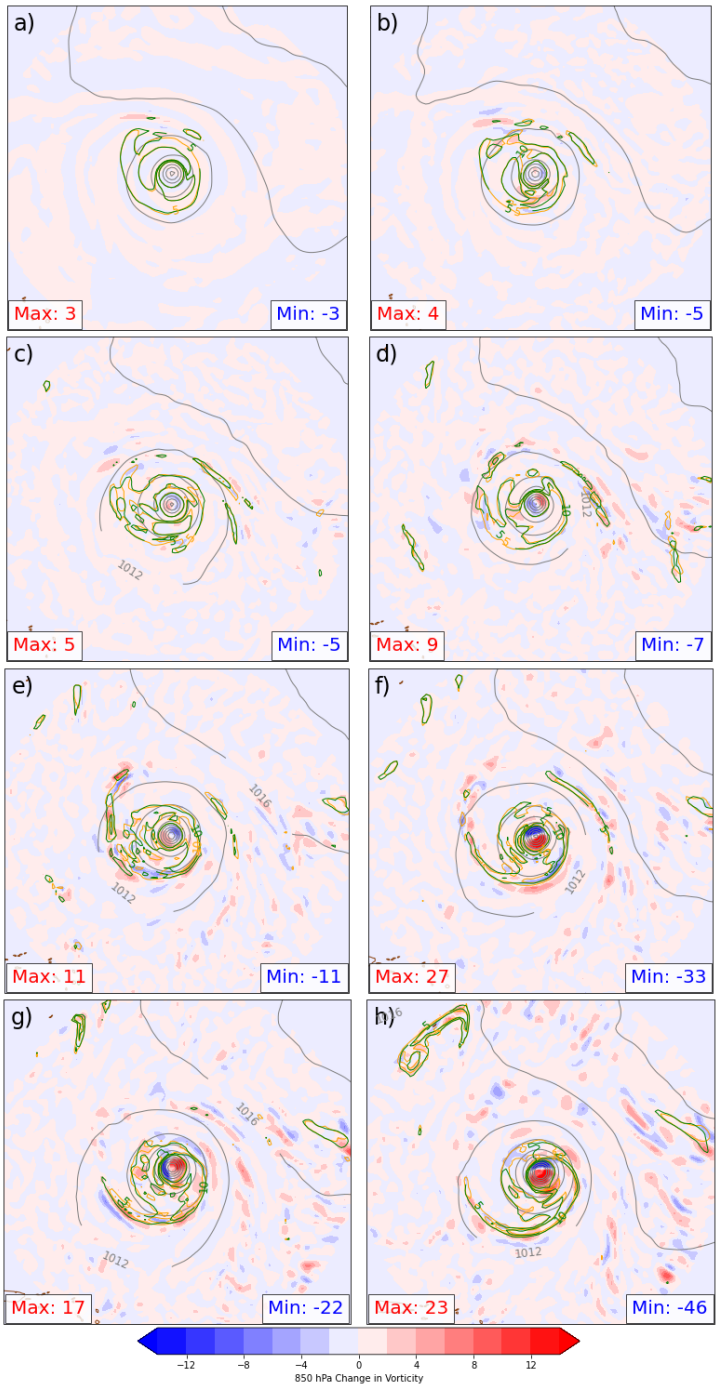

FIGURE 3.20: The 850 hPa vorticity as in Fig 3.11. Valid at a) F00, b) F03, c) F06, d) F12, e) F18, f) F24, g) F30 and h) F36. Maximum and minimum values are from perturbed minus control.

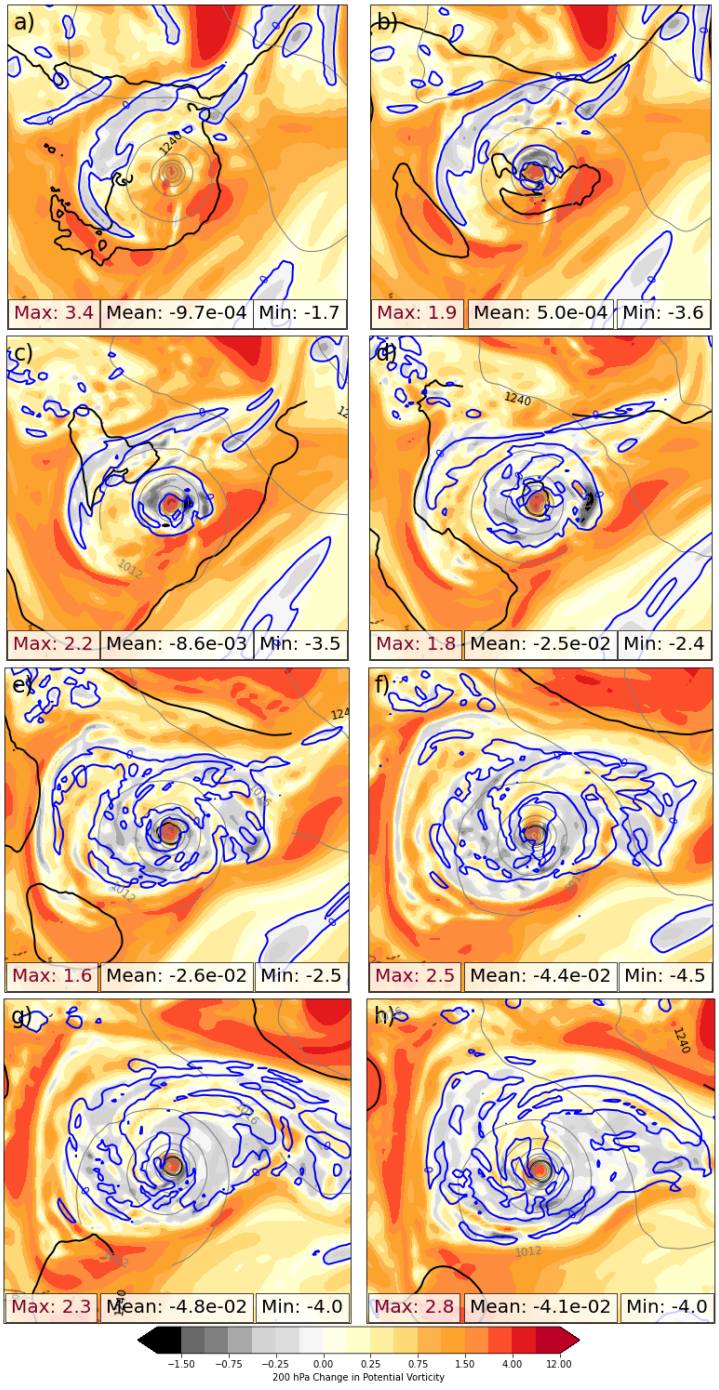

FIGURE 3.21: The 200 hPa PV from UPE (fill; PVU), control simulation zero contour (blue; PVU), geopotential height (black line every 8 dm). Valid at a) F00, b) F03, c) F06, d) F12, e) F18, f) F24, g) F30 and h) F36. Maximum, minimum, and mean values are from perturbed minus control within area shown.

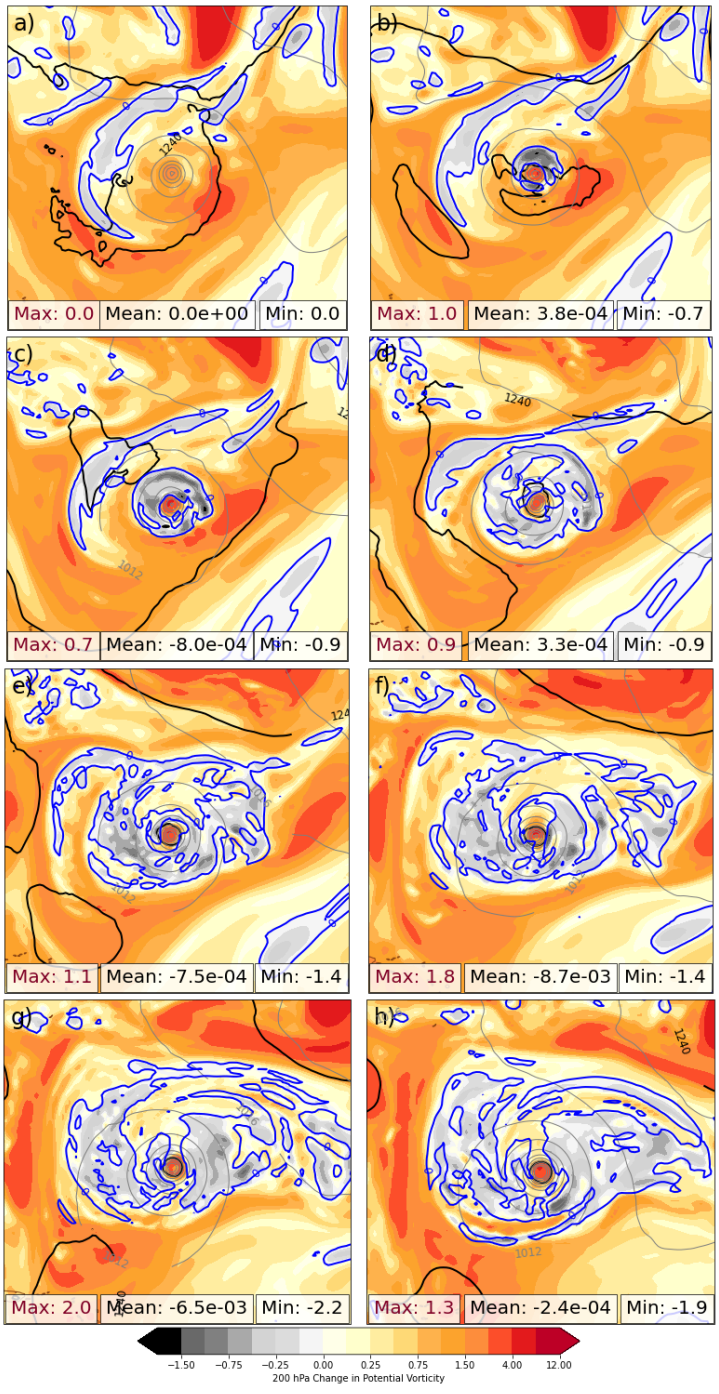

FIGURE 3.22: Same as Fig 3.21 except for the LPE.

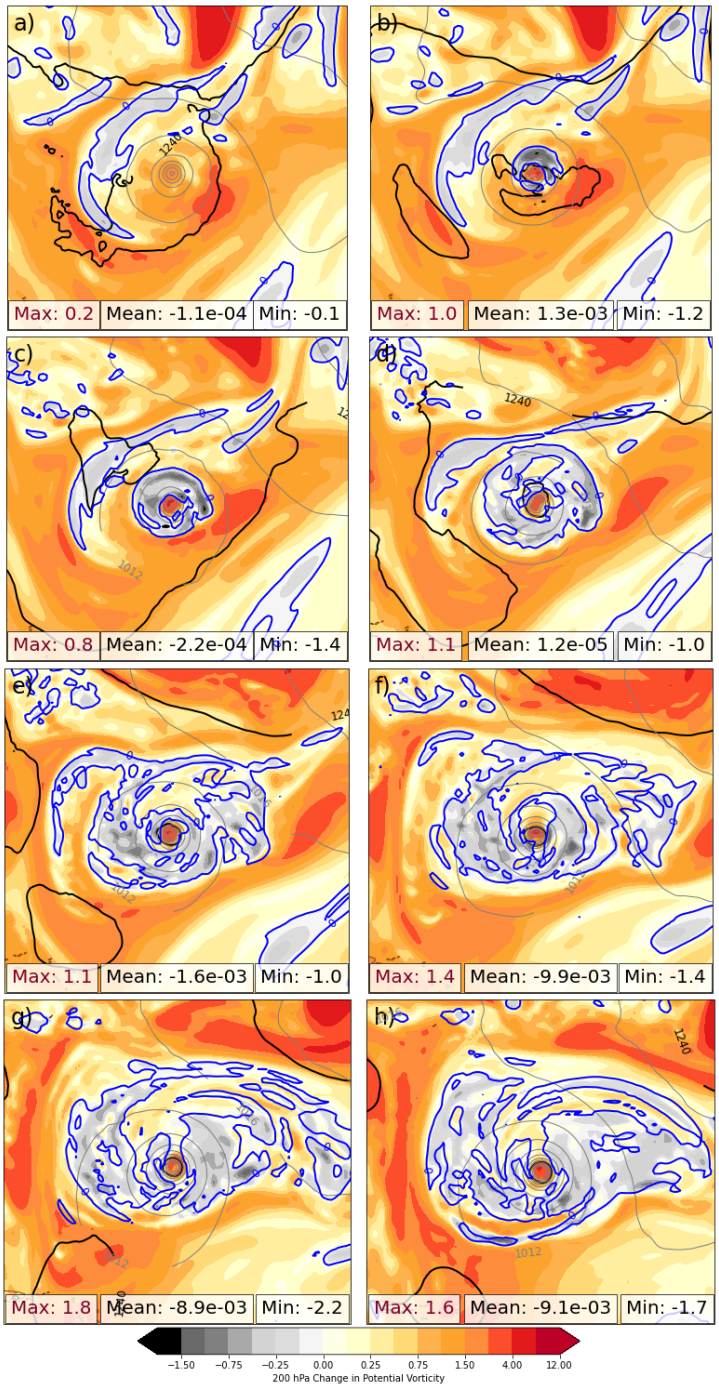

FIGURE 3.23: Same as Fig 3.21 except for the FPE.

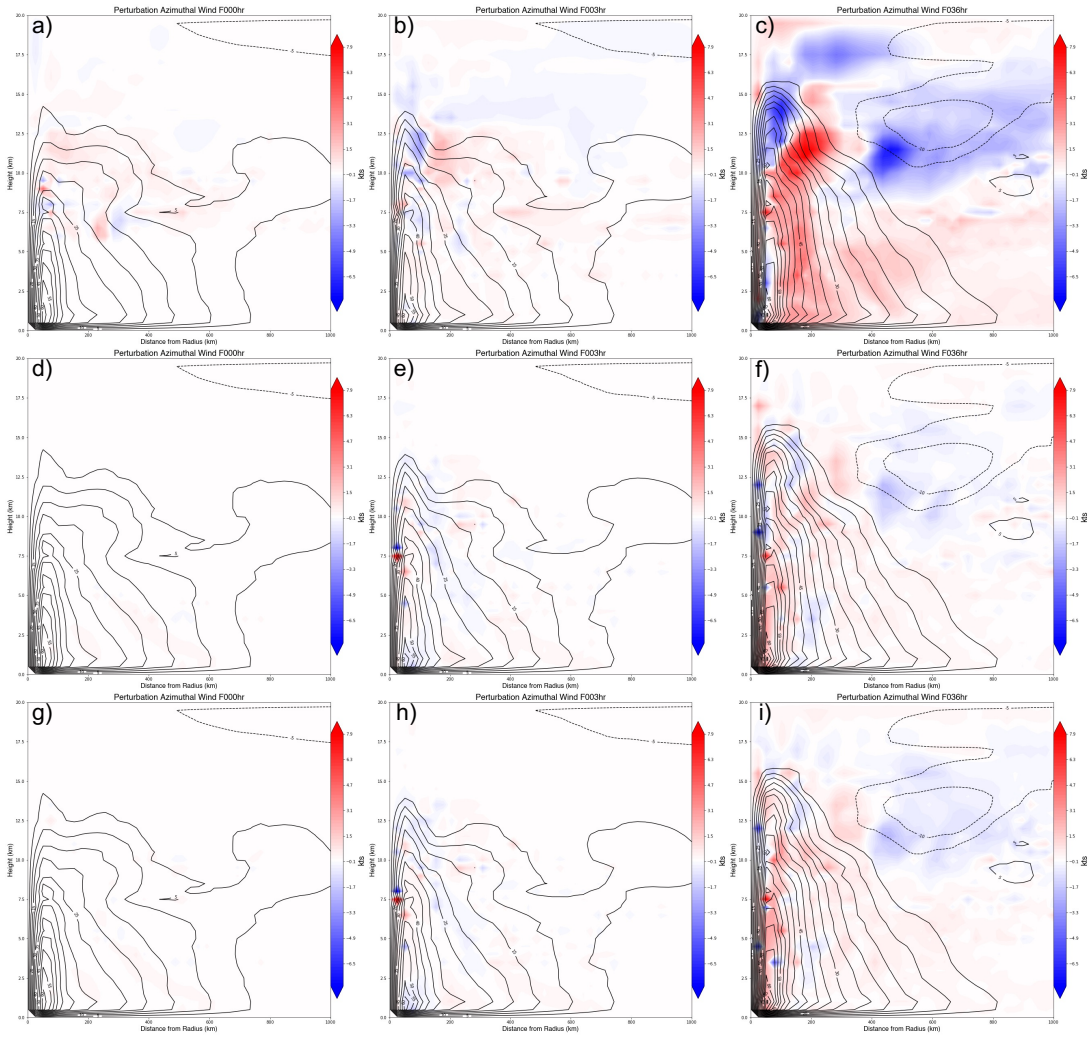

FIGURE 3.24: Azimuthally averaged from TC center to 1000 km for UPE (a-c), LPE (d-f), and FPE (g-i): storm center relative difference azimuthal wind (fill; kts), control azimuthal wind (black contour every 5 kts). Valid at F00 (a,d,g), F03 (b, e, h), and F36 (c,f,i).

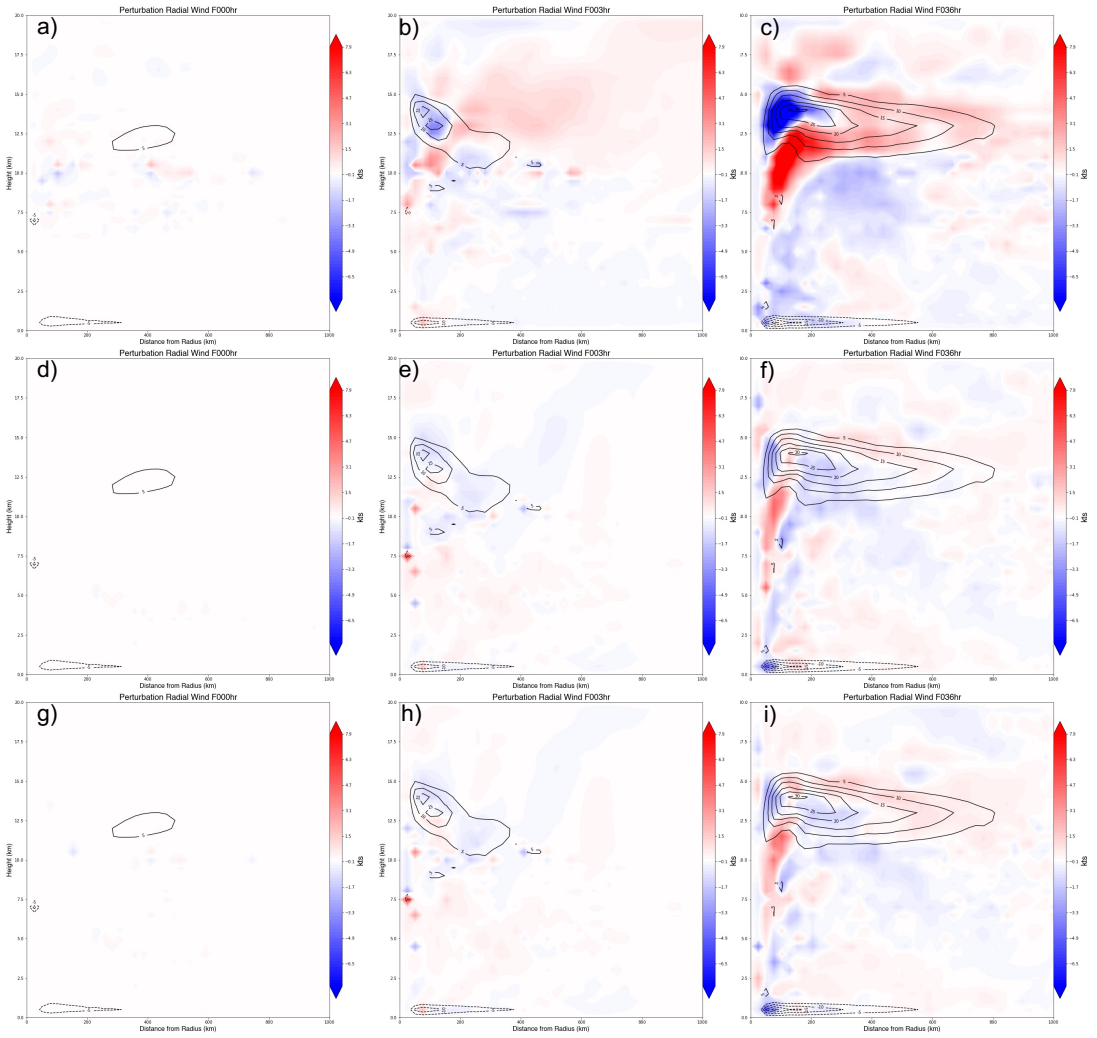

FIGURE 3.25: Sames as Fig 3.24 except for radial wind.

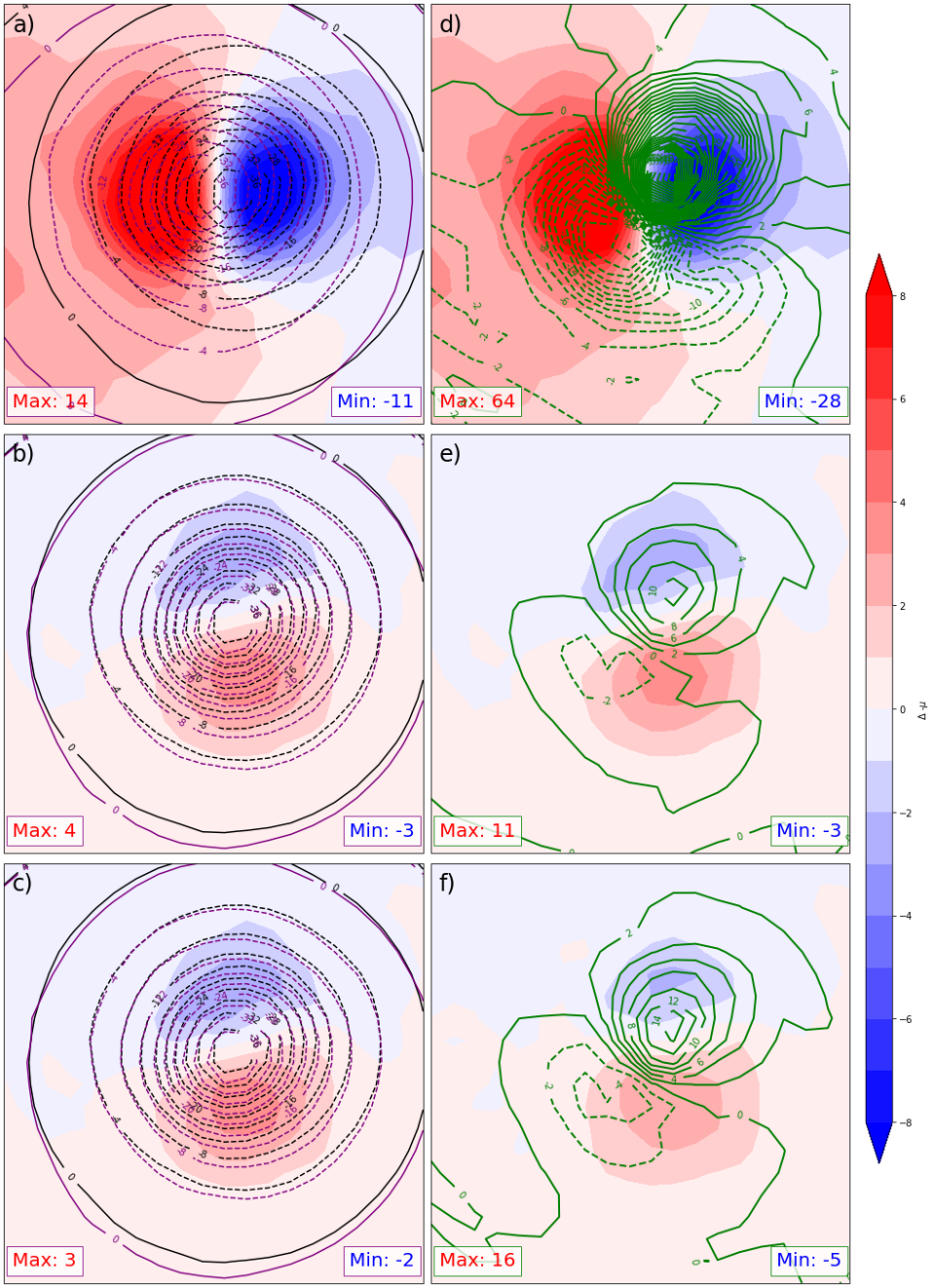

FIGURE 3.26: Valid 1200 UTC 10 September 2018 within response function domain for a and d) UPE, b and e) LPE, and c and f) FPE. Change in response function ($-\mu$) (fill; hPa), control simulation μ (black contour every 4 hPa), perturbed simulation μ (purple contour every 4 hPa), tangent linear perturbation (green contour every 1 hPa). Maximum and minimum values are from NLM perturbed minus control (left column) and TLM (right column) in each respective simulation.

Chapter 4

A comparison of TC intensity metrics in an adjoint model

4.1 Overview

An adjoint model calculates how an aspect of the final state of a numerical weather prediction (NWP) model (called a response function, R) changes due to small changes to the initial model state ($\mathbf{x_0}$) or at any other model time prior to the final forecast state (Errico, 1997). Through a single integration of the adjoint model, the adjoint model calculates the sensitivity of the response function to all state variables. For an adjoint study to be useful, the defined response function must correctly represent the forecast characteristic of interest (e.g., intensity, steering flow, forecast error). The effectiveness of a response function is impacted by both size of the region in which the response function is defined

and variable(s) used to define the response function (Hoover and Morgan, 2010). If the response function domain (RFD) is too small, perturbed forecasts using adjoint-informed initial perturbations may shift the feature of interest outside the RFD. Furthermore, careful consideration of how the response function is defined is necessary to ensure that the feature of interest is actually being measured. Examples of this can be found with an application of instantaneous tropical cyclone (TC) steering sensitivities (Hoover and Morgan, 2011), where careful construction of a response function is necessary to separate the background steering flow from the flow associated with the TC. Adjoint sensitivity analysis is one of many approaches to used to explore the predictability of numerical weather prediction forecasts. Other objective sensitivity methods include singular vectors (e.g., Peng and Reynolds 2006) and ensemble sensitivity analysis (e.g., Ancell and Mass 2006).

Tropical cyclone intensity change forecasts require a similar careful approach, complicated by the discussions of how to best represent intensity. Tropical cyclone intensity is historically defined by the strength of surface winds and/or the minimum central pressure of the storm by the National Hurricane Center (Rappaport et al., 2009). Holland and Merrill (1984) defined a TC's strength as the magnitude of the cyclonic circulation in the region outside the inner core. A TC's intensity can also be related to the strength of the overturning thermal circulation, as typically represented through the conceptual model of the Carnot Cycle (Emanuel, 1986). The discussion surrounding how to define a TC's intensity, or potential intensity, has been a long-established conversation that has limited discussion of the physical understanding that links the different definitions

(Chavas et al., 2017). Furthermore, discussions in the TC community have considered the intensity through the lens of how the hazards of the TC presents (e.g., storm surge, flooding) as those metrics may be more directly understandable to populations impacted by land falling TCs.

An established framework to evaluate expected TC intensity change is the Statistical Hurricane Intensity Prediction Scheme (SHIPS; DeMaria and Kaplan 1994) and the SHIPS Rapid Intensity Index (SHIPS-RII; Kaplan et al. 2010). The statistical techniques SHIPS and SHIPS-RII evaluate a combination of current conditions, including satellite data, persistence metrics, and model forecast data. Through historical data sets, an established statistical relationship between these metrics and expected intensity change has been established to relate each variable to TC intensity through a weighted coefficient. Aspects of this framework are used in the present study, particularly, evaluating the change of synoptic scale variables in the horizontal and vertical range used in SHIPS(RII). The metrics evaluated are the average 200 hPa temperature and divergence within a 1000 km radius, the 850 hPa relative vorticity within a 1000 km radius, the 700-850 hPa average relative humidity within a 200 - 800 km radius, the 200-850 hPa vertical shear of the horizontal winds within a 200 - 1000 km radius, and the precipitable water within a 100 - 200 km radius. These variable definitions can also be found in Appendix A. While the regression coefficients established within SHIPS and SHIPS-RII literature cannot be used, the general relationship (e.g., sign of change) and magnitude of change can provide insights into changes of physical processes. Additionally, the distribution of change and the physical implications are evaluated within the context of this case study.

Previous adjoint sensitivity studies for tropical cyclone intensity change predominantly define intensity in terms of the (1) sea level pressure (Langland et al. 1995; Chu et al. 2011) or (2) the low-level wind fields (e.g., Doyle et al. 2011; Ito et al. 2011), either from the vorticity (Vukicevic and Raeder, 1995) or kinetic energy (Doyle et al. 2011; Doyle et al. 2012) within within a lower-tropospheric volume region surrounding the storm center, however, there is a limited extant of studies using adjoint sensitivity diagnostics applied to TC intensity. Ito et al. (2011) used adjoint sensitivity in a cloud-permitting, nonhydrostatic, axisymmetric model to examine the sensitivity of 1hr intensity forecasts for a mature TC to heat flux and surface wind stress, using the tangential velocity at the top of the boundary layer as a response function. Chu et al. (2011) employed the Weather Research and Forecasting (WRF) model and its adjoint to apply adjoint sensitivity techniques to a TC that had undergone rapid intensification (RI), finding low-level moisture exerts a strong influence on the final time forecast intensity. Chu et al. (2011) implemented the central sea level pressure as a response function. These sensitivities to moisture were verified by perturbing and evolving the areas of sensitivity with assimilated idealized observations. Doyle et al. (2012) utilized the Coupled Ocean-Atmosphere Mesoscale Predication System (COAMPS) and its adjoint to address the role of initial state wind, temperature, and moisture perturbations on tropical cyclogenesis in a developing and non-developing case. Applying a low-level kinetic energy response function, adjoint diagnostics identified low-level moisture and temperature perturbations were of greater importance than perturbations to the wind fields, and through perturbing the initial conditions identified a "bottom up" development process. With the exception of

Doyle et al. (2012), studies consider a single metric to define intensity. Furthermore, the justification for how the response function was selected is limited in how it best describes TC intensity in previous studies. When using an adjoint model, there will always be an answer, however, whether that answer has any relevance to the question asked is not certain. This results in the need to consider carefully the response function used to initiate the adjoint model in order to ensure the answer will be relevant.

Doyle et al. (2019) performed a study of extratropical cyclone "Desmond" that evaluated adjoint sensitivities using multiple response functions for different aspects of the storm, not intending to measure the same characteristic, to understand limitations to predictability on high-impact cyclones. Results showed regions of overlap and juxtaposition of sensitivities across response functions, highlighting the importance of carefully defining the forecast aspect of interest for adjoint model sensitivity as the subsequent diagnosis and interpretation of sensitivities is dependent on that selection.

This paper discusses the application of adjoint sensitivity analysis applied to TC intensity, introducing a novel response function designed to measure solely the strength of the TC winds. Section 2 describes the adjoint model and its applications, section 3 describes the response functions used and section 4 is a case study of Hurricane Irma (2017) to compare the influence of response function definition on physical properties and the tangent linear assumption.

4.2 Technical Approach

4.2.1 Adjoint models

An adjoint model is defined as the transpose of the tangent linear model (TLM) approximation to the nonlinear NWP model (NLM), linearized about the forecast trajectory of the NLM. Adjoint models evaluate the gradient of a specific forecast aspect (known as a *response function*, R) with respect to the model state ($\mathbf{x}$) at earlier times by evolving the gradient $\partial R/\partial \mathbf{x}$ (or $\widehat{\mathbf{x}}$) "backward" in time along the NLM trajectory. The response function is a measurable characteristic of the forecast that must be differentiable with respect to the model state (Errico, 1997), but is otherwise at the discretion of the user. The adjoint is initialized by the gradient of the response function with respect to the model final-time forecast state. For this study, response functions chosen to measure different TC intensity metrics are considered. The adjoint evolves the sensitivity gradient "backward" along the trajectory of the NLM to compute the sensitivity of R to prior times in the model forecast.

From a single integration, the adjoint model most efficiently evaluates the sensitivity of a chosen response function to all input parameters (Errico, 1997). Furthermore, the adjoint technique yields precise information on the structure of perturbations that can be made to the initial state to change the response function, which as described earlier is defined at the final state. The impact of any arbitrary perturbation ($\mathbf{x_0}'$) initial condition on the response function can be evaluated by taking the inner product of the sensitivity gradient

with the perturbation:

$$\Delta R \cong \delta R = \left\langle \frac{\partial R}{\partial \mathbf{x_0}}, \mathbf{x_0}' \right\rangle \tag{4.1}$$

where ΔR represents the difference of R from a perturbed nonlinear forecast state and R from the control nonlinear forecast state. Linearity is perfectly held when $\Delta R = \delta R$, meaning the perturbations to the initial state ($\mathbf{x_0}'$) evolved exactly as prescribed (δR).

4.2.2 Adjoint limitations

Accuracy and utility of adjoint models are constrained by the assumption of the tangent linear evolution of perturbations and simplified physics for nonlinear processes, such as moist convection. These assumptions restrict the quantitative accuracy of the adjoint-derived sensitivity gradients for highly nonlinear phenomena, like TCs, to around 18-36 hours. Using sophisticated adjoint models are beneficial for extending the forecast lead time over which sensitivities are quantitatively useful in TCs. The approximation $\Delta R \cong \delta R$ is due to non-linearities that evolve in the NLM (e.g., convection, shifting track of the storm). As long as difference in this approximation is small, the underlying assumptions of the adjoint are held. The behavior of perturbation evolution can also be computed using the TLM, by comparing how the TLM and the difference of the control and perturbed NLM simulations evolve. Qualitative and quantitative comparisons of the perturbations from the TLM and NLM can give insights for what is causing linearity to be lost. This can be done by comparing quantitatively the expected change (δR) from the TLM with the actual change (ΔR) in the nonlinear model. This relationship is an approximation for the correlation between the TLM and NLM perturbations. Further qualitative analysis can be

performed by comparing changes in the model state to investigate reasons for differences between the TLM and NLM perturbations; for example, if speed of propagation is faster in the TLM than the NLM, the linearity would be low even if the magnitude and distribution of the perturbed states are consistent.

4.2.3 Adjoint Sensitivity Analysis

An adjoint model simulation produces the sensitivity of a response function to the model state variables (i.e. temperature, pressure, winds, moisture). In addition to sensitivity to model state variables, derived sensitivities to vorticity and divergence ($\widehat{\zeta}$and $\widehat{\delta}$ respectively; Kleist and Morgan 2005) can also be computed, as they are potentially more insightful to consider since they can be directly related to synoptic features (e.g., vorticity and divergence extrema associated with mid-latitude upper-tropospheric weather systems, tropical Kelvin waves, or changes in the outflow layer inertial stability - where vorticity in the outflow layer is a surrogate for inertial stability). These sensitivities are directly calculable from the sensitivities to the horizontal wind components ($\widehat{u}$ and $\widehat{v}$):

$$\nabla^2\widehat{\zeta} \;=\; -\left(\frac{\partial\widehat{v}}{\partial x} \;-\; \frac{\partial\widehat{u}}{\partial y}\right) \text{ and } \nabla^2\widehat{\delta} \;=\; -\left(\frac{\partial\widehat{u}}{\partial x} \;+\; \frac{\partial\widehat{v}}{\partial y}\right)$$

However, coincidence of synoptic scale features with sensitivities is insufficient to ascribe dynamical significance to that feature (Langland et al., 1995). Perturbations must be constructed based on adjoint sensitivities to elucidate the physical significance.

Numerical simulations of the TCs can be perturbed using adjoint-informed optimal perturbations (e.g., Doyle et al. 2012; Hoover 2015). Adjoint-derived sensitivity gradients, $\partial R/\partial \mathbf{x}$, can be used to objectively calculate the optimal perturbations to the initial conditions of the model to find the desired forecast impact. These perturbations are optimal in the sense that they require the smallest amplitude change in energy, as defined by an energy-based norm:

$$e \;=\; \tfrac{1}{2}\left\langle \mathbf{x'_0},\, \mathbf{W}\mathbf{x'_0} \right\rangle \;=\; \tfrac{1}{2}\left[u'^2 \;+\; v'^2 \;+\; \frac{c_p}{T_0}T'^2 \;+ RT_0\left(\frac{p'_s}{p_0}\right)^2 \;+\; \varepsilon\frac{L^2}{c_pT_0}q'^2 \right] \tag{4.2}$$

where the weighting matrix, $\mathbf{W}$ **,** determines the initial time amplitude or norm. The above energy-based norm equation represents the combined kinetic energy, perturbation available potential energy, perturbation elastic energy, and perturbation latent (heat). Constraining this equation results in the optimal change in the initial state wind, temperature, pressure, and/or moisture, based on your choice of response function R and by the ΔR desired using a Lagrange multipliers technique. The Lagrange multiplier used to constrain the problem is defined as:

$$L = \; e - \lambda\left(\delta R - \langle \frac{\partial R}{\partial \mathbf{x}_0}, \mathbf{x}_0^{'} \rangle\right) \tag{4.3}$$

Through differentiation of L with respect to λ and $\mathbf{x_0'}$ the initial conditions are thus defined as:

$$x_0^{'opt} = \lambda \mathbf{W}^{-1}\frac{\partial R}{\partial x_0} = \delta R \frac{\mathbf{W}^{-1}\frac{\partial R}{\partial x_0}}{\langle \frac{\partial R}{\partial x_0}, \mathbf{W}^{-1}\frac{\partial R}{\partial x_0}\rangle} \tag{4.4}$$

From this expression, for constant $\mathbf{W}$, it is evident that the initial perturbation is directly proportional to the initial time adjoint-derived sensitivity gradient.

$$\delta R = \langle \frac{\partial R}{\partial \mathbf{x}_\tau}, \mathbf{x}_\tau{}' \rangle \tag{4.5}$$

If linearity is held, this dot product should equal the prescribed change in response function used to initialize the adjoint model, ΔR. Any deviations are due to the limitations discussed previously.

4.3 Response Function

For this study, a comparison is made of three response functions, defined over the same horizontal domain consisting of grid points within $\sim$ 180 km of the storm center and, when applicable, the same vertical depth (model levels 6 to 10). This domain allows for a more representative measure of cyclone intensity, rather than the intensity measured at a single point, since sensitivity of TC intensity defined at a single point is strongly controlled by small changes in TC track (Hoover and Morgan, 2010). Using multiple response functions allows for cross-evaluation of sensitivities and differing initial condition perturbations that drive development. The three response functions evaluated are minus the perturbed mass of column dry air ($-\mu$), kinetic energy (KE), and the *vortex-associated kinetic energy* (VAKE). The response function VAKE is a novel adjoint response function that builds from a technique first described by Hoover and Morgan (2011) for instantaneous TC steering by the environmental flow.

The response functions are defined as follows:

1. (Minus) the average *surface pressure* of dry air: the response function (R_μ) is a model state variable that is a proxy for sea level pressure:

$$R_\mu = \frac{1}{N} \sum_{i,j \in D} -\mu_{ij} \tag{4.6}$$

where μ is the dry air in a model column extending from the surface to the top of the model. These values are summed over N grid points in a horizontal domain D indexed zonally by i, and meridionally by j over a defined region centered on the minimum sea level pressure. An increase in R_μ through perturbing the initial conditions would correspond to lower pressure on average in that domain (D). The negative sign is included to such that the sign sensitivities is consistent with other response functions, such that a positive perturbation to a positive sensitivity would result in increasing R_μ.

2. The kinetic energy response function is similar to response functions used in previous studies (e.g., Doyle et al. 2012) which measures the KE of the horizontal winds in the domain centered on the storm:

$$R_{KE} = \frac{1}{N} \sum_{i,j,k \in D} \frac{1}{2}(u_{ijk}^2 + v_{ijk}^2) \tag{4.7}$$

This value is summed over N grid points in a horizontal domain D indexed zonally by i and meridionally by j over a defined box centered on the maximum 850 hPa vorticity.

An increase in R_{KE} through perturbing the initial conditions would correspond to more intense winds on average in that domain.

3. The *vortex-associated kinetic energy* (VAKE) response function (R_{VAKE}) measures the KE associated with the vorticity of the cyclone defined as:

$$R_{VAKE} = \frac{1}{N} \sum_{i,j,k \in D} \frac{1}{2} (u^2_{\zeta_{TC}ijk} + v^2_{\zeta_{TC}ijk}) \tag{4.8}$$

where ζ_{TC} is the vertical component of vorticity associated with the TC. The response function R_{VAKE} is the sum of a subset of the KE associated with only the vorticity that exists within the 3-dimensional lower-tropospheric volume centered on the TC. The calculation of R_{VAKE} requires computing the relative vorticity from the model forecast state zonal and meridional wind, separating the vorticity into the environmental and the TC-associated relative vorticity, inverting the TC-associated relative vorticity to recover the zonal and meridional winds associated with the TC, and calculating the KE of the resulting wind field (Fig 4.1a). Each of these process steps is linear, thus the adjoint model can be initialized by performing the adjoint of each step in reverse-order to recover sensitivities to model state variables. Through this calculation, one can attribute sensitivities (and perturbations to the initial state based on the sensitivities) to changes in the KE of the horizontal wind field associated with the cyclonic vorticity only of the TC (Fig 4.1b). It is hypothesized R_{VAKE} will perform more optimally by focusing on intensification of the TC because it follows the superposition principle, where the greatest overlap (correlation) in perturbation vertical vorticity (ζ') and stream function (ψ') leads

to the largest KE as noted by the equation: $KE = -\frac{1}{2}\int_A \psi'\zeta' dA$. It is expected that the perturbations will evolve to contract about the center of the TC, resulting in higher linearity due to less of a horizontal shift in the position of the TC, which is a major source of non-linearity.

Response function R_{VAKE} was developed to address a potential issue with R_{KE} as demonstrated in Fig 4.2. Fig 4.2a shows the distribution of mean SLP (black contour) and (positive) vorticity (pink fill) associated with a hypothetical control cyclone within a response function box (red). The KE can be increased by decreasing the central pressure and increasing the geopotential height gradient within the box, resulting in stronger winds (Fig 4.2b). This corresponds to a stronger cyclone. The KE can also be increased by enhancing a nearby ridge (blue, negative vorticity) while keeping the vorticity of the TC the same, increasing the geopotential height gradient within the volume and increasing KE, but not developing the storm (Fig 4.2c). Depending on the purpose of the study (i.e., predicting wind damage) R_{KE} alone is a suitable response function, however, if your goal is to understand the intensification of the TC, R_{KE} can lead to unrelated results.

4.4 Case Study: Hurricane Irma (2017)

To compare the performance of adjoint TC intensity metrics, a simulation of Hurricane Irma (2017) was performed using Weather Research and Forecasting (WRF; v3.8.1) forward model (Skamarock and Coauthors, 2008) and its adjoint (Zhang et al., 2013). The adjoint model was initialized three times, using the gradient of each respective response

function: R_{KE} , R_{VAKE}, and R_{μ}. The following are results from the control case study and each response function experiment.

4.4.1 Synoptic History

Hurricane Irma (2017) originated as a convectively active tropical wave, which moved off the west coast of Africa on 27 August and quickly developed into a tropical storm (Cangialosi et al., 2018). Two days after genesis, following a period of rapid intensification (RI), Irma (2017) grew into a major hurricane at 0000 UTC 1 September in an environment of favorably low wind shear and a fairly moist lower troposphere with marginally favorable sea surface temperatures (SSTs). Subsequently, Irma's intensification fluctuated between a category 2 and 3 until 0000 UTC 4 September due to dry air intrusions and eyewall replacement cycles (Cangialosi et al., 2018). At the same time Irma interacted with a strong anticyclone to its north that shifted its track west-southwest over warmer SSTs and brought it in line to interact with the northern Leeward Islands. Early 4 September, Irma began to intensify again, growing in size and symmetry. The western side of the mid-level ridge eroded and Irma turned west-northwest, and began another round of RI. Irma reached a category 5, maximum intensity of 155 kt around 1800 UTC 5 September, when it was located 70 n mi east-southeast of Barbuda. Later Hurricane Irma made landfall on Barbuda around 0545 UTC 6 September still with 155 kt winds and a minimum pressure of 914 hPa. Irma continued at a category 5 strength at its second landfall in St. Martin later that day at 1115 UTC, and again in the British Virgin Islands

at 1630 UTC. As Irma moved away from the Virgin Islands, while still a category 5 hurricane, it weakened slightly and had a broader wind field than earlier. Irma maintained a category 5 strength for 60h as it moved nearby a number of islands.

4.4.2 Case Overview

This case study focuses on a 24-hour period associated with the second RI period, initialized at 0000 UTC 5 September, using the WRF. The WRF adjoint, available through WRFPLUSv3.8.1, has the adjoint of most moist physical processes for large scale condensation and the adjoint of a simplified cumulus scheme (Xiao et al. 2008; Chu et al. 2011). The WRF was initialized using the National Center for Environmental Predictions (NCEP) FNL (Final) operational global analysis on 0.25° x 0.25° latitude longitude grid available from the National Center for Atmospheric Research (NCAR) Research Data Archive (RDA) as dataset ds083.3. The numerical simulation was run at 18 km horizontal grid spacing. This grid spacing is consistent with the few other adjoint-based tropical cyclone studies (e.g., Doyle et al. 2011; Doyle et al. 2012; Hoover 2015; Reynolds et al. 2016). The model was configured with 65 layers of evenly spaced vertical levels, from the surface to 50 hPa.

The storm does not reach the same intensity or intensification rate as observed; however, the simulation has a well spun-up vortex centered within 85 km of the observed system. While the initial vortex is weaker than operational models, the intensification rate is consistent with the experimental the Navy Research Laboratory COAMPS-TC model (CTCX) and the operational Hurricane WRF (HWRF) model. These model forecasts are

run at finer grid spacing, nested 45-, 15-, 5-km, and nested 18-, 6-, and 2-km, respectively. Tracing the track and intensity (not shown), the track forecast is slower, but similar to the best track. After 24 hours, the simulation has developed a hurricane with a central pressure of 959 hPa and maximum surface wind of 80 kt. The simulation is not expected to represent Hurricane Irma (2017), rather to simulate an environment capable of producing an intensifying TC. In this context, the simulation does contain a robust TC that is physically consistent with its environment.

At the beginning of the model simulation, Hurricane Irma is located at 16.2 N, 55.1 W being steered west-northwest by an eroding mid-level ridge. In favorably warm SSTs (Fig 4.3a) and based on track expected to traverse into higher SSTs. The TC environment is moist, with high relative humidity though dry air is to the west of the cyclone (Fig 4.3b). Irma's near environment is characteristic of favorable shear (Fig 4.3c). A high shear environment is to the north-northeast associated with a weak jet and trough, coinciding with filament of potential vorticity (PV) (Fig 4.3d). This jet is also likely associated with a developing outflow jet associated with the cyclone. In the near environment and outside its core, the outflow level PV is generally low and the flow is broadly divergent (Fig 4.3d). All these characteristics are favorable for intensification to occur. The outflow in this case study is identified by the equivalent potential temperature (θ_e) that enters at the base of the eyewall. In the control simulation this value is ranges from 354 to 358 K, which in the upper troposphere is situated slightly below or at 150 hPa, rising as the simulation progresses and the TC intensifies.

As the simulation progresses, the outflow becomes more pronounced as shown by the negative PV and the anticyclonic wind field (Fig 4.4). A pool of high equivalent potential temperature at 900 hPa increases in the core of the storm, which broadens as the simulation advances (Fig 4.4). Low equivalent potential temperature persists to the northeast, associated with an anticyclone. Furthermore, bands of low (less than 345 K) equivalent potential temperature are to the south and west of the TC, but are not advected into the core. The anticyclone located to the north-northeast of Irma continues to steer the TC north-northwest. Notably, the sea level pressure becomes more asymmetric at forecast hour 24, as it borders the anticyclone to the east. The interaction of the TC vortex with an anticyclone provides an adequate set up to compare the KE and VAKE response functions.

Based on the simulated forecast at forecast hour 24, the response functions R_{KE}, R_{VAKE}, and R_{μ} were calculated. The gradients of each response function are used to initialize the adjoint model to produce sensitivities to the model initial state. The extent of the horizontal response function domain is shown in the red box for all adjoint integrations (Fig 4.4). This horizontal box is centered about the latitude longitude location of the maximum vorticity of the 0.90625 eta level, which approximately corresponds to the 900 hPa level assuming the surface pressure is 1000 hPa.

4.4.3 Sensitivities

The 200 hPa sensitivity to potential temperature ($\widehat{\theta}$) for R_{KE}, R_{VAKE}, and R_{μ} share similar distributions, banded positive and negative structures in the near environment with

the strongest sensitivities to the south of the core, however, they have slight differences in magnitude and distribution (Fig 4.5). A notable difference in distribution is to the east of the core, with R_{KE} suggesting a greater sensitivity to warming than R_{VAKE} or R_{μ}. The consistencies are overall greater between R_{KE} and R_{VAKE}, as expected since the response function definitions are more closely related than R_{μ}. Additionally, R_{μ} is more similar to R_{VAKE} than R_{KE}. This is likely due to the relationship between surface pressure (e.g., R_{μ}) and vorticity, which R_{VAKE} is derived from. The magnitude of the sensitivities is scaled by their respective maximum values on that level, as the sensitivities do not have the same units due to their response functions.

Features farther from the feature of interest suggest an adjustment or gravity wave disturbance that is unbalanced and not linked to physical features, rather boundary conditions. This is most apparent at times close to when the response function is defined, as shown in Fig 4.6. Fig 4.6 shows the same plotted variables as Fig 4.5 except over the full domain 21 hours into the forecast (3 hours from when the response function is defined). As evident in the sensitivity patterns, an adjustment process is present with large, non-physical features (e.g., banding). The magnitude of the non-physical adjustment to in near environment is larger for R_{KE} and R_{μ}, with R_{VAKE} showing less of an adjustment. This is most apparent when analyzing the sensitivities to surface pressure ($\widehat{\mu}$) at forecast hour 21 (Fig 4.7). Three hours prior to the response function being defined to intensify the TC, it is expected that the dominant feature in the surface pressure sensitivity is to decrease the pressure near and within the cyclone core (as indicated by a strong negative $\widehat{\mu}$). Notably, the R_{KE} and R_{μ} sensitivities show high frequency waves at the boundaries that is the

dominant feature with similar to larger magnitudes than the expected sensitivity in the core. This is also present, but less pronounced using R_{VAKE}, where the main feature is the expected negative $\widehat{\mu}$. As the adjoint integration integrates further "backward" in time, evidence of the high frequency waves across each adjoint integration diminishes, occurring the quickest in R_{VAKE}, followed by R_{KE} and lastly R_{μ}, (Fig 4.8 and Fig 4.9). The high frequency wave pattern shown is an established feature in adjoint sensitivity studies, particularly using surface pressure response functions (Errico and Vukicevic 1992; Morgan 2018) and is a signature of the adjustment process resulting in gravity wave like structures. These results suggest that VAKE is a more balanced response function that results in fewer spurious adjustments. This is due to how VAKE is calculated, as it filters out the divergent component of the flow, which can result in nonlinear features when perturbing the nonlinear model based on adjoint sensitivities.

The 850 hPa sensitivity to vorticity, across response functions, is in agreement to increase the relative vorticity in the core of the TC with a coupled counterclockwise spiral of positive and lower (or negative) vorticity extending into the near environment of the TC (Fig 4.10). However, outside the core the patterns are nearly reversed between R_{KE} and R_{VAKE}, with R_{μ} an entirely different pattern (Fig 4.11). Analyzing the R_{KE} experiment, sensitivities to vorticity imply increasing the steering flow to increase the westward movement will increase the KE at forecast hour 24. The R_{VAKE} sensitivities imply reducing the steering flow, slowing the westward movement, will increase VAKE at forecast hour 24. The R_{μ} experiment sensitivities overall suggest adding more positive vorticity, stretching from the storm core to the northeastern half of the domain while reducing the

vorticity to the south and east. Both R_μ and R_{VAKE} suggest weakening the low-level anticyclone in the mid-Atlantic ocean. The three response functions show contrasting sensitivity patterns particularly in the lower troposphere. Differences reduce in the middle and upper (outflow) levels (Fig 4.12). The increase in similarity is most apparent between R_{KE} and R_{VAKE}, as expected. The vertical change in the differences across response functions indicate (in this case study) that the upper levels are less sensitive to the definition of TC intensity.

Vertical distribution of sensitivities show consistency across all response functions, with the largest sensitivities in the lower troposphere, particularly below 900 hPa, in the boundary layer (Fig 4.13). Notably, the vertical distribution of sensitivity to zonal and meridional winds using R_μ has a less dramatic change in the distribution in the lower troposphere. In addition to the sensitivity value's global maximum in the boundary layer, a local maxima is in the middle troposphere, between 500 and 700 hPa and in the upper troposphere, and between 200 and 300 hPa at the bottom of the outflow level, as defined by the equivalent potential temperature which enters the eyewall.

While the coincidence of sensitivities with the basic state are desirable to attribute to a feature (such as deepening the passing trough), perturbations must be made and evolved to attribute meaning of the sensitivities. Calculating and evolving optimal perturbations enables the ability to determine whether tangent linear assumptions are held. Evaluating this can elicit more information on adjoint response functions.

4.4.4 Optimal Perturbations

Optimal initial condition perturbations to the zonal and meridional wind components were calculated as described in section 4.2.3. The prescribed change (δR) was a 5% increase in VAKE. The response function domain and prescribed change are identical for both KE and VAKE sensitivity experiments in order to compare results. The (dry surface) pressure response function is prescribed as an average 25 Pa increase in response function area. The 25 Pa prescribed change is used as it results in a similar initial change in total perturbed KE in the model domain across all three response function experiments. Across all three perturbed simulations, perturbations to the initial winds are all weaker than 3 ms^{-1} with the majority under 0.5 ms^{-1}.

As anticipated, at initialization time all perturbations are associated with perturbing the zonal and meridional wind components. Perturbations are concentrated below 900 hPa, with a local maxima at 500 and 200 hPa (Fig 4.14), consistent with the sensitivities (Fig 4.13). The initial distribution of perturbation KE are in agreement, with R_{KE} having a greater dependence on near surface perturbations than R_{μ} and R_{VAKE}. The spread in the distribution of energy is greatest at the initial time and decreases as the integration steps forward. As the perturbations evolve, the fraction of the change in KE shifts upwards. The final time (forecast hour 24) perturbation KE has two maxima, the primary maximum is concentrated about the outflow layer (200 hPa) and a smaller local maxima around 900 hPa. The low-level maximum is located vertically where the response function is defined for R_{KE} and R_{VAKE}. This distribution is consistent across all response

functions. This result is consistent with results found in Doyle et al. (2012) that show a "bottom-up" development, where initial condition sensitivities are maximized in the lowest 2 km and, when perturbed, undergo rapid growth in a deep layer throughout the troposphere. The change in latent heat energy is maximized in the lower troposphere, peaking at or slightly below 900 hPa. After initialization time, the available potential energy has a smaller, local maximum near 900 hPa as well as a global increase in the upper troposphere lower stratosphere (above 300 hPa to top of model domain, 50 hPa).

The normalized storm (difference divided by control value) relative averaged difference of SHIPS-related variables are shown in Fig 4.15. The variables are scaled, as described in the figure, to account for the relative change. The the average change across the three experiments is nearly identical in sign and magnitude until forecast hour 12, with the exception of a larger decrease in the 200 hPa in the R_{VAKE} simulation (Fig 4.15b) with a smaller decrease in R_{KE} simulation (Fig 4.15a) and R_{μ} simulation (Fig 4.15c). After forecast hour 12, the average change in SHIPS-related variables begins to increase and differences across simulations increases. At the final time, forecast hour 24, the average change in 850 hPa vorticity is largest for R_{μ} followed by R_{VAKE} and then R_{KE}, as shown in Fig 4.15. The average 200 hPa temperature change at forecast hour 24 is negative for R_{VAKE}, while positive for R_{μ} and R_{KE} (Fig 4.15). The RH steadily increases from forecast hour 18 in the R_{VAKE} and R_{KE} simulations, the R_{μ} simulation begins to increase at forecast hour 21 resulting in the RH being lower for the R_{μ}. From forecast hour 21 to forecast hour 24 the PW in all three simulations decreases, with the R_{VAKE} simulation average change having a negative change in PW.

Analyzing the horizontal distribution of select SHIPS-related metrics, initial perturbations to 850 hPa vorticity based on R_{KE} are concentrated near the TC and on average increase the relative vorticity within 1000 km of the TC center. The initial perturbations are in a banded structure, suggesting wind speed maximum acting on shear that possibly links to barotropic growth, through extracting energy from the mean state KE and converting it into the TC KE (Nolan and Farrell, 1999). As the perturbations evolve, they remain somewhat banded and concentrated along regions of local maxima of vorticity. At the final time, the largest perturbations are near the cyclone center and mostly attributable to a shift to the southwest and rotation of the cyclone. The average vorticity has increased at this time at 850 hPa within 1000 km of the TC, indicating a more intense TC. Using R_{VAKE}, a very similar distribution is shown compared to R_{KE} at early model time steps, at the final time, a notable difference is $\sim 90°$ rotation counterclockwise relative to R_{KE} resulting in a mostly westward shift or broadening. The response function R_{μ} again has similar banding at the initial time, although the magnitude of the perturbations are slightly larger. This is consistent with the vertical distribution of perturbations (Fig 4.14), as at initialization time the R_{μ} experiment has a smaller perturbed KE at level 850 hPa compared to R_{VAKE} and R_{KE}. At the final time, the change in vorticity shifted to the west of the cyclone center as well as a spiral inward of the vorticity.

The 200 hPa temperature within 1000 km of the TC center at forecast hour 12 shows asymmetric distribution with a dominant warming to the northwest for all three simulations and slight cooling to the east of the TC (Fig 4.19). All, on average, increase the 200 hPa temperature, though only slightly. These results run counter to the assumption

that through decreasing the outflow level temperatures the maximum potential intensity increases, which creates an environment for the TC to intensify more efficiently. However, the asymmetric distribution of perturbed 200 hPa temperature may be consistent with Nolan et al. (2007) which demonstrated that heat release in highly asymmetric convective bands may be transferred into KE of the quasi-symmetric wind field and the available potential energy associated with the warm core. The change in 200 hPa temperature for R_{VAKE} broadly decreases around the core, with a maximum to the northwest (Fig 4.19). This maximum decrease is evident across all response functions, with R_{μ} having a strong band to the north. To the south of the TC the perturbed temperature is largely positive for all three response functions, with most warming occurring with R_{μ}.

The largest surface latent heat (LH) flux increase within the response function domain (approximately 180 km from the TC center) at the final time was observed for optimal perturbations derived from R_{VAKE} sensitivities, followed by R_{KE} and R_{μ} (Table 4.1). All perturbed simulations result in a nearly continuous increase in LH flux around the core, with a decrease associated with a shift in the storm core (Fig 4.20). The distribution of the change in LH flux is broadly consistent with the shift of the TC center for each respective simulation. Coincident with the change in the latent heat flux is the change in upward moisture flux (Fig 4.21). This is consistent with the stronger low-level winds enhancing surface evaporation and LH flux, which adds latent energy to the atmosphere due to condensation that can result in a more intense TC.

Cross evaluation of the metrics used to define each response function can elucidate the

relationship between changes in KE, VAKE, and μ (Fig 4.22). In the simulation from R_{KE} sensitivities, there is a shift to the southwest with an increase in the KE around the TC core (Fig 4.22a). To the northeast the KE decreases indicating the gradient of KE has increased. The minimal increase in KE and attribution of a shift rather than development can be noted through analyzing the average change in Table 4.1. Furthermore, looking at the change in the horizontal distribution of μ (Fig 4.22g), there is little change associated with the perturbed field that is not attributable to the shift.

In the simulation from R_{VAKE} sensitivities, a slight shift of the storm occurs to the west accompanied by a deepening and broadening of the TC (Fig 4.22e). While a large component of the in μ shows the shift in position (Fig 4.22h), the decrease in the perturbation dry air pressure in the column is larger and broader than the increase (Table 4.1). Furthermore, the increase of the KE (Fig 4.22b) and VAKE (Fig 4.22e) does not emphasize a change to northeast of the TC core like using R_{KE}, which supports the use of R_{VAKE} as a response function for TC intensity over R_{KE}.

From the R_{μ} sensitivity perturbation simulation, results are similar to the distribution of change using R_{VAKE} with small shift slightly more southward shift in TC position (Fig 4.22i). The broadening and deepening is evident qualitatively (Fig 4.22i) and quantitatively (Table 4.1). Contrasting the average change across the response functions used, implementing R_{VAKE} results in the largest average change in KE and VAKE, with the second largest change in μ while R_{μ} creates the largest change in μ and second largest

change in KE and VAKE(Table 4.1). Notably, R_{KE} results in the smallest change across all response functions variables.

To further compare the change in the R_{KE} and R_{VAKE} simulations, using the conceptual model motivating the VAKE response function (Fig 4.2), the difference in the 900 hPa geopotential height is calculated within the response function domain (Fig 4.23). The increase in the geopotential height to the northeast and decrease to the southwest in Fig 4.23a confirm the shift in the R_{KE} simulation location is along the orientation of the anticyclone to the northeast. This contrasts to the shift in the R_{VAKE} and R_{μ} simulations is predominately westward. Additionally, the gradient of the stream function (calculated from the TC vorticity) is taken in the zonal and meridional direction. Within the response function domain, the R_{KE} simulation zonal gradient of stream function ($\delta\psi/\delta x$) shows a slight shift westward shift and an increase in the gradient in the center of the domain (Fig 4.24a). The meridional gradient of stream function ($\delta\psi/\delta y$) shows a tripole (negative, positive, negative) with the largest meridional change overlapping with the zonal maximum. The southwestward shift show in Fig 4.23a along with the tightening of the gradient of stream function, as well as the minimal change in SLP from the R_{KE} simulation support the conceptual model for how the KE can increase without intensifying the TC. Analyzing the R_{VAKE} simulation zonal gradient of stream function shows a westward shift and an increase in the gradient in the center of the domain (Fig 4.24b). The meridional gradient of stream function shows a quadrupole also showing the westward shift, along with a slight southward shift. The R_{μ} simulation shows a near identical change as the R_{VAKE} simulation, only slight muted (Fig 4.24c). This analysis

partially addresses the concern highlighted in the beginning of this chapter about the multiple routes to increase the KE within a confined domain.

Variable	R_{KE}	R_{VAKE}	R_{μ}
KE	5.86	9.4	6.0
VAKE	3.37	10.4	7.0
μ	-0.036	-0.061	-0.094
SLP	-0.038	-0.067	-0.088
HFX	0.46	-0.10	0.19
QFX	1.26e-6	1.33e-6	9.67e-7
LH	3.14	3.32	2.42

TABLE 4.1: Comparison of average change in variables within response function domain (20 grid points north and south centered on the maximum 850 hPa relative vorticity latitude-longitude position), horizontally and vertically (model levels 6 to 10), when applicable. Values are Kinetic energy (KE; m^2s^{-2}), vortex associated KE (VAKE; m^2s^{-2}), perturbation dry air mass in column (μ; Pa), sea level pressure (SLP; Pa), upward heat flux at surface (HFX; Wm^{-2}), upward moisture flux at surface (QFX; $gm^{-2}s^{-1}$), and latent heat flux at surface (LH; Wm^{-2})

4.4.5 Tangent Linear Assumption Validity

To test the validity of the tangent linear adjoint assumption for this case, we calculate the linearity ratio, the ratio of the prescribed change (δR) to difference between the response function for the perturbed and control simulation (ΔR):

$$\Delta R = R_{perturbed} - R_{control} \tag{4.9}$$

The evolution is perfectly (tangent) linear if $\Delta R/\delta R = 1$, as described in section 2.2 with equation 1. Any deviations are associated with the nonlinear evolution of perturbations, and/or physics that exists within the forward model, but not the adjoint model, such as moist convection. For both R_{KE} and R_{VAKE} perturbed simulations, the prescribed change

is δR_{VAKE}=40140 m^{2}s^{-2}. The ΔR, using R_{KE} as the response function, is $\Delta R_{KE} = 9512$ m^{2}s^{-2} resulting in a linearity ratio of 0.24. The evolved KE is shifted to the southwest of the response function domain center, with a slight increase in the average KE in the response function domain (Fig 4.25a). The largest magnitude change is associated with the shift in position, however, there is an increase in the KE. The ΔR, using R_{VAKE} as the response function, is $\Delta R_{VAKE} = 16687$ m^{2}s^{-2} resulting in a linearity ratio of 0.42. Notable differences in the evolved R_{VAKE} is an expansion and slight shift of VAKE to the west of the response function domain center (Fig 4.25b). The ΔR_μ, using R_μ is 9.42 Pa, where the $\delta R_\mu = 25$ Pa, resulting in a linearity ratio of 0.38. Recall that since the response function is defined as $-\mu$, a positive change in δR_μ corresponds to a deepening (i.e. lower surface pressure) of the TC. The change is partially due to a shift if the TC center to the southwest along with a slight deepening (Fig 4.25c). Comparing the linearity ratios across the three response functions, the response function VAKE performed best with respect to the tangent linear assumption.

Comparing the evolved nonlinear perturbations to the tangent linear perturbations evolved at the final time, the overall spatial distributions are well-aligned for the R_{KE} and R_{VAKE} simulations, but nearly reversed for the R_μ simulations (Fig 4.26i). The magnitude of the change is lower for the nonlinear perturbations in all cases. The shifts in TC location indicated in the difference fields are also present in the tangent linear perturbations and therefore, not the main contributor to the loss in linearity. The response function R_μ indicates that part of the loss to linearity is due to faster, counter-clockwise rotation in the nonlinear model relative to the tangent linear model (Fig 4.26c, f, and i). To further

analyze the change in TC intensity across response functions, a comparison of the perturbed stream function (ψ') derived from the distribution of perturbed vorticity (ζ') is completed (Fig 4.27). Comparing the changes across the three simulations, the R_{VAKE} simulation results in a lower stream function, with potentially a small shift in position (Fig 4.27b). The R_{KE} simulation is associated with a shift as well, however, the orientation of the change in stream function aligns such that the increase in stream function of the northeast is collocated with the anticyclone (Fig 4.27a). This supports the hypothesis that a KE response function for intensity change is tied to restructuring the wind field and increasing the gradient of the stream function through building up a ridge instead of deepening the TC within the response function domain. The R_{μ} simulation shows little change not associated with a shift to the west, however, there is a slight deepening to the west (Fig 4.27c).

4.5 Conclusions

The definition of tropical cyclone intensity in an adjoint sensitivity study influences the physical processes and structure that lead to changes in intensity. Moreover, the choice of response function may lead to changes in TC position and broadening. The change of all three response functions in this analysis is generally consistent, while the tangent linear assumption is best held by the response function R_{VAKE}. This is found in other TC cases (not shown). The cause of the tangent linear assumption being held most closely is likely due to the definition of VAKE, as it utilizes the superposition principle, where the largest overlap in perturbation vertical relative vorticity and stream function result

in the greatest change in KE. This is evident as the change in VAKE is largely due to a broadening and shift to the center of the response function domain. The high linearity using R_{VAKE} is also likely due to it's being a more balanced response function, as the high frequency wave patterns is more evident in the R_{KE} and R_{μ} sensitivity fields than R_{VAKE} sensitivity fields. Additionally, the signal of the high frequency waves diminishes quickest in the R_{VAKE} initiated adjoint integration. A sensitivity field which contains less high frequency waves (i.e., more balanced) is hypothesized to result in less loss in the linearity ratio, which is a major limitation in adjoint sensitivity analysis.

The changes in the physical processes across all response function are consistent enough to not denote specific process important for each respective response function. This could be due to the small prescribed and evolved change. However, the differences between the nonlinear and tangent linear perturbations provides insights into the relative effectiveness of VAKE over KE as a response function measuring TC intensity as it minimizes the potential for an increase in KE to be associated with stronger winds without deepening the TC. An important aspect of using VAKE as a response function is the structure contained within its definition and the implicit relationship between VAKE and the superposition principle, where the most efficient method to increase the perturbed KE is through the overlap of perturbed stream function and perturbed vorticity. This relationship results in a higher likelihood of the tangent linear and nonlinear perturbations being co-located, but at different magnitudes. Both traditional response functions, KE and -μ, do not specify structure of how the change in the nonlinear or tangent linear perturbations evolve. This can lead to changes in the response function that do not correspond to the metric intended

to be evaluated as shown using the R_{KE}. Alternatively, as seen using R_{μ}, the orientation of the evolved perturbations in nearly reversed between the tangent linear and nonlinear model simulations.

a

$$u, v \rightarrow \zeta \rightarrow \zeta_{TC} + \zeta_{ENV} \rightarrow u_{TC}, v_{TC} \rightarrow R = \frac{1}{2}(u_{TC}^2 + v_{TC}^2)$$

b

$$\frac{\partial R}{\partial u}, \frac{\partial R}{\partial v} \leftarrow \frac{\partial R}{\partial \zeta} \leftarrow \frac{\partial R}{\partial \zeta_{TC}} \leftarrow \frac{\partial R}{\partial u_{TC}}, \frac{\partial R}{\partial v_{TC}}$$

FIGURE 4.1: a) Flowchart describing how is R_{VAKE} calculated based on u and v wind at final time forecast; b) Flowchart describing how sensitivity to model state u and v wind, $\partial R/\partial u$ and $\partial R/\partial v$, are calculated from $\partial R/\partial u_{TC}$ and $\partial R/\partial v_{TC}$. Note that for R_{VAKE}, environmental vorticity is set to zero outside of response function domain using a local projection operator.

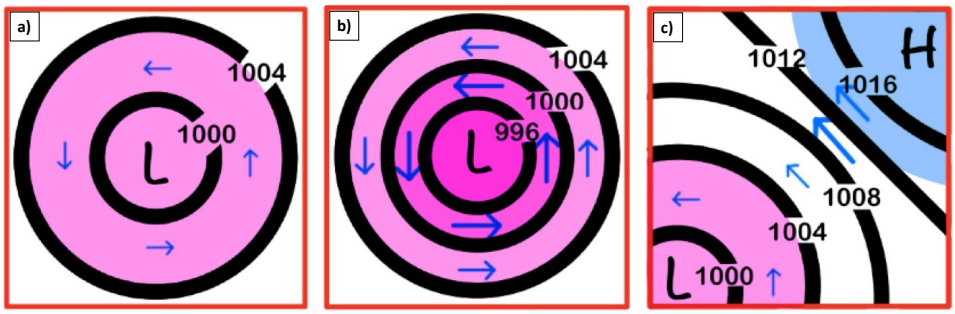

FIGURE 4.2: Fill depicts (geostrophic) vorticity perturbation (pink-positive, blue-negative), and a minimum in local sea level pressure; a) Control cyclone in response function domain; b) perturbed, deeper cyclone with increased KE and no change to the position; c) perturbed, undeepened cyclone with increased KE and change in position.

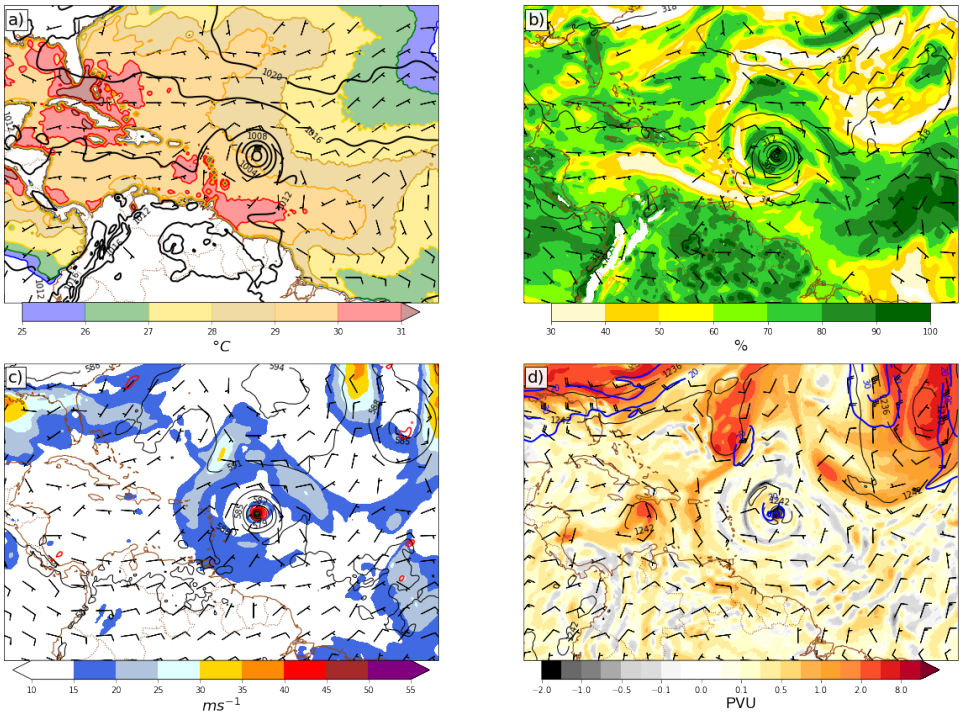

FIGURE 4.3: Valid 0000 UTC 5 September 2017 a) Sea surface temperatures (fill; °C), sea level pressure (black; hPa) and 10 m wind (barbs; ms^{-1}), b) 850-700 hPa average relative humidity (fill; %), 700 hPa geopotential height (black; m), and wind (barbs;ms^{-1}), c) 850–200 hPa vertical wind shear (fill; ms^{-1}), 500 hPa relative vorticity (red; 10^5s^{-1}), geopotential height (black; m), and wind (barbs;ms^{-1}), d) 200 hPa potential vorticity (fill; PVU), wind speed (blue; ms^{-1}), geopotential height (black; m), and wind (barbs;ms^{-1})

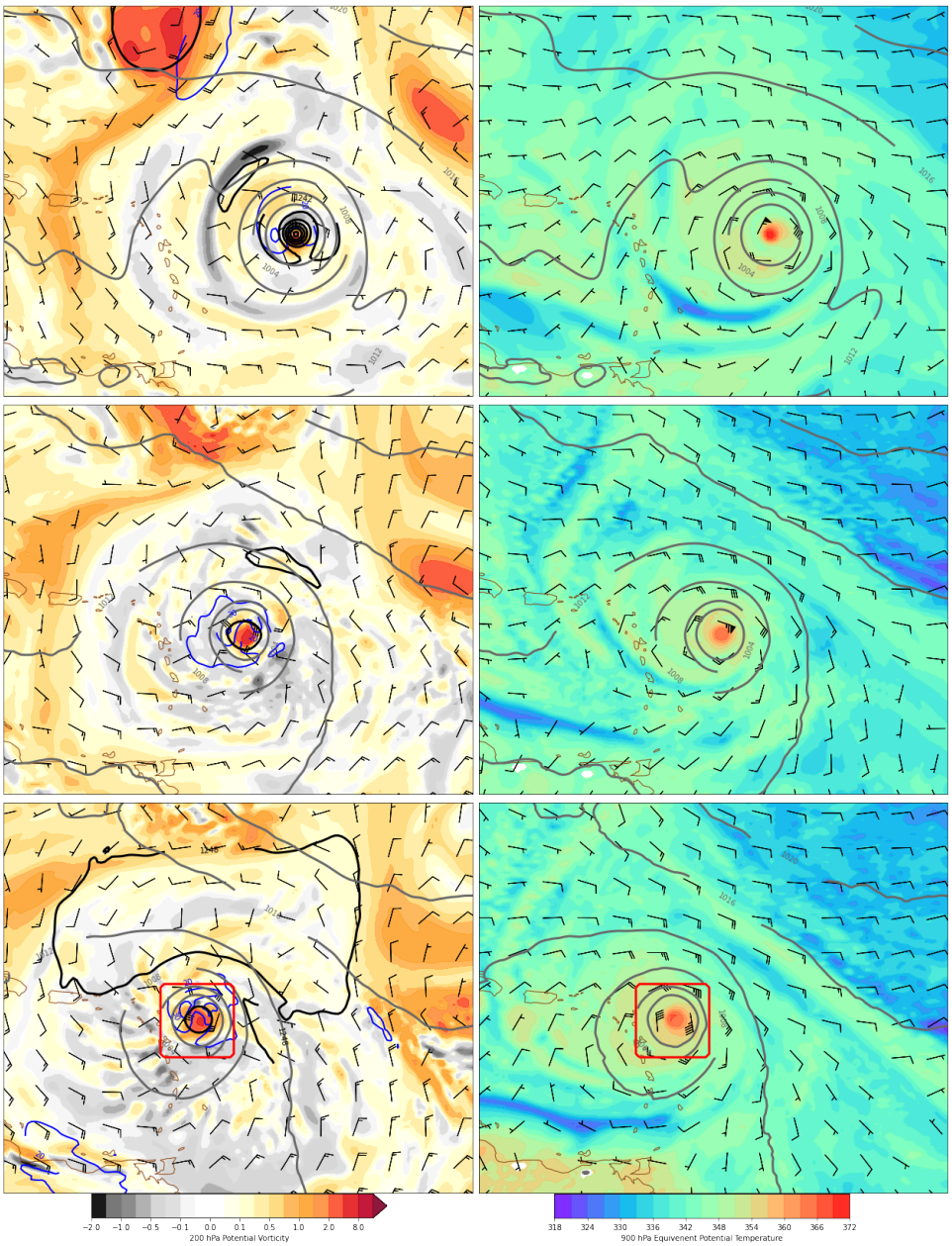

FIGURE 4.4: Right panels 200 hPa potential vorticity (fill; PVU), wind speed (blue; ms^{-1}), geopotential height (black; m), wind (barbs;ms^{-1}), and SLP (grey; hPa). Left panels 900 hPa equivalent potential temperature (fill; K), wind (barbs;ms^{-1}), and SLP (grey; hPa). Valid at a-b) 0000 UTC 5 September, c-d) 1200 UTC 5 September, and e-f) 0000 UTC 6 September. Red box denotes horizontal size and location of response function.

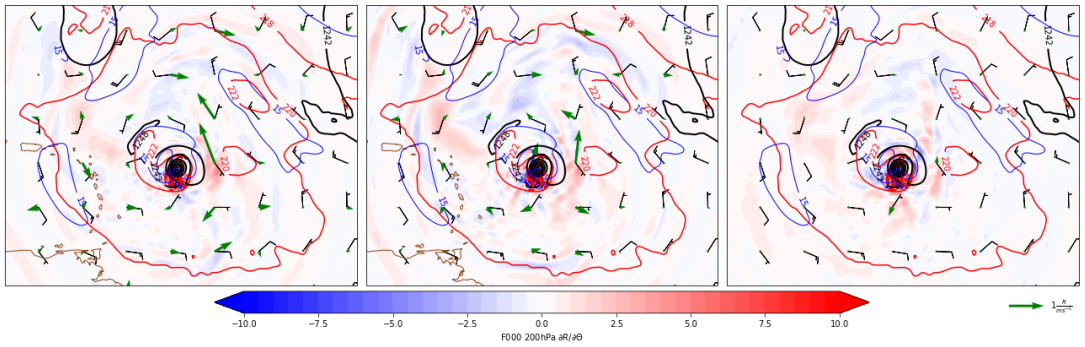

FIGURE 4.5: The 200 hPa adjoint sensitivity to potential temperature for response functions R_{KE} (m^2s^{-2}/K), R_{VAKE} (m^2s^{-2}/K), and R_{μ} (Pa/K), respectively, (color scale by maximum value on that level), sensitivity to horizontal winds (green vectors), 200 hPa potential temperature (solid red every 2 K), wind speed (solid blue every 5 ms^{-1} above 15 ms^{-1}), geopotential height (solid black every of 60 m) and wind (barbs; ms^{-1}) at initial time of valid at 0000 UTC 5 September 2017.

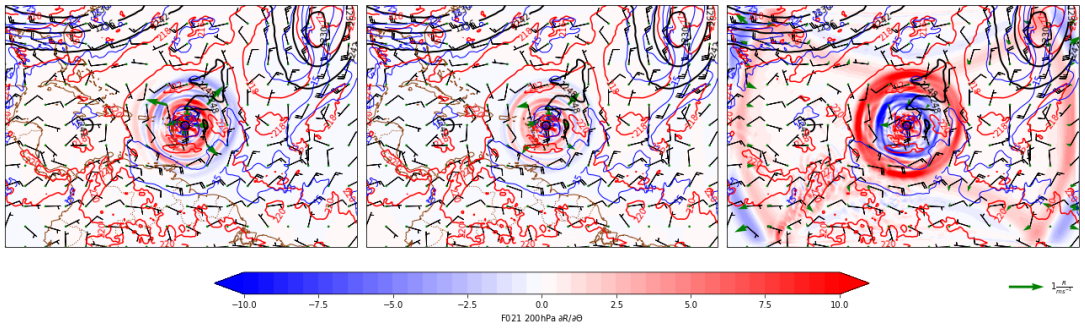

FIGURE 4.6: Same as Figure 4.5 except valid at 2100 UTC 5 September 2017 over entire model domain.

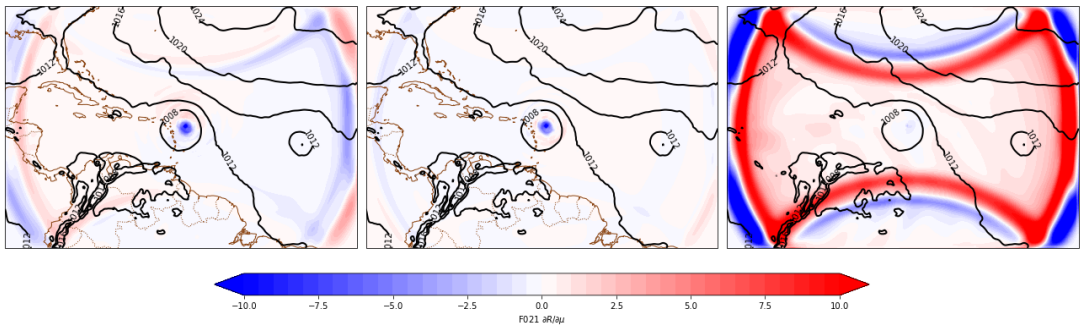

FIGURE 4.7: The adjoint sensitivity to dry air perturbation in a column ($\widehat{\mu}$) for response functions R_{KE} (m^2s^{-2}/Pa), R_{VAKE} (m^2s^{-2}/Pa), and R_{μ} (Pa/Pa), respectively, (color scale by maximum value on that level; R / Pa), and SLP (solid black every of 4 m above 1008 hPa) 2100 UTC 5 September 2017.

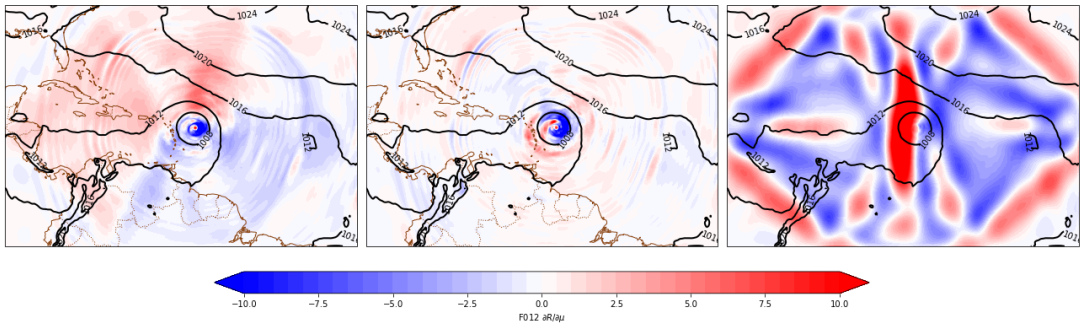

FIGURE 4.8: Same as Figure 4.7 except valid at 1200 UTC 5 September 2017.

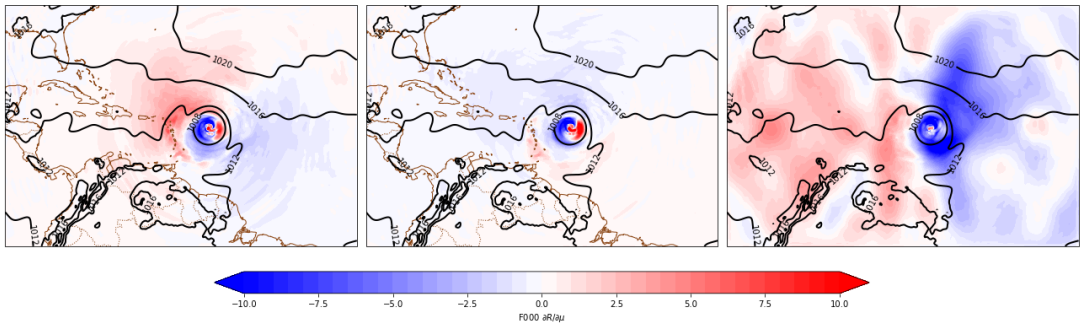

FIGURE 4.9: Same as Figure 4.7 except valid at 0000 UTC 5 September 2017.

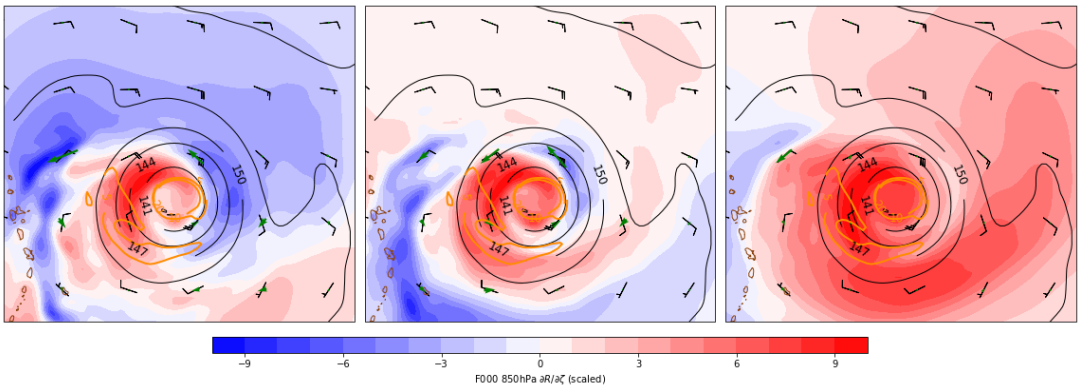

FIGURE 4.10: The 850 hPa adjoint sensitivity to vorticity for response functions R_{KE} (m^2s^{-2}/s^{-1}), R_{VAKE} (m^2s^{-2}/s^{-1}), and R_{μ} (Pa/s^{-1}), respectively, (color scale by maximum value on that level), sensitivity to horizontal winds (vectors), positive relative vorticity (solid orange scale by 1e5 every 5 s^{-1}), geopotential height (solid black every of 60 m) and wind barbs (ms^{-1}) at initial time of valid at 0000 UTC 5 September 2017.

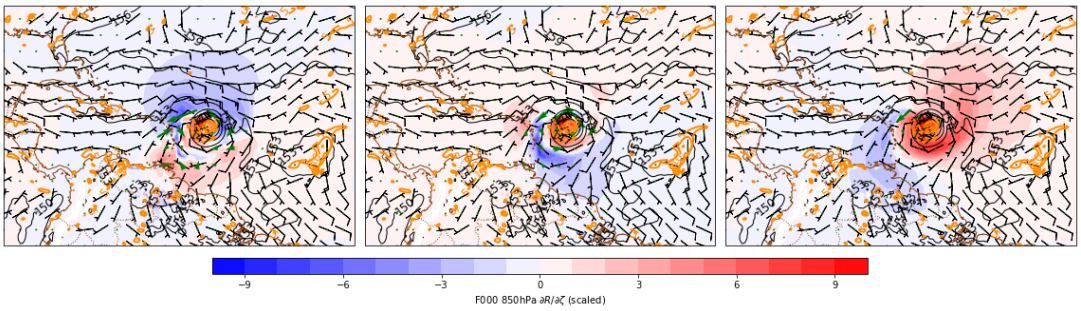

FIGURE 4.11: Same as Fig 4.10 except for full domain.

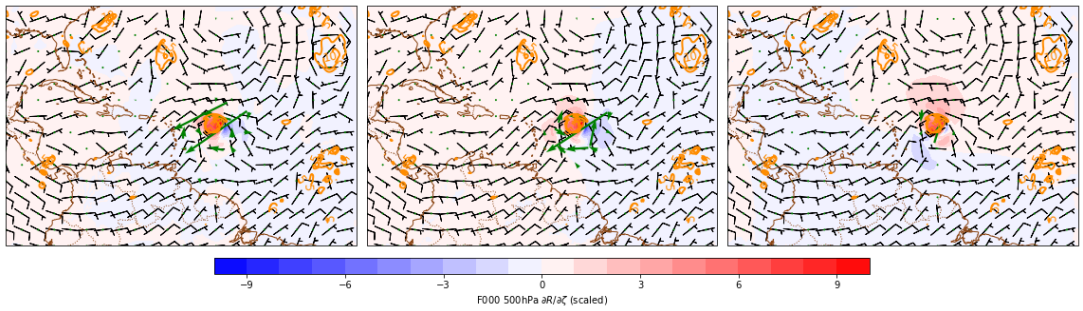

FIGURE 4.12: Same as Fig 4.10 except for 500 hPa level and over full model domain.

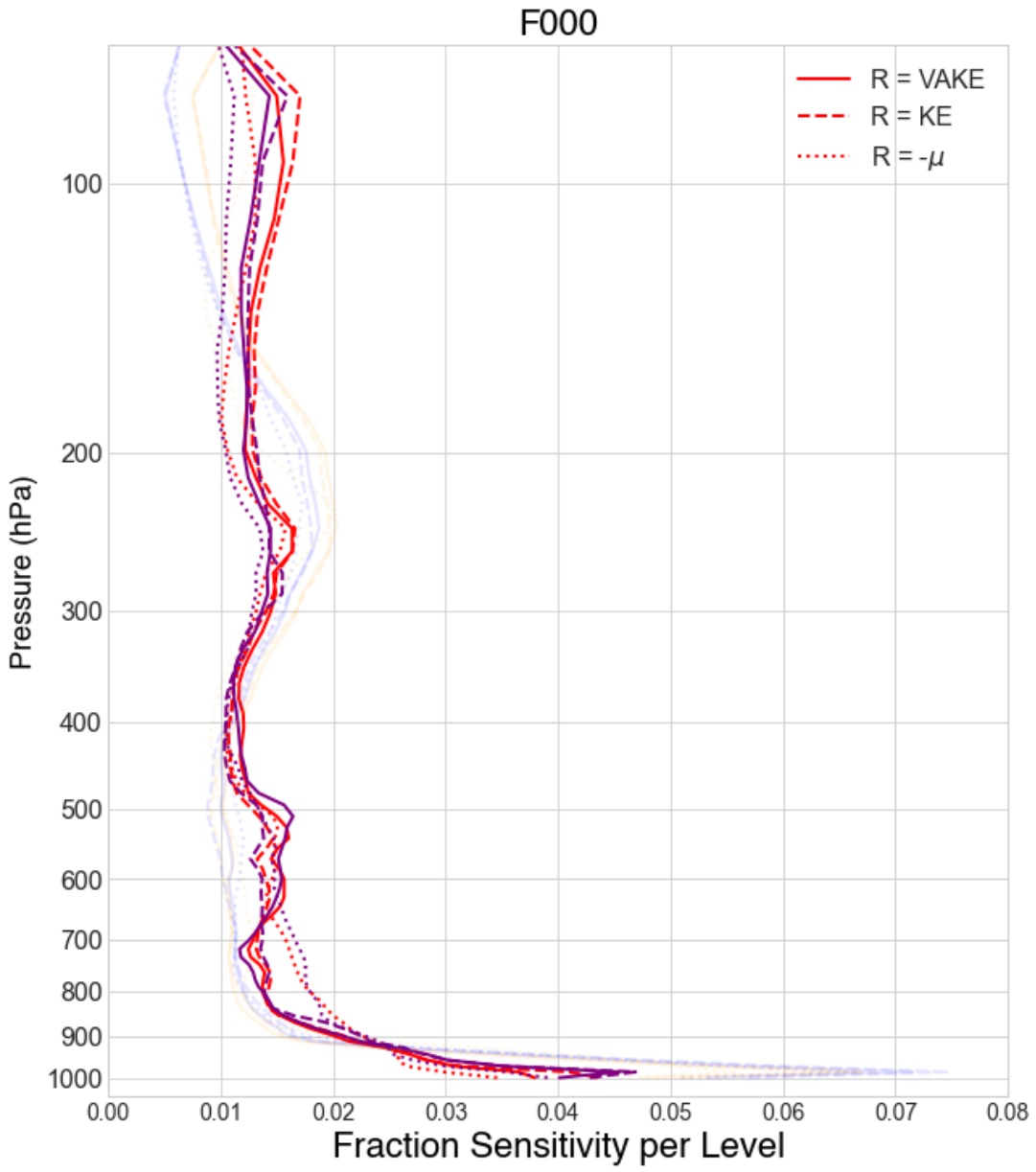

FIGURE 4.13: Valid at 0000 UTC 5 September 2017: sum of near TC (1000 km) sensitivity to zonal wind (red), meridional wind (purple), potential temperature (blue), and water vapor (orange) scaled by total magnitude of sensitivity. Response function R_{KE} (dashed line), R_{VAKE} (solid line), and R_{μ} (dotted line).

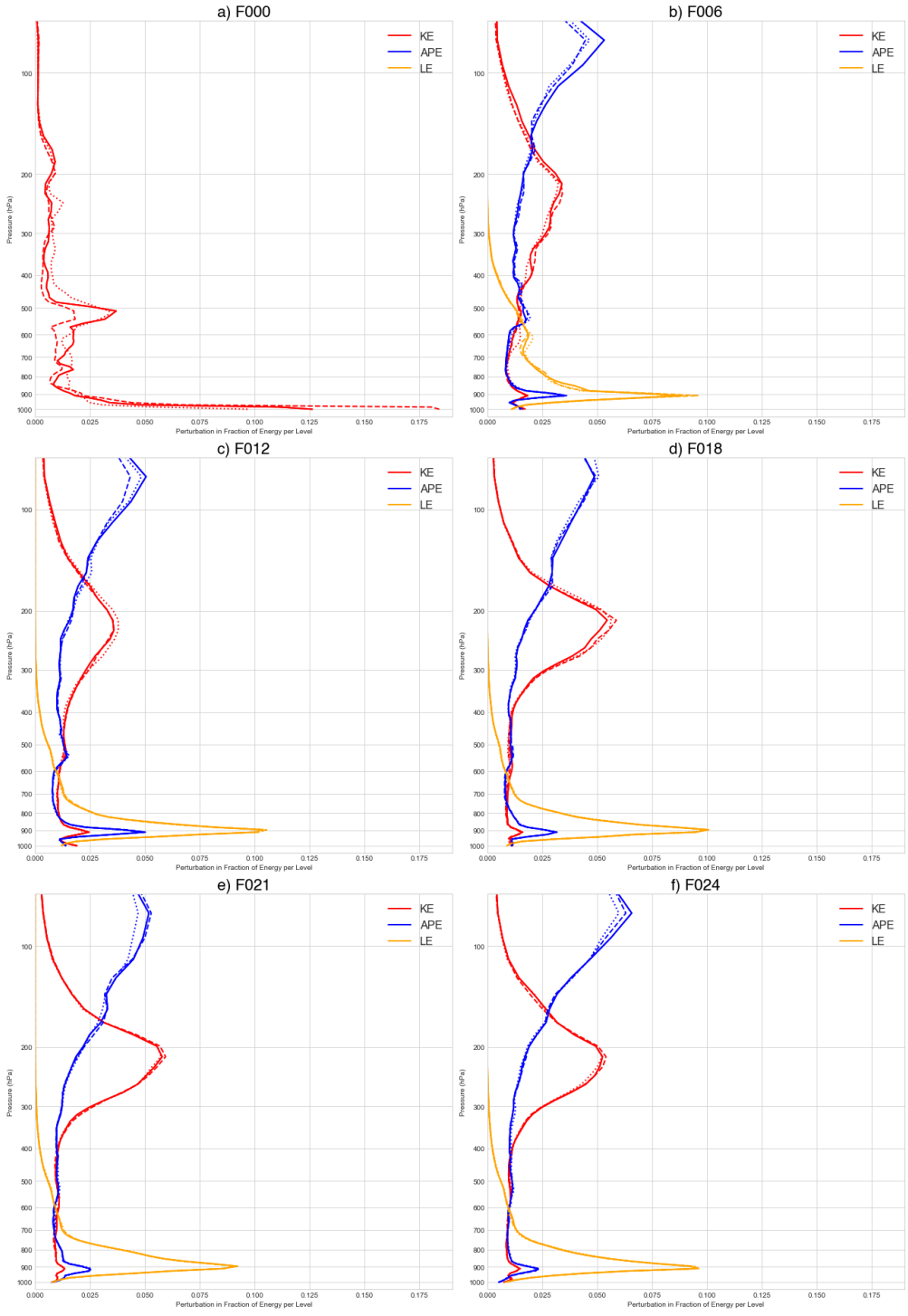

FIGURE 4.14: Perturbation of the kinetic energy (KE; red), available potential energy (APE; blue), and latent heat energy (LE; orange) normalized by the total change in their respective energy. Response function R_{KE} (dashed line), R_{VAKE} (solid line), and R_{μ} (dotted line). Valid at forecast hours F00, F06, F12, F18, F21, and F24.

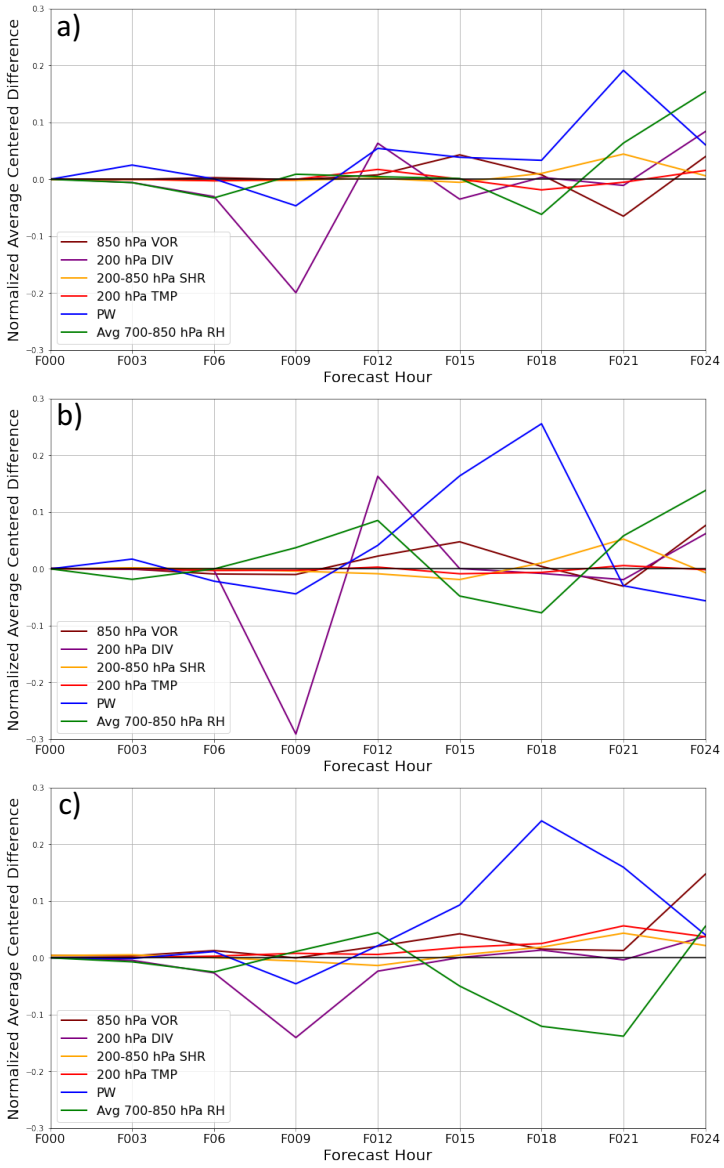

FIGURE 4.15: The normalized (difference divided by control value) storm relative averaged difference for each defined SHIPS-related variable. All values are calculated from a radius starting at the TC center, defined as the 850 hPa maximum vorticity. Variables 850 hPa relative vorticity (scaled by 1) from 0-1000 km radius (maroon), 200 hPa divergence (scaled by 1) from 0-1000 km (purple), 850 to 200 hPa vertical wind shear (scaled by 10) from 200-1000 km radius (yellow), 200 hPa temperature (scaled by 1000) centered from 0-1000 km radius (red), precipitable water (scaled by 100) centered from 100-200 km radius (blue), 700 to 850 hPa average relative humidity (scaled by 100) centered from 200-800 km radius (green). The values are scaled for ease of view. Panels show a) R_{KE} simulation, b) R_{VAKE} simulation, and c) R_{μ} simulation.

.

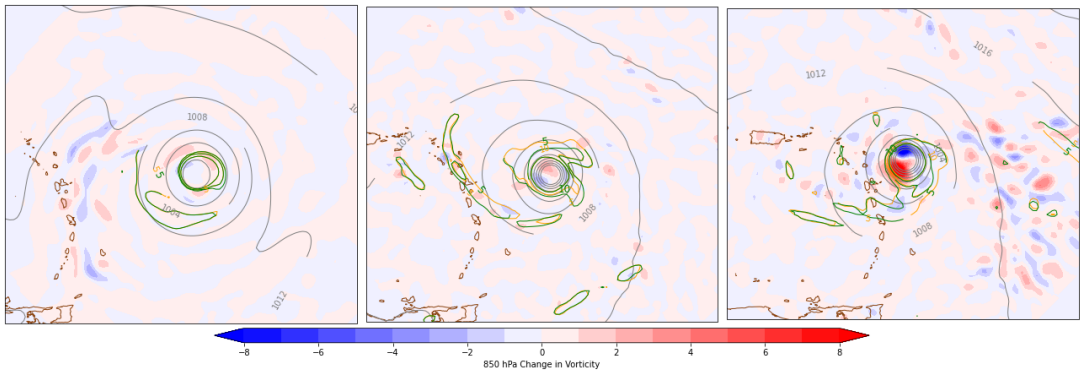

FIGURE 4.16: Kinetic Energy response function experiment (R_{KE}) perturbation 850 hPa vorticity (fill), control positive relative vorticity (solid green scale by 1e5 every 5 s^{-1}), perturbed positive relative vorticity (solid orange scale by 1e5 every 5 s^{-1} below 15), SLP (solid gray every 4 hPa above 980 hPa). Valid at F00, F12, and F24. Perturbations at time F00 scaled by 10.

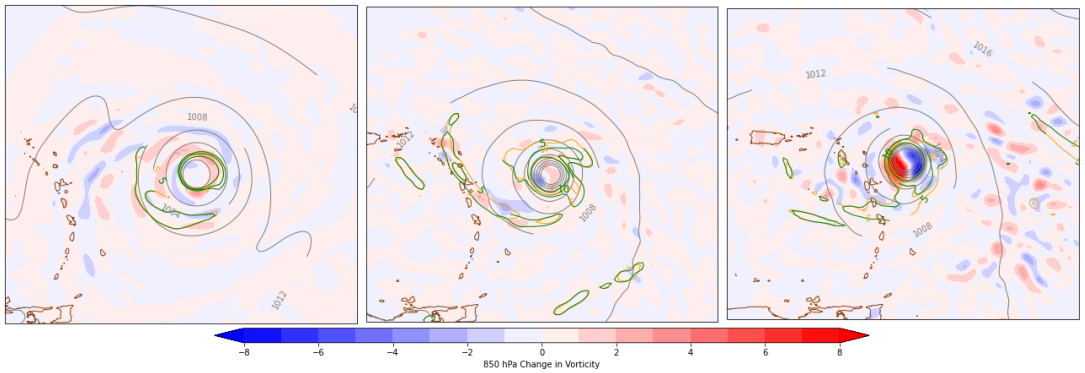

FIGURE 4.17: Same as Figure 4.16 except VAKE response function experiment (R_{VAKE}). Perturbations at time F00 scaled by 10.

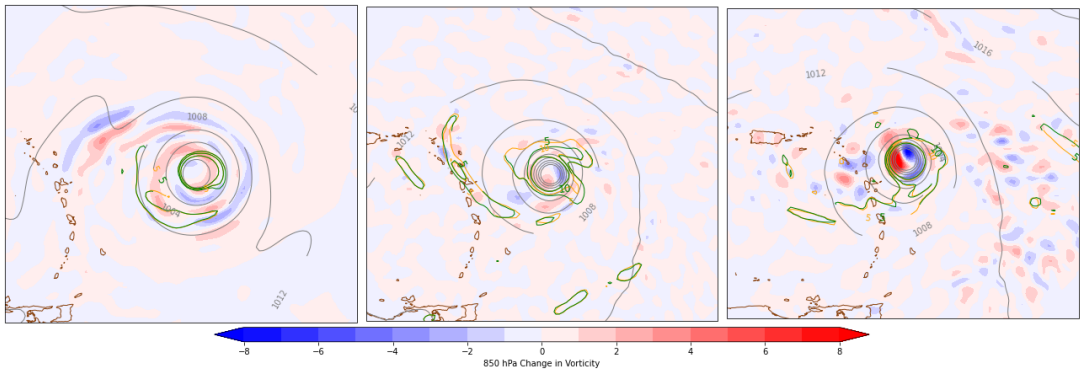

FIGURE 4.18: Same as Figure 4.16 except $-\mu$ response function experiment (R_μ). Perturbations at time F00 scaled by 10.

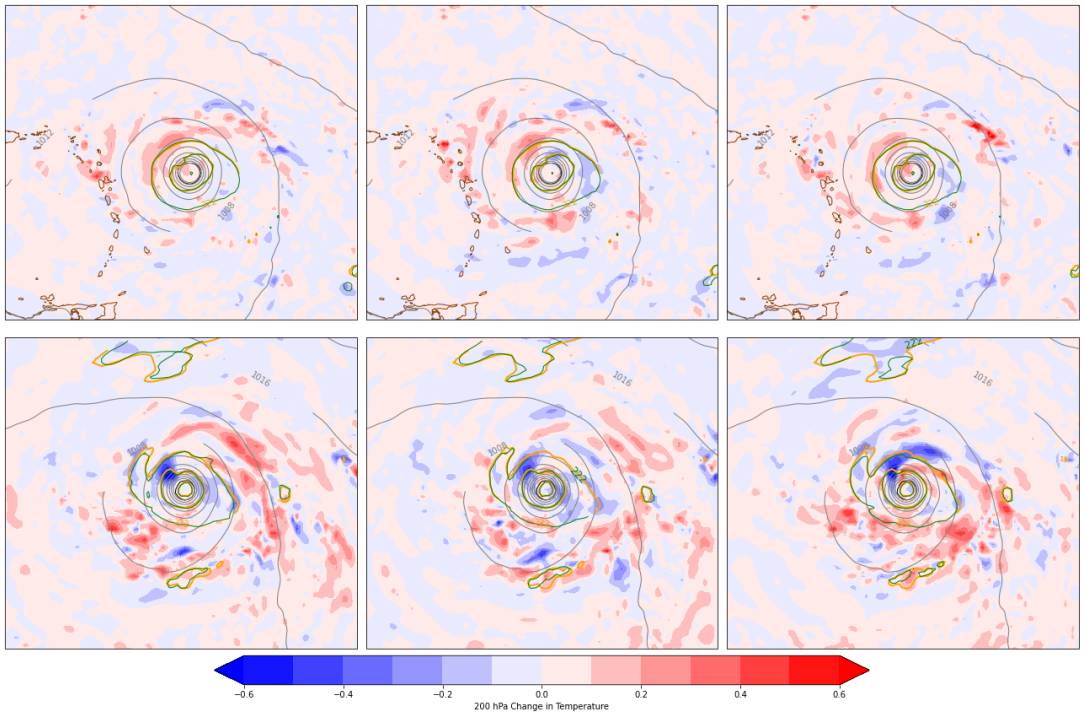

FIGURE 4.19: Each column for response functions R_{KE}, R_{VAKE}, and R_μ . Perturbation 200 hPa temperature within 1000 km of TC center (fill; K), control temperature (solid orange; K), perturbed temperature (solid green; K), SLP (solid gray every 4 hPa above 980 hPa). Valid at F12 (top row) and F24 (bottom row).

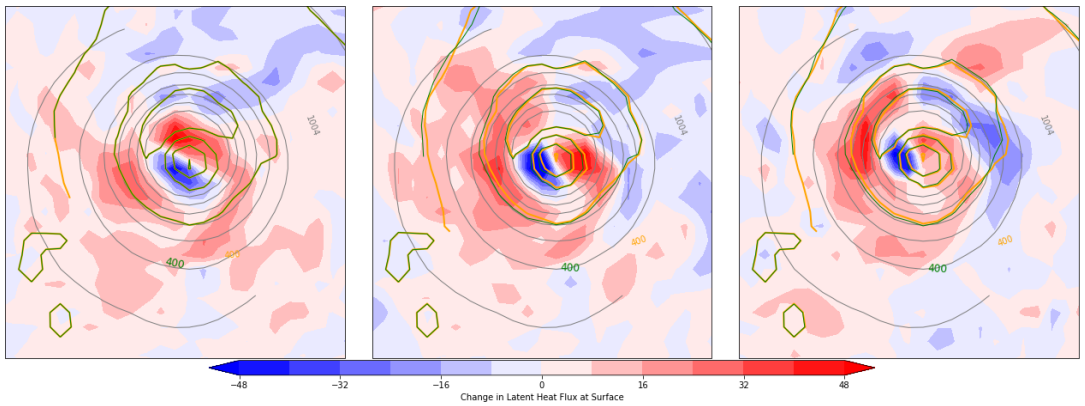

FIGURE 4.20: Each column for response functions R_{KE}, R_{VAKE}, and R_{μ}. Perturbation latent heat flux at surface within 180 km of TC center (fill; Wm^{-2}), control latent heat flux (solid orange; Wm^{-2}), perturbed positive relative vorticity (solid green; Wm^{-2}), SLP (solid gray every 4 hPa above 980 hPa). Valid at F24.

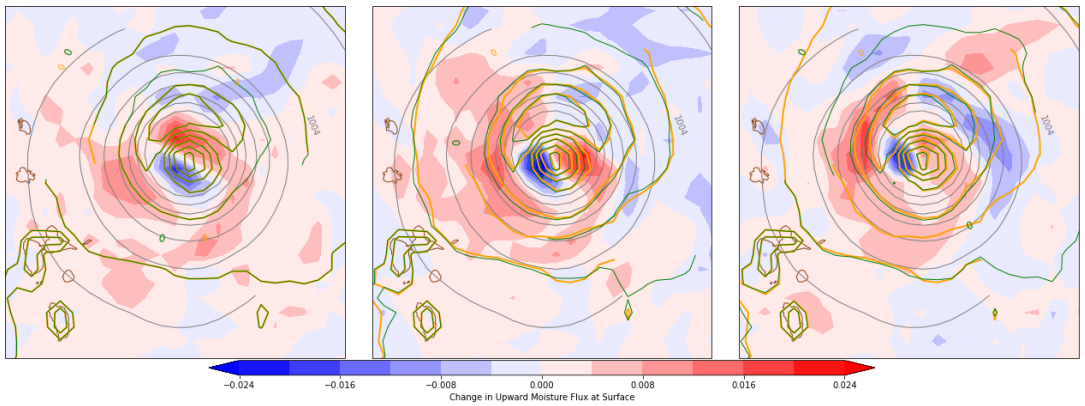

FIGURE 4.21: Same as Figure 4.20 except for upward moisture flux at the surface (g $\mathrm{m}^{-2}\mathrm{s}^{-1}$) .

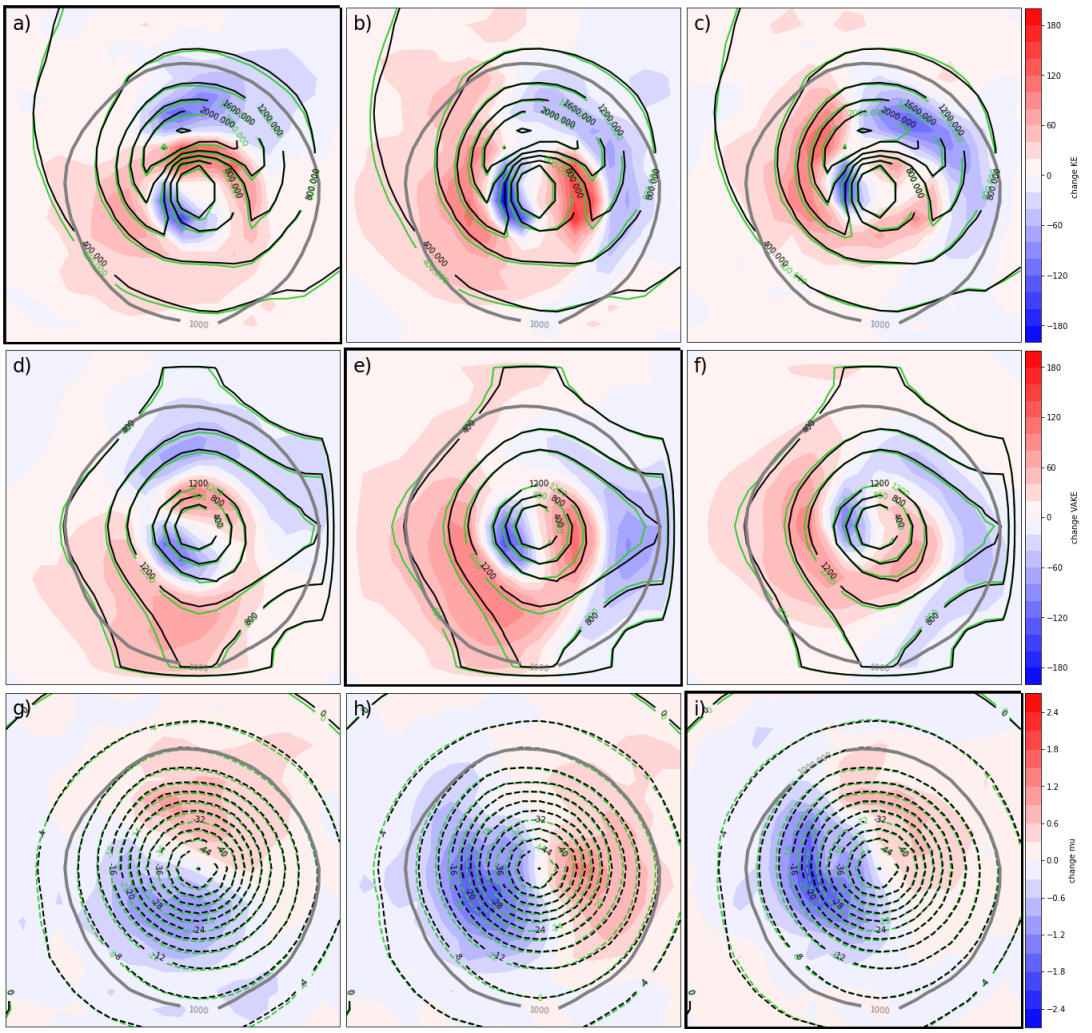

FIGURE 4.22: Each column for simulations from R_{KE}, R_{VAKE}, and R_{μ} adjoint sensitivities, respectively. a-c) Change in KE (m^2s^{-2}), d-f) change in VAKE (m^2s^{-2}), and g-i) change in mu (hPa). Fill is difference (perturbed minus control) for each respective variable, control variable (black) and perturbed variable (green). SLP 1000 hPa contour drawn for reference.

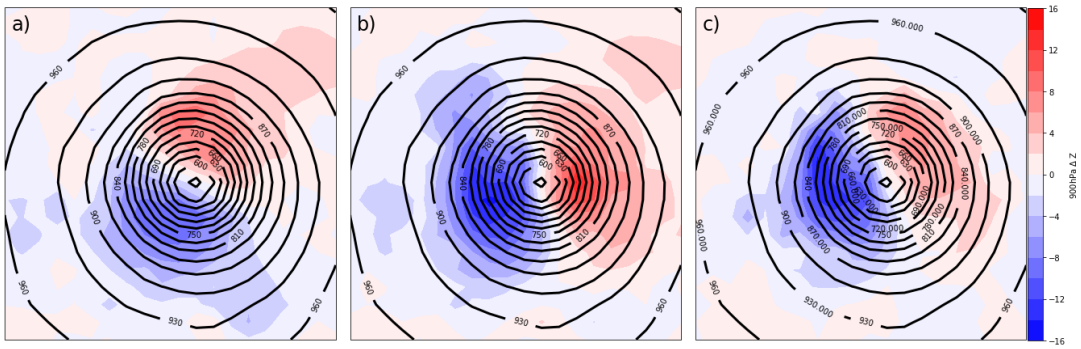

FIGURE 4.23: Each column for response functions a) R_{KE}, b) R_{VAKE}, and c) R_{μ}. Fill is difference (perturbed minus control) for 900 hPa geopotential height (fill; m) and control simulation geopotential height (black; m)

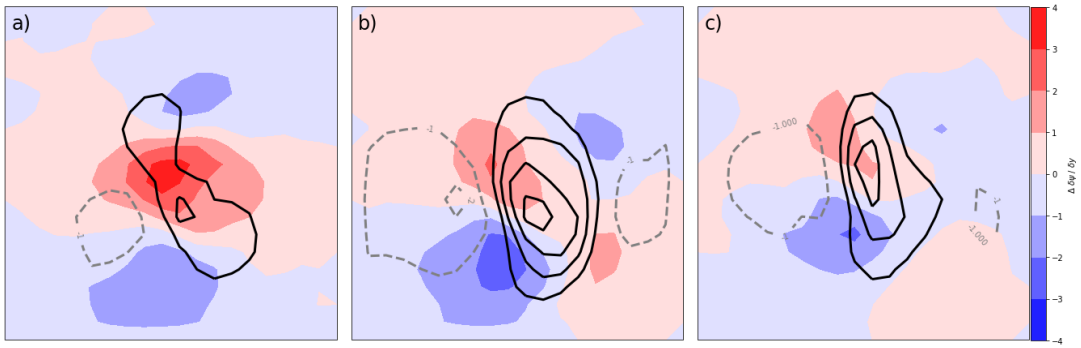

FIGURE 4.24: Each column for response functions a) R_{KE}, b) R_{VAKE}, and c) R_{μ}. Difference (perturbed minus control) of meridional gradient of stream function (fill; m^2s^{-1}/m), difference in zonal gradient of stream function (contoured; m^2s^{-1}/m) contoured at same interval as nonlinear perturbation. Stream function derived and averaged from the perturbed vorticity from model levels 6 to 10.

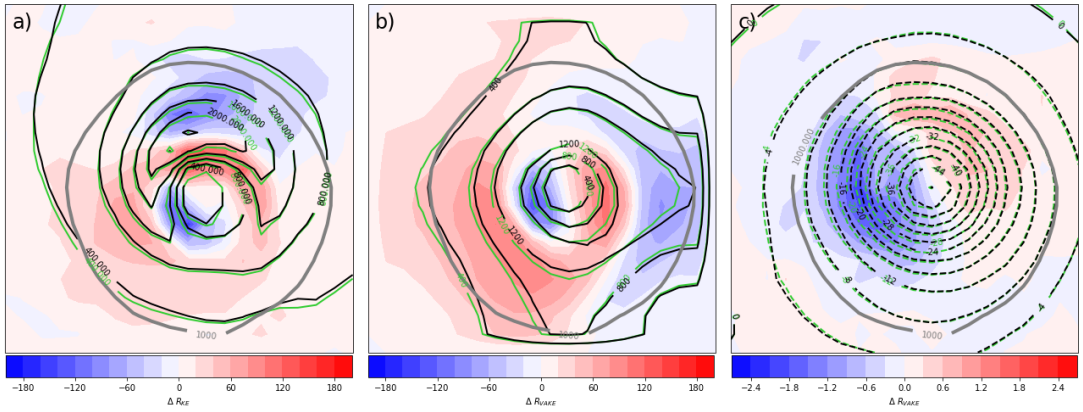

FIGURE 4.25: Valid 0000 UTC 6 September 2017 (F24) shown within response function domain: a) R_{KE} simulation ΔR_{KE} (fill; m^2s^{-2}), $KE_{control}$ (black contour; m^2s^{-2}) and KE_p (green contour; m^2s^{-2}), b) R_{VAKE} simulation ΔR_{VAKE} (fill; m^2s^{-2}), $VAKE_{control}$ (black contour; m^2s^{-2}) and $VAKE_{perturbed}$ (green contour; m^2s^{-2}), and c) R_{μ} simulation ΔR_{μ} (fill; hPa), $\mu_{control}$ (black contour; hPa) and μ_p (green contour; hPa). All 1000 hPa SLP contour (gray) for reference. KE and VAKE averaged from model level 6 to 10.

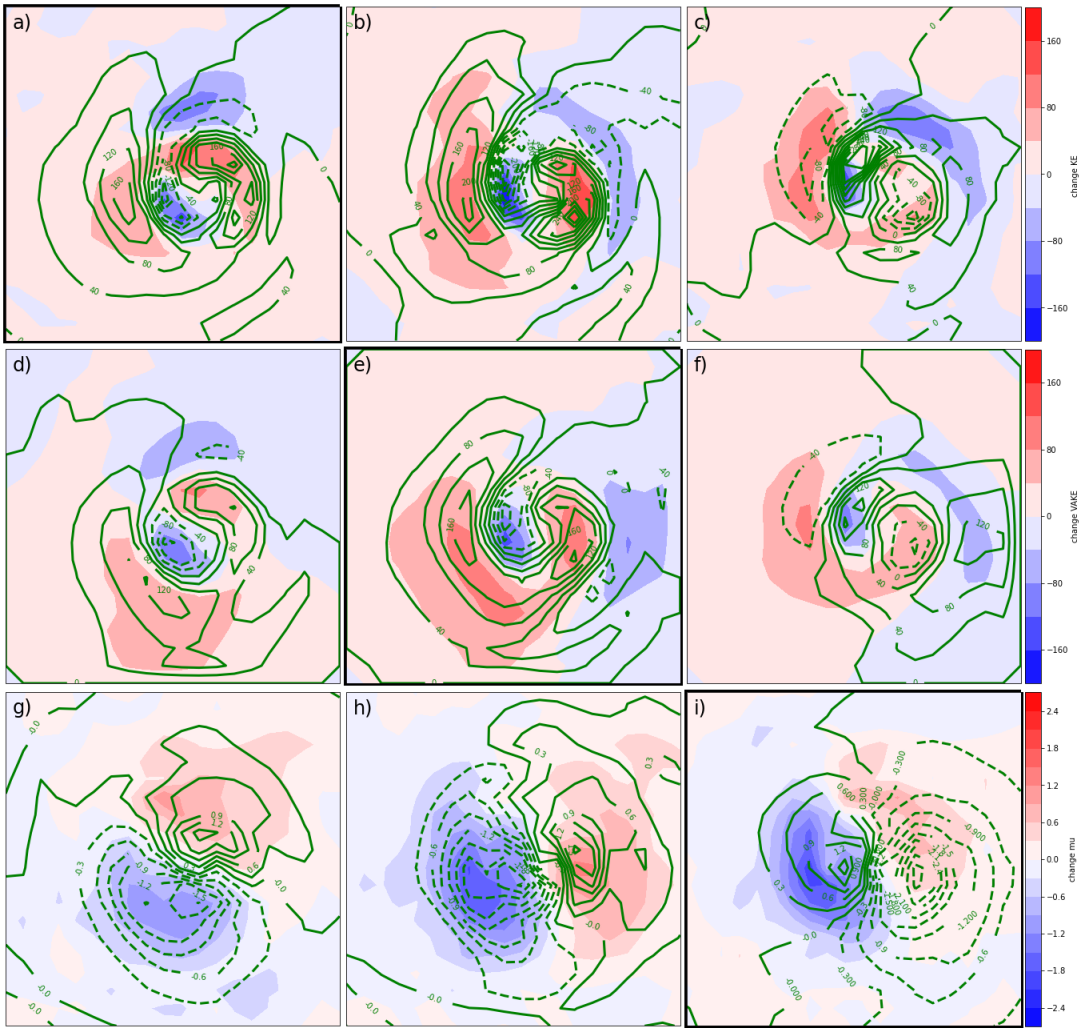

FIGURE 4.26: Each column for response functions R_{KE}, R_{VAKE}, and R_{μ}. a-c) Change in KE (m^2s^{-2}), d-f) change in VAKE (m^2s^{-2}), and g-i) change in μ (hPa). Fill is difference (perturbed minus control) for each respective variable as in Fig 4.22. Tangent linear perturbation (green) contoured at same interval as nonlinear perturbation.

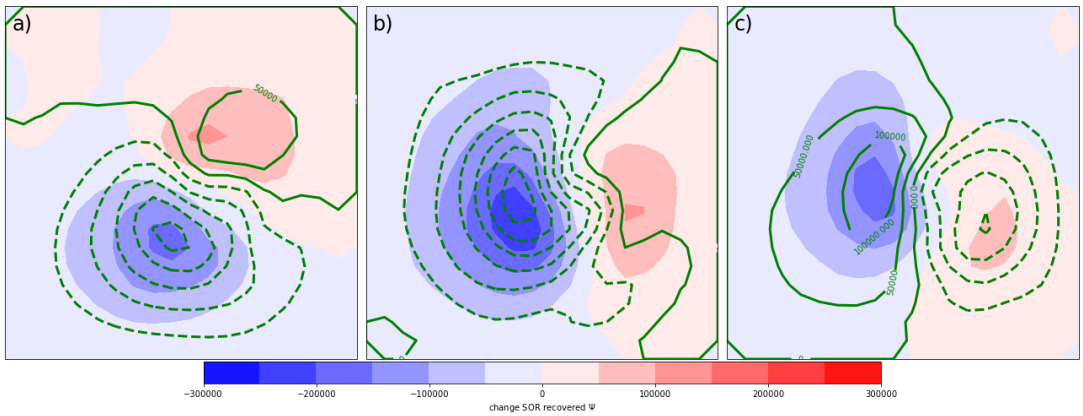

FIGURE 4.27: Each column for response functions a) R_{KE}, b) R_{VAKE}, and c) R_{μ}. Fill is difference (perturbed minus control) for the stream function derived from the perturbed vorticity. Tangent linear perturbation (green) contoured at same interval as nonlinear perturbation.

Chapter 5

In what regions is TC intensity change most sensitive?

5.1 Overview

Adjoint sensitivity studies typically involve perturbing a control forecast using optimal perturbations as described in prior chapters and in published studies (e.g., Doyle et al. 2012; Hoover 2015). Alternatively, perturbations to the initial state can be calculated using a scalar quantity to perturb particular variable(s), a certain region or feature of interest (e.g., intensifying a jet). It is hypothesized that by using a local projection operator (LPO) on optimal perturbations to evaluate specific regions in the model forecast, information can be gained about what physical processes are important for TC intensification.

Previous adjoint studies of tropical cyclone (TC) intensity have shown that while the largest intensity sensitivities (and by extension the largest adjoint-informed optimal initial perturbations) are at or near the surface (e.g., Doyle et al. 2012), as the perturbations evolve, the largest perturbation amplitudes (particularly for wind) are found higher in the troposphere. This is consistent with results shown in Chapter 3 and Chapter 4. This may suggest that the most efficient means to intensify the storm is through a"bottom up" intensification. This is found in other studies for extratropical storms as well (Goldstein 2018; Doyle et al. 2019). Sensitivities for most state variables, excluding pressure, have been found to be most sensitive within the lowest 2-3 km of the model simulation, with lower sensitivity extending throughout the atmosphere. Considering the typical order of magnitude for winds near the surface and near the outflow layer, a larger perturbation can be made to the upper troposphere while remaining relatively close to the basic state trajectory. It is hypothesized that through partitioning optimal perturbation into upper- and lower- tropospheric parts, information can be gained about the physical processes important to intensification, such as the evaluating whether the "bottom up" development is most effective. This hypothesis was tested in Chapter 3, where optimal perturbations were split between upper and lower pieces and scaled to prescribe the same change across all simulations. Results revealed the upper troposphere perturbation experiment created a larger change in the surface pressure, as well as upheld the tangent linear assumption. The full and lower perturbations resulted in a change in the surface pressure much smaller than the prescribed change and, as a consequence did not satisfy the tangent linear assumption. Analysis found that a notable difference between experiments was the earlier

and larger expansion of the outflow in the upper perturbation experiment that allowed for development to occur in contrast to the lower and full perturbations. A similar analysis was completed by Morgan (2021) to compare upper and lower troposphere perturbations in a case study of Hurricane Irma (2017). In this study, the perturbations were not scaled to prescribed the same change across experiment, resulting in a smaller expected change in the upper experiment than lower experiment. Consistent with the case study analyzed in Chapter 3, the upper perturbation experiment alone resulted in a lower surface pressure and held the tangent linear assumption better than in the full or lower perturbation experiments. Furthermore, the study showed upper perturbations resulted in decreasing the initial state outflow level relative vorticity and reducing the upper tropospheric inertial stability, which supports intensification (Morgan, 2021).

The evidence that upper perturbations alone can lead to TC development through changes in the outflow establishes a basis to investigate partitions of adjoint initial condition perturbations. Partitions can be made based on any arbitrary selection, however, in this chapter, partitions separate the model atmosphere into three experiments. In addition to evaluating the vertical structure of perturbations, the horizontal proximity of initial condition perturbations will be evaluated. As shown in previous chapters, in addition to sensitivities being concentrated in the lower troposphere, the largest sensitivities are within the near environment ($<$ 500 km radius from TC) of the TC. In this chapter, we will evaluate how perturbing the TC near environment versus far environments influence the physical processes important for development the TC. Lastly, while optimal perturbations are constructed to input the least amount of perturbation energy to result in the

prescribed change, not all perturbations made in the model will survive the nonlinear physical processes. It is hypothesized that restricting optimal perturbations to regions where the atmosphere is less resistant to lateral displacement will reduce the perturbations (and therefore linearity) lost to adjustments. As discussed in Chapter 1, the inertial stability can be quantified as the resistance to displacement by the Petterssen (1953) equation:

$$I_p^2 = \frac{1}{2}\left[(\zeta_\theta + f)^2 - D_\theta^2\right] \tag{5.1}$$

where I_p^2 is the inertial stability, f is the planetary vorticity, ζ_θ is the relative vorticity on an isentropic surface, and D_θ is the total deformation on an isentropic surface. Through partitioning the optimal perturbations based on positive and negative inertial stability, information about the role of inertial stability on TC intensification can be gained.

5.2 Model and Data

As in Chapter 4, this study focuses on a 24-hour period of Hurricane Irma (2017), initialized at 0000 UTC 5 September, using the Weather Research and Forecasting (WRF; v3.8.1) forward model (Skamarock and Coauthors, 2008) and its adjoint (Zhang et al., 2013). The WRF adjoint, available through WRFPLUSv3.8.1, has the adjoint of most moist physical processes for large scale condensation and the adjoint of a simplified cumulus scheme (Xiao et al. 2008; Chu et al. 2011). The WRF was initialized using the National Center for Environmental Predictions (NCEP) FNL (Final) operational global analysis on 0.25° x 0.25° latitude longitude grid available from the National Center for

Atmospheric Research (NCAR) Research Data Archive (RDA) as dataset ds083.3. The numerical simulation was run at 18 km horizontal grid spacing. The model was configured with 65 layers of evenly spaced vertical levels, from the surface to 50 hPa.

The response functions used is *vortex-associated kinetic energy* (VAKE) response function (R_{VAKE}), which measures the kinetic energy associated with the vorticity of the cyclone defined as:

$$R_{VAKE} = \frac{1}{N} \sum_{i,j,k \in D} \frac{1}{2}(u^2_{\zeta_{TC}ijk} + v^2_{\zeta_{TC}ijk}) \tag{5.2}$$

where ζ_{TC} is the vertical component of vorticity associated with the TC. The response function R_{VAKE} is the sum of a subset of the kinetic energy associated with only the vorticity that exists within the 3-dimensional lower-tropospheric volume centered on the TC. Further details can be found in Section 2.1.2.

The case study and synoptic evolution are discussed in Chapter 4, as well as the adjoint-derived sensitivities. For brevity, more information can be found in that chapter and will be referred to as the control simulation. The case study involving the perturbations using the response function R_{VAKE} in Chapter 4 will be referred to as the full perturbation experiment (FPE).

The following section will describe the partitioned experiments performed and the impact the partitioning had on TC intensity change and tangent linear assumption.

5.3 Partition Experiments

To investigate these questions, optimal perturbations based on the adjoint sensitivities described in section 4.4.3 are calculated. As in the full domain perturbed simulation, optimal perturbations u' and v' were constructed using the energy norm discussed in Chapter 2. For the following experiments, a local projection operator (LPO) is used to partition the model atmosphere. Sensitivities outside of the specified region are set to zero using the LPO. The prescribed change to constrain the norm was a 5% average increase in the VAKE within the response function domain. The experiments are named and defined in Table 5.1.

Experiment	**Specific Change**	**Restriction**
Experiment 1	a) Lower Model	LPO levels 0 to 30; all horizontal
	b) Upper Model	LPO levels 30 to 65; all horizontal
Experiment 2	a) $\leq$ 1008 hPa	LPO within 1008 hPa contour (all vertically)
	b) >1008 hPa	LPO outside 1008 hPa contour (all vertically)
Experiment 3	a) I^2 <0	LPO inertially unstable and above BL
	b) I^2 >0	LPO inertially stable and above BL

TABLE 5.1: List of 6 optimal perturbation simulations partitioned by level(s) in atmosphere (Experiment 1), proximity to TC (Experiment 2), and inertial stability (Experiment 3)

Experiment 1 consists of two partitions, the lower troposphere (EXP1a) and the upper troposphere (EXP1b). The vertical partition of the atmosphere is at model level 30 of 65, which corresponds approximately 500 hPa. This can be seen through a cross section of the initial state perturbed meridional wind (Fig 5.1). Perturbations are scaled in the figure for emphasis, with the actual perturbations size from the FPE shown in green. Together EXP1a and EXP1b add to the prescribed change (δR) as seen in Table 5.2

Experiment 2 consists of two partitions as well, separating the perturbations from the TC (EXP2a) and its environment (EXP2b). The separating of the TC and its environment is defined as the area encompassed by the surface 1008 hPa SLP contour, which is approximately 500 km. This area is extended vertically in these experiments as shown in Fig 5.2. As evident in Fig 5.2, EXP2a perturbations are in within the TC core and strongest radial gradient of wind in the lower troposphere. The EXP2b perturbations are outside of the TC core and strong radial gradient of wind, separating the experiments into TC and environmental perturbations (at least in low levels). Together EXP2a and EXP2b add to the prescribed change (δR) as seen in Table 5.2.

The final experiment set, experiment 3, also consists of two partitions, separating perturbations by inertially unstable (EXP3a) and inertially stable (EXP3b) regions (Fig 5.3). As the inertial stability is calculated on isentropic surfaces, interpolation resulted in the loss of perturbations near the surface, within the well-mixed layer. To account for this, the lowest 6 eta levels were all set to zero for both EXP3a and EXP3b. An additional simulation with the lowest 6 model levels of sensitivities removed was performed and compared to the FPE to test whether this would result in a large change in the perturbation evolution, which it did not for this case. The initial perturbations to wind fields are concentrated in inertially unstable regions as seen in the percent change associated with EXP3a in Table 5.2. Additionally, it is notable the EXP2a and EXP3a show highly similar distributions, except for exceedingly small perturbations in the inner core in the middle and upper troposphere. Together EXP3a and EXP3b add to the nearly prescribed

change (δR) as seen in Table 5.2, this value is lower than 5% due to the lack of boundary layer perturbations.

	% VAKE	LR	Δ SLP	SLP_{min}	$\Delta\zeta$
FPE	5.0	0.42	-0.068	959.1	0.203
EXP1a	3.69	0.29	-0.0036	959.2	0.0975
EXP1b	1.31	1.52	-0.046	958.9	0.149
EXP2a	1.93	0.60	-0.0063	959.2	0.137
EXP2b	3.07	0.25	0.020	959.1	-0.00749
EXP3a	2.13	0.67	0.0054	959.0	0.112
EXP3b	0.388	2.05	-0.020	959.1	0.116

TABLE 5.2: List of 6 optimal perturbation simulations. Columns show the initial percent change of VAKE (% VAKE), the final time (forecast hour 24) linearity ratio (LR), the change in average SLP within response function domain (Δ SLP), the minimum SLP (SLP_{min}), and the change in average vorticity within response function domain ($\Delta\zeta$)

As anticipated, at initialization all perturbations are associated with perturbing the zonal and meridional wind components. The perturbation kinetic energy (KE) for all experiments can be seen in Fig 5.4. At the initial time, there is considerable spread between experiments, however, a cluster of EXP1b, EXP2a, and EXP3a can be seen with a maxima in perturbed KE centered at 500 hPa (Fig 5.4a). At forecast hour 3, perturbed KE in EXP1b and EXP2a remain closely related with a maximum around 100 to 200 hPa (Fig 5.4b). A similar cluster of EXP1a and EXP2b is seen at initialization, with a maximum in the boundary layer perturbed KE (Fig 5.4a). This relationship continues 3 hours into the forecast, with a broad maximum from 200 to 400 hPa (Fig 5.4b). By 12 hours into the forecast, there is little discernible difference in any of the experiments perturbed energy, particularly in the lower troposphere (Fig 5.4c). This difference narrows 24 hours

into the forecast (Fig 5.4d), with the greatest spread in the upper troposphere and lower stratosphere in the perturbed KE and APE.

The following subsections will include a brief discussion of the evolution of each set of experiments, including the impact of the partitioned experiment on the response function and SHIPS-related variables.

5.3.1 Experiments 1: Vertical Partitions

In experiment 1, the larger percent change is associated with EXP1a (Table 5.2) as expected from the analysis completed in Chapter 4. As perturbations evolve, the difference in SHIPS-related variables are small until 9 hours into the forecast, when changes in the 200 hPa divergence decreases most for EXP1b (Fig 5.5b). At 12 hours into the forecast, the FPE experiences an increase the 200 hPa divergence, while EXP1a and EXP1b remain near the control, after which all three experiments show little change from the control. The change in relative humidity shows little difference across the FPE, EXP1a and EXP1b (Fig 5.5f). At forecast hour 9, the PW in EXP1b decreases while for EXP1a, PW increases, with EXP1a retaining higher PW through 15 hours into the forecast. After 15 hours into the forecast, the PW remains constant or decreases through forecast hour 24 in EXP1a while EXP1b increases (Fig 5.5e). The 200 hPa temperature change remains small through forecast hour 12, after which a decrease is seen in EXP1a, FPE, and EXP1b, in increasing magnitude of decrease. This separation continues until 24 hours into the forecast, where the 200 hPa change in temperature in EXP1b is slightly negative, near zero for the FPE, and positive for the EXP1b (Fig 5.5d). At the final time,

the change in the 850 hPa vorticity is largest for the FPE followed by the EXP1b and EXP1a (Fig 5.5a). Recall that since the prescribed is smallest for EXP1b, it is expected that the change in vorticity is smallest for EXP1b.

Examining the changes at the final time across experiment 1, the linearity ratio (LR) is closer to 1 for EXP1b (LR = 1.52) than EXP1a (LR = 0.29) or the FPE (LR = 0.42), as seen in Table 5.2. This change can also be seen in Fig 5.6. The distribution of change in VAKE is consistent across this set of experiments. Consistent with the FPE, the TC shifts to the west 24 hours into the forecast which is shown in both Fig 5.6 and Fig 5.7. In EXP1b, the shift is also slightly to the south. While the largest decrease in average change in SLP is associated with the FPE, the minimum SLP is associated with EXP1b (Table 5.2). Similarly to the analysis performed in Chapter 3, EXP1b results in the least amount of change and lowest linearity ratio even through it is closely related to the FPE.

5.3.2 Experiments 2: Horizontal Partitions

In experiment 2, the larger percent change is associated with EXP2b (Table 5.2), as it encompasses the majority of the model atmosphere. Similar to experiment 1, perturbations remain small and closely related until 9 hours into the forecast, with separation in the 200 hPa divergence and temperature, and PW (Fig 5.8). However, unlike experiment 1, the changes are tightly clustered about the FPE and lack notable differences in trends. At the final time, the largest spread is in the PW and average RH, with EXP2 being larger in both cases (Fig 5.8e and f). The 850 hPa vorticity and 200 hPa divergence is nearly identical across simulations 24 hours into the forecast (Fig 5.8a and b).

Examining the changes at the final time across experiment 2, the LR is closer to 1 for EXP2a (LR = 0.60) than EXP2b (LR = 0.25) as seen in Table 5.2. This change can also be seen in Fig 5.9. The distribution of change in VAKE is shows a difference in orientation, with EXP2a developing to the south and west (Fig 5.9b) while EXP2b shows less change and is oriented more north and west (Fig 5.9c). This is also evident in Fig 5.10. The average change in SLP is small and negative for EXP2a, while positive for EXP2b. However, it has a lower minimum SLP than EXP2a. Across all experiments, EXP2b is the only simulation that results in the average relative vorticity within the response function domain decreasing (Table 5.2).

5.3.3 Experiments 3: Inertial Stability Partitions

In experiment 3, the larger percent change is associated with EXP3a (Table 5.2), revealing that adjoint sensitivities to the components of the horizontal wind are co-located with low inertial instability. Perturbations again remain small and closely related until 9 hours into the forecast, with separation in the 200 hPa divergence and PW (Fig 5.11b and e). The EXP3a PW decreases initially relative to FPE at forecast hour 9, then increases until 15 hours into the forecast when it remains approximately constant and positive through the final, 24 forecast hour (Fig 5.11e). This contrast to EXP3b, which exhibits little change throughout the simulation and 24 hours into the forecast is negative. The 200 hPa temperature 24 hours into the forecast for EXP3a is negative while EXP3b is positive (Fig 5.11d). From a Carnot cycle perspective, the EXP3a is more favorable for a stronger TC intensity (change). The change in 850 hPa vorticity is largest for EXP3a

at forecast hour 24 compared to both the FPE and EXP3b (Fig 5.11a).

Examining the differences 24 hours into the forecast across experiment 3, the LR is closer to 1 for EXP3a (LR = 0.67) than EXP3b (LR = 2.05) as seen in Table 5.2. The large linearity ratio for EXP3b is likely associated with the very small prescribed change. This change can also be seen in Fig 5.12. The distribution of change in VAKE is shows a slightly more south and west change in VAKE for EXP3a (Fig 5.12b) while EXP3b shows less change and is oriented more north and west (Fig 5.12c). This is also evident in Fig 5.13. The average change in SLP is small and positive for EXP3a, while negative for EXP2b. However, EXP3a has a lower minimum SLP than EXP3b and FPE. The average change in relative vorticity within the response function domain consistent between EXP3a and EXP3b (Table 5.2).

5.3.4 Partitions Discussion

The partitioning of adjoint perturbations had an effect on both the TC intensity and linearity ratio. As noted at the initial time, vertical distributions of perturbation KE, the EXP1b, EXP2a, and EXP3a reveal a similar structure in the middle and upper troposphere, with a maximum in perturbation KE at about 500 hPa (Fig 5.4a). As these three experiments evolved to the final forecast hour, they result in the highest linearity ratio (Table 5.2). Furthermore, EXP1b, EXP2a, and EXP3a result in a more northwest shift and development than the FPE, EXP1a, EXP2b, and EXP3b all which are dominated by a westward shift and development. The consistent signal across these simulations indicates that the distribution of initial perturbations for EXP1b, EXP2a,

and EXP3a lead to a more robust TC vortex. Furthermore, within the context of an adjoint study, results from these three experiments suggest that certain partitions of adjoint sensitivities are less likely to result in highly nonlinear simulations.

5.4 Perturbations in Inertially Unstable Regions

An inertially unstable upper troposphere supports the development of TC outflow, as air can expand outward laterally without doing work on the environment. It is found that adjoint sensitivities to wind are highly collocated with inertially unstable regions, at all levels. In the case study of Hurricane Irma (2017), it is found that 82% of the sensitivities to zonal and meridional wind are in inertially unstable regions. To a lesser extent, sensitivities to temperature and moisture are found in these regions as well. Fig 5.14 provides an example of the upper and lower model troposphere of this relationship between sensitivity gradients and inertial stability. In the lower troposphere (312 K), sensitivity gradients remain outside of the core of high inertial stability while in the upper troposphere (358 K), this relationship is less clear particularly seeing the sensitivity to potential temperature overlapping with the inertially stable core. This relationship leads to multiple research questions to understand this relationship: (1) Does a more asymmetric inertial stability field prime a TC for development? (2) How do potential temperature perturbations in inertially stable or unstable regions influence intensity? (3) Does lower inertial stability in the surrounding environment of a developing TC lead to a more robust intensification?

As seen in section 5.3.4, perturbations made only in inertially unstable regions (EXP3a)

result in a greater LR than perturbations in inertially stable (EXP3b). It is not evident at initialization that the perturbations systematically change the distribution of inertial stability in either simulation. As the prescribed change is not equal and EXP3a does not hold the tangent linear assumption, statements of which resulted in a greater change in the TC cannot be made. To address this issue, an additional simulation (EXP3c) perturbing inertially stable regions was made that is equal to EXP3a (2% of the response function domain VAKE). The LR in EXP3c is 0.28, with a small average decrease in SLP (-0.02 hPa). Comparing EXP3a to EXP3b and EXP3c, it is evident that perturbing inertially unstable regions will result in the tangent linear assumption being held and thus a more intense TC. The following discussion will evaluate how the TC intensified.

As seen in the SHIPS-related time series (Fig 5.8a), the 850 hPa vorticity exhibits little change from initialization to 21 hours into the forecast, with an increase at forecast hour 24. The horizontal distribution of change in 850 hPa vorticity shows the same lack of substantial change, with the forecast hour 24 change consistent with the FPE (Fig 5.15). The close relationship between the FPE and EXP3a at the final time is expected as they share the same response function. The changes in the azimuthal wind do not reveal clear signals in the evolving azimuthal flow (Fig 5.16). This may be due to a significant asymmetric distribution of the perturbations smearing out any azimuthally averaged signal. At the final time, there is a slight indication the TC contracting closer to the core and lowering the vertical extent of the cyclonic azimuthal flow (Fig 5.16b). The decrease in the strength of the azimuthal wind in the upper troposphere indicates that the azimuthal flow decreasing in the outflow levels. Additionally, the inner gradient

of the radius of maximum winds in the mid-troposphere has increased. The perturbed radial wind 24 hours into the forecast indicate a shifting inward of the radial outflow in the upper troposphere (Fig 5.17b). The mid-troposphere also indicates a shifting inward, consistent with the azimuthal wind change. Additionally, a slightly stronger radial inflow near the surface.

In the upper troposphere, the average 200 hPa temperature change is small, 12 hours into the forecast the average 200 hPa temperature has increased slightly (Fig 5.18c), similar to the FPE. The largest change occurs 24 hours into the forecast, when EXP3a decreases the average 200 hPa on average compared to the control and FPE (Fig 5.18d). This change in Fig 5.18a) is notably asymmetric around the core. A similar change can be seen in the evolving equivalent potential temperature (Fig 5.19d). At that time, the azimuthally averaged equivalent potential temperature change reveals an increase in the warm core of the TC with an decrease in the equivalent potential temperature in the outflow layer (Fig 5.20). The decrease in the 200 hPa (equivalent) potential temperature is likely associated with the contraction of the TC in the outflow levels seen in the azimuthally averaged azimuthal and radial wind. This is evident in the more vertically aligned equivalent potential temperature contours (Fig 5.20).

Evaluating the change in the response function in the nonlinear and tangent linear models, as seen in Fig 5.12, EXP3a results in a slightly more southwest change in location than the FPE or EXP3b. The magnitude of change in the nonlinear VAKE is largest for EXP3a then FPE and EXP3b, respectively. The tangent linear perturbation VAKE is the largest

for the FPE, which is consistent with the largest prescribed change is associated with the FPE (Fig 5.21). The shift in position across the three simulations, best seen in the change in perturbation dry air pressure, aligns most closely with the FPE (Fig 5.21b). Comparing the change in SLP in Table 5.2, this is expected as EXP3a does not result in a lower average SLP within the response function domain despite its high LR and increase in both 850 hPa relative vorticity and the relative vorticity within the response function domain. This adds to the discussion in Chapter 4 about how intensity is defined.

5.5 Conclusions

Adjoint-derived initial condition perturbations can be partitioned by variable or region to evaluate the role that the variable or region has on the response function. Experiments were conducted to evaluate the impact of such partitioning in three sets of experiments: (1) vertical partition of the atmosphere, (2) within the near TC environment and outside the near TC environment, and (3) partitions based on inertial stability. In all three partitions, one partition performed more optimally - including improving on the linearity ratio compared to the full, non-partitioned simulation (FPE). The highest LR experiments (EXP1b, EXP2a, and EXP3a) reveal a similar importance of mid-troposphere perturbation KE (i.e., initial horizontal wind perturbations) at initialization, which quickly extends to upward to the outflow level by 3 hours into the forecast, particularly for EXP1b and EXP2a. At the final time, all three simulations result in a more southward shift and broadening than the FPE or the low LR simulations (EXP1a, EXP2b, and EXP3b) which all result in a more westward shift and lower-tropospheric broadening.

The impact of the experiments performed in this chapter reveal that within an adjoint framework, where perturbations are made has an influence on how well the tangent linear assumption is held, consistent with the findings in Chapter 3. This information can be leveraged for future adjoint case studies to reduce limitations, such as the duration or resolution of the simulation, while still adhering to the tangent linear assumption.

The evolution of perturbations in EXP3a do not reveal unique pathways or changes compared to the FPE. The evolution of SHIPS-related variables shows a consistent average change at most time steps, except for 200 hPa temperature and PW 24 hours into the forecast. In both variables, EXP3a the change seen is favorable for a more intense TC. While the LR is higher for EXP3a magnitude of the maximum and minimum change in VAKE is similar between EXP3a and the FPE, which is due to the smaller prescribed change in EXP3a. Furthermore, while EXP3a has the highest linearity found across all partitioned experiments in this chapter, it does not decrease the average SLP – though it does reduce the minimum grid point SLP by 0.2 hPa compared to the FPE. The more intense TC as defined by VAKE, and also by average vorticity within the response function domain, but not by surface pressure enforces the discussion in Chapter 4 of the need to carefully define the response function. As evident in Table 5.2, within the response function domain the magnitude and sign of the change in average vorticity and sea level pressure are not anti-correlated.

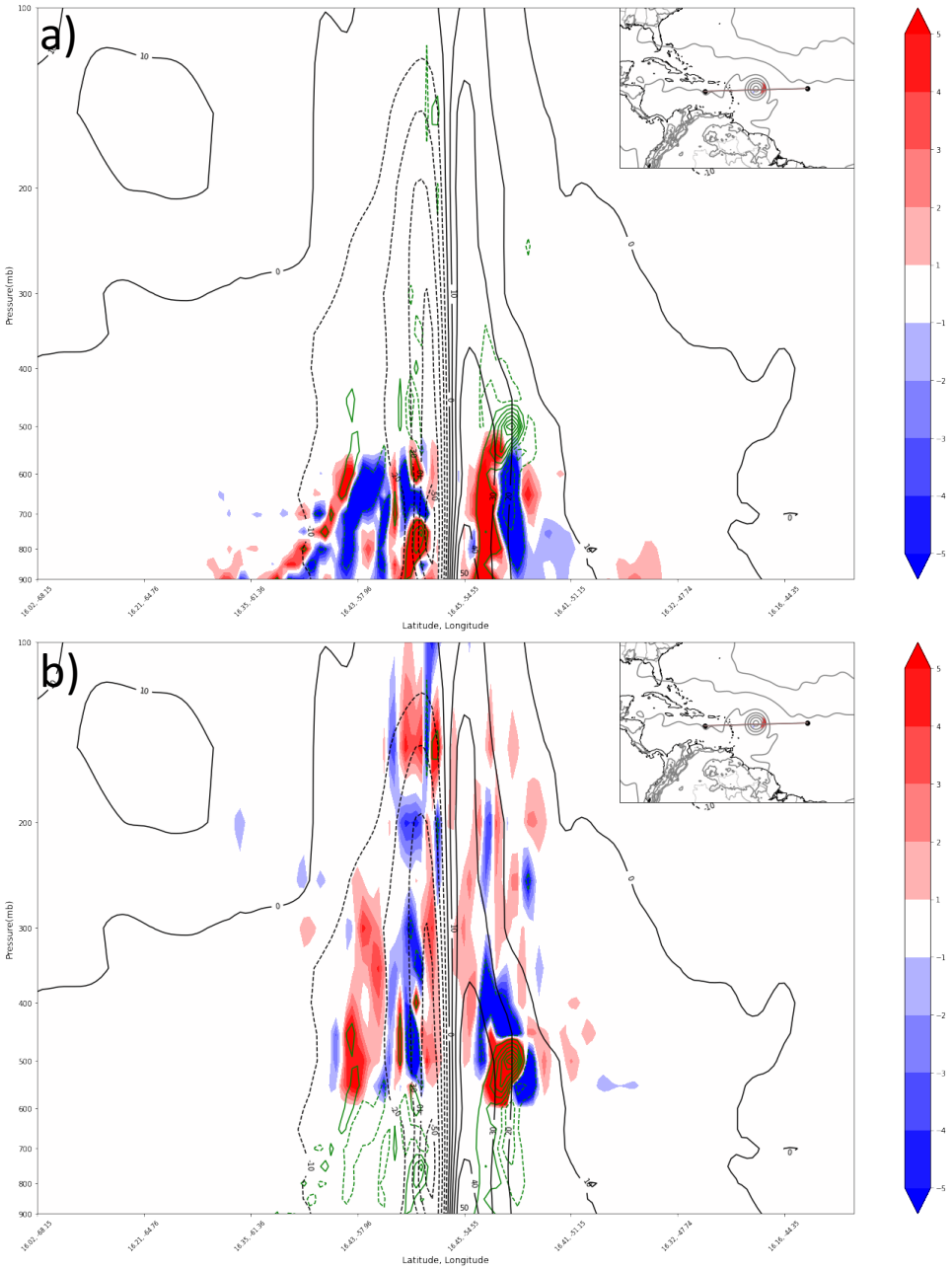

FIGURE 5.1: Valid at 0000 UTC 5 September 2017. The partitioned optimal perturbation to meridional wind field scaled by 100 (fill, ms^{-1}), FPE optimal perturbation meridional wind field (green, 0.1 ms^{-1}), meridional wind field (solid black line every 10 ms^{-1}). Inset is the 500 hPa FPE optimal perturbation meridional wind field and SLP with the cross section orientation. Panel a) EXP1a and b)EXP1b

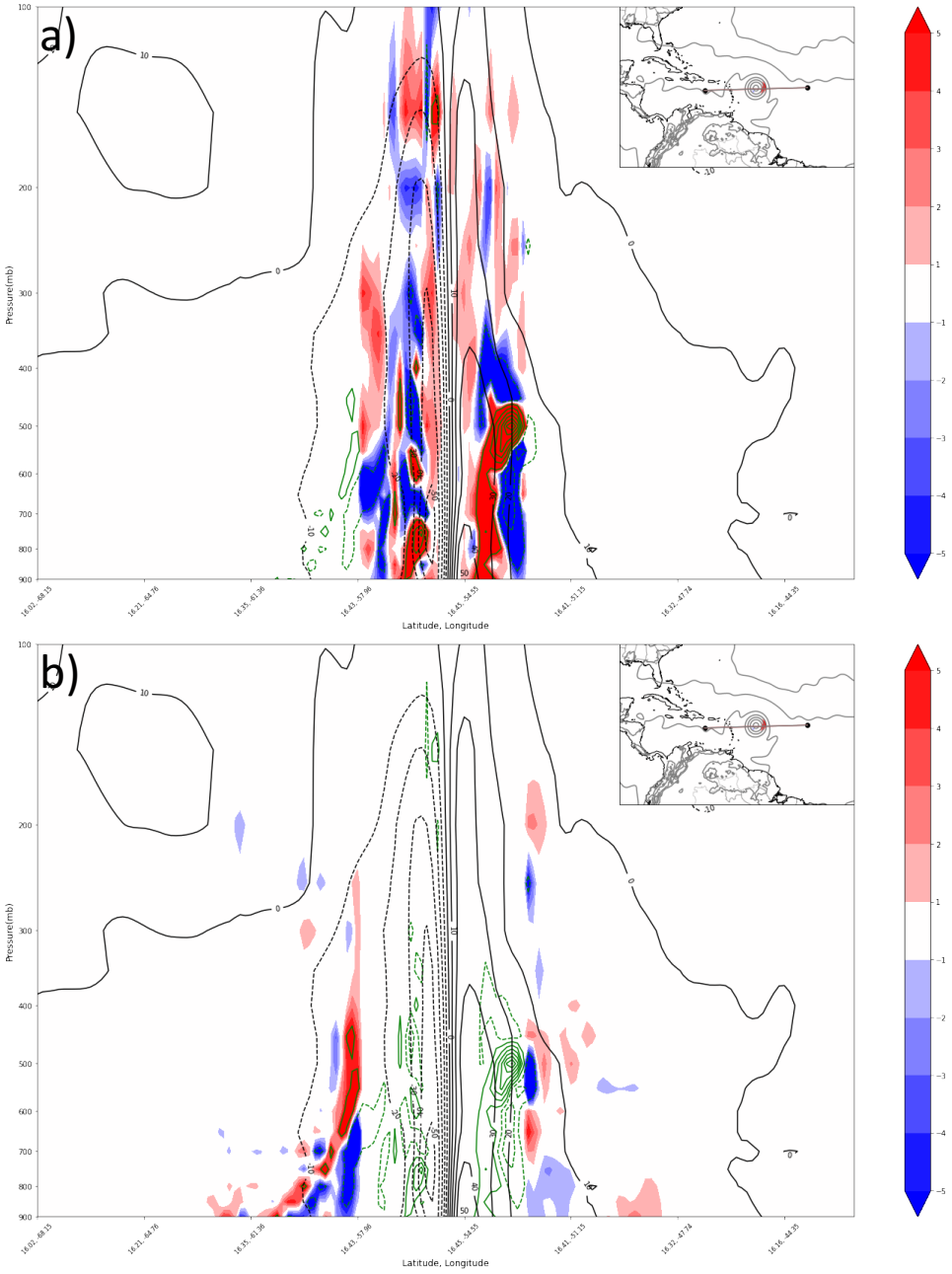

FIGURE 5.2: Same as Fig 5.1 except panel a) EXP2a and b)EXP2b

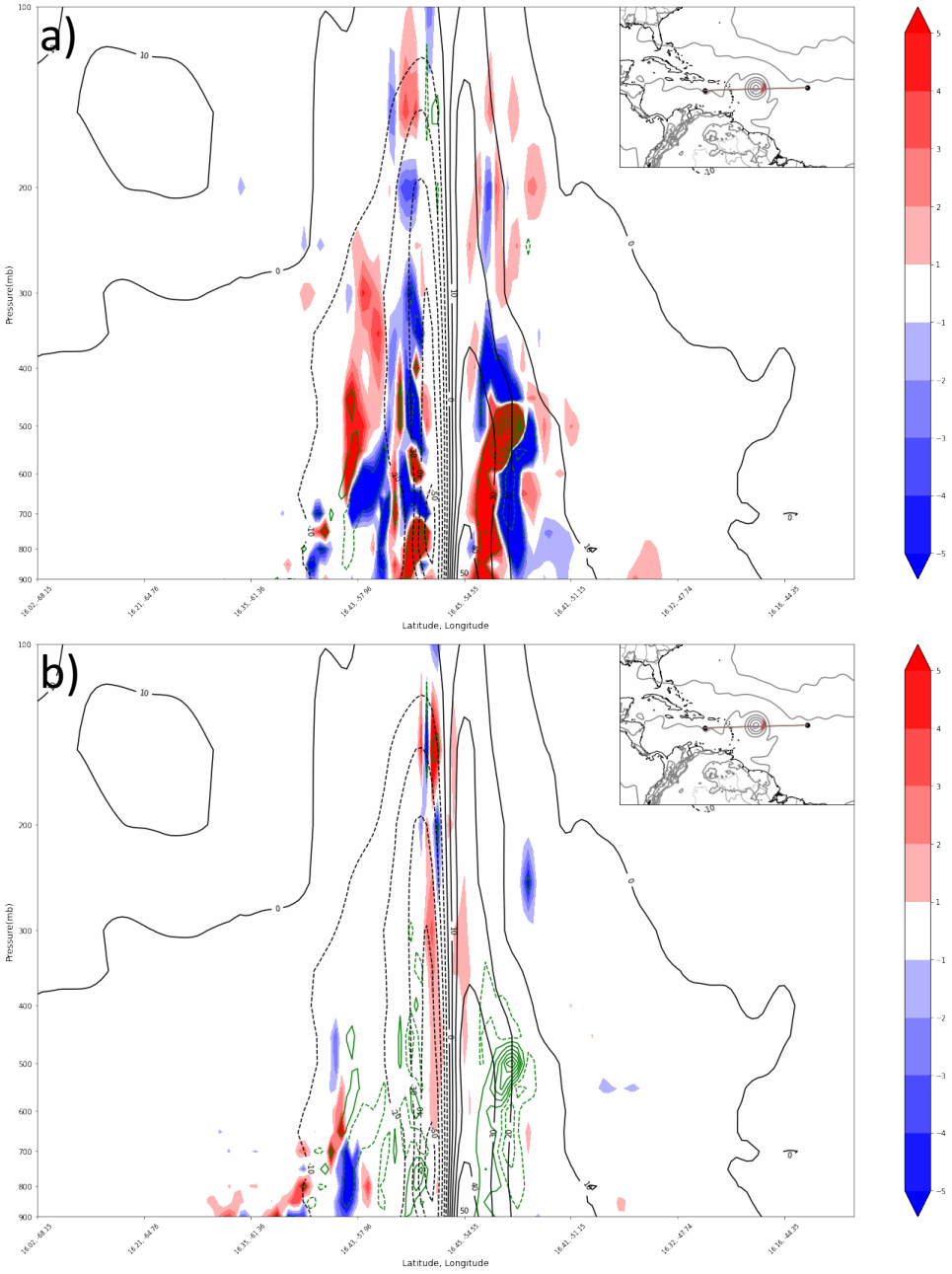

FIGURE 5.3: Same as Fig 5.1 except panel a) EXP3a and b)EXP3b

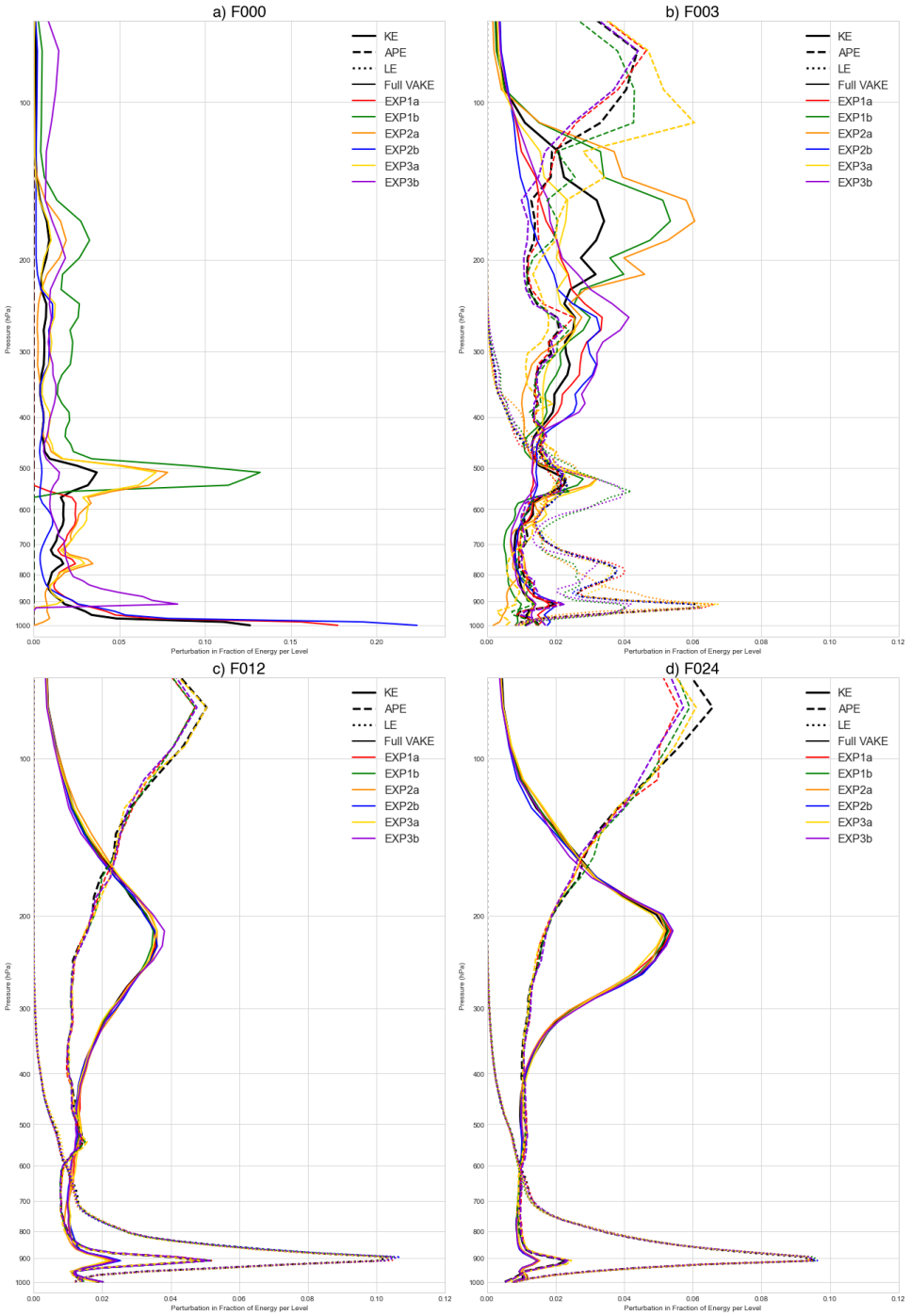

FIGURE 5.4: Perturbation of the kinetic energy (KE; solid), available potential energy (APE; dashed), and latent heat energy (LE; dotted) normalized by the total change in their respective energy. Colors denote experiment: FPE (black), EXP1a (red), EXP1b (green), EXP2a (orange), EXP2b (blue), EXP3a (yellow), EXP3b (purple). Valid at forecast hours a) F00, b) F03, c) F12, and d) F24.

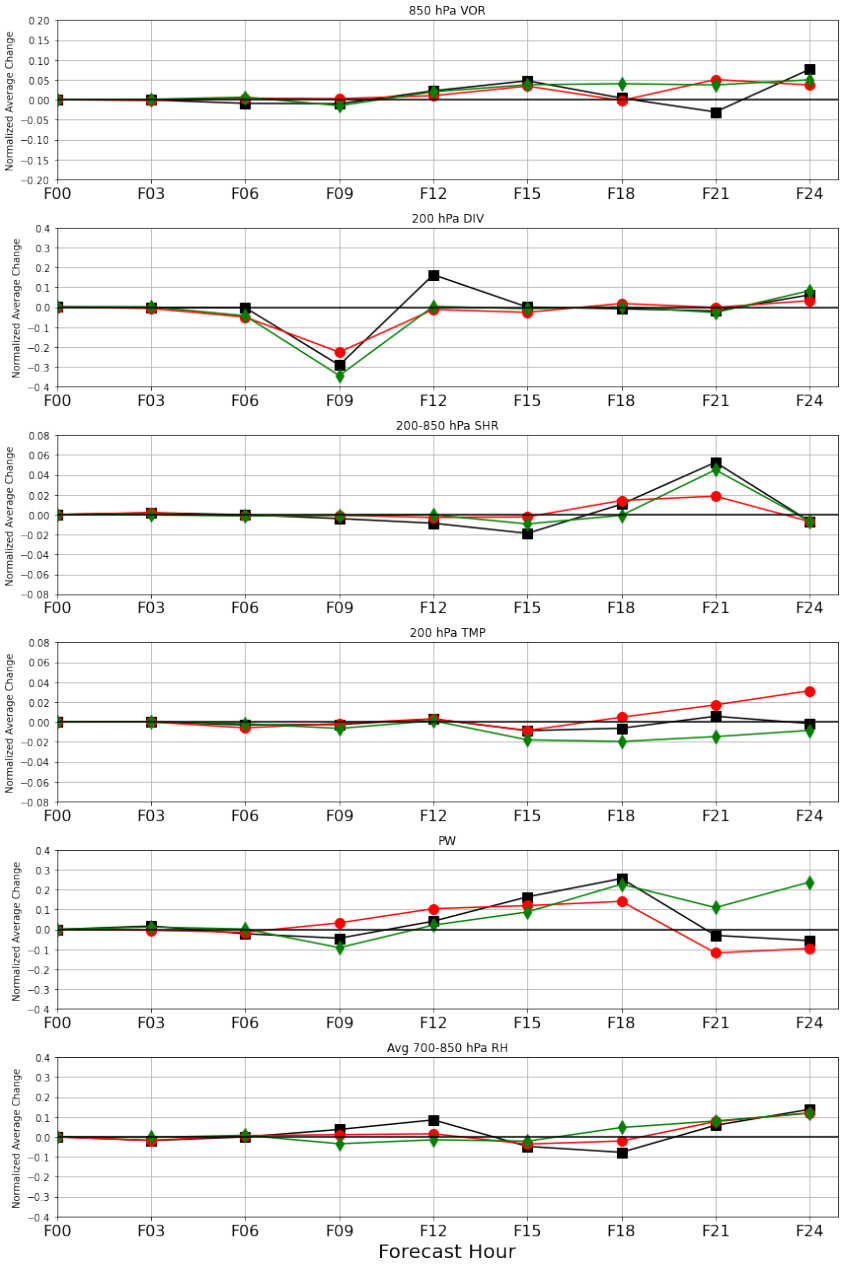

FIGURE 5.5: The normalized (difference divided by control value) storm relative averaged difference for each defined SHIPS-related variable as defined in Appendix A. All values are calculated from a radius starting at the TC center, defined as the 850 hPa maximum vorticity. Panels a) 850 hPa relative vorticity (scaled by 1), b) 200 hPa divergence (scaled by 1), c) 850 to 200 hPa vertical wind shear (scaled by 10), d) 200 hPa temperature (scaled by 1000), d) precipitable water (scaled by 100), e) 700 to 850 hPa average relative humidity (scaled by 100). The values are scaled for ease of view. Lines represent FPE (black, square marker), EXP1a (red, circle marker), and EXP1b (green, diamond marker).

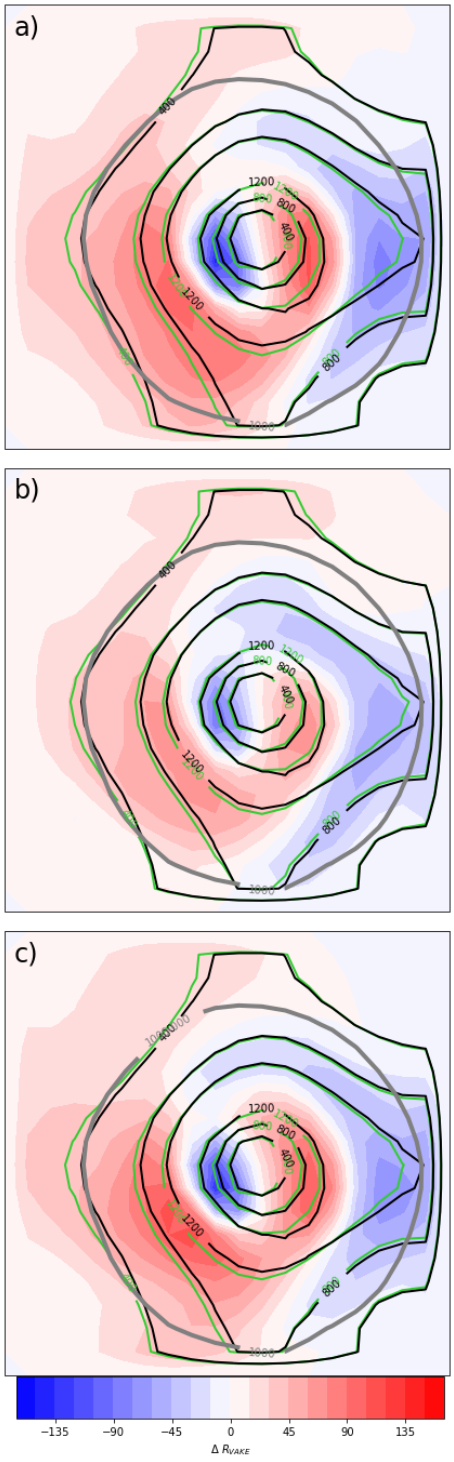

FIGURE 5.6: Valid 0000 UTC 6 September 2017 (F24) shown within horizontal response function domain and averaged from model level 6 to 10: ΔR_{VAKE} (fill; m^2s^{-2}), $VAKE_{control}$ (black contour; m^2s^{-2}), $VAKE_{perturbed}$ (green contour; m^2s^{-2}), and 1000 hPa SLP contour (gray) for reference. Panel a) FPE, b) EXP1a, and c) EXP1b.

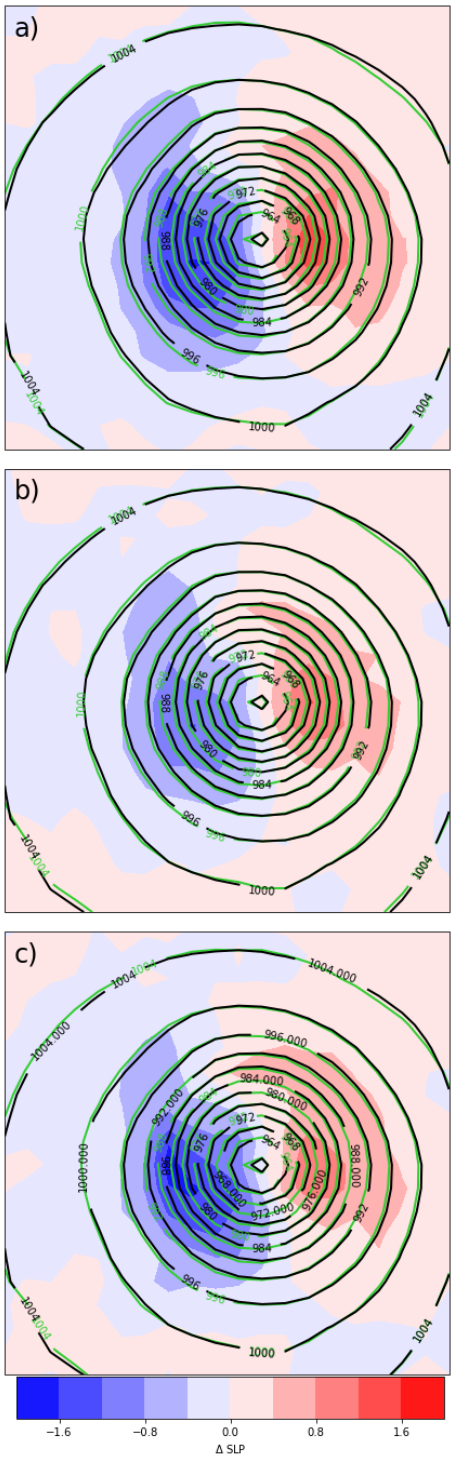

FIGURE 5.7: Valid 0000 UTC 6 September 2017 (F24) shown within horizontal response function domain: Δ SLP (fill; hPa), $\text{SLP}_{control}$ (black contour; m^2s^{-2}), and $\text{SLP}_{perturbed}$ (green contour; hPa). Panel a) FPE, b) EXP1a, and c) EXP1b.

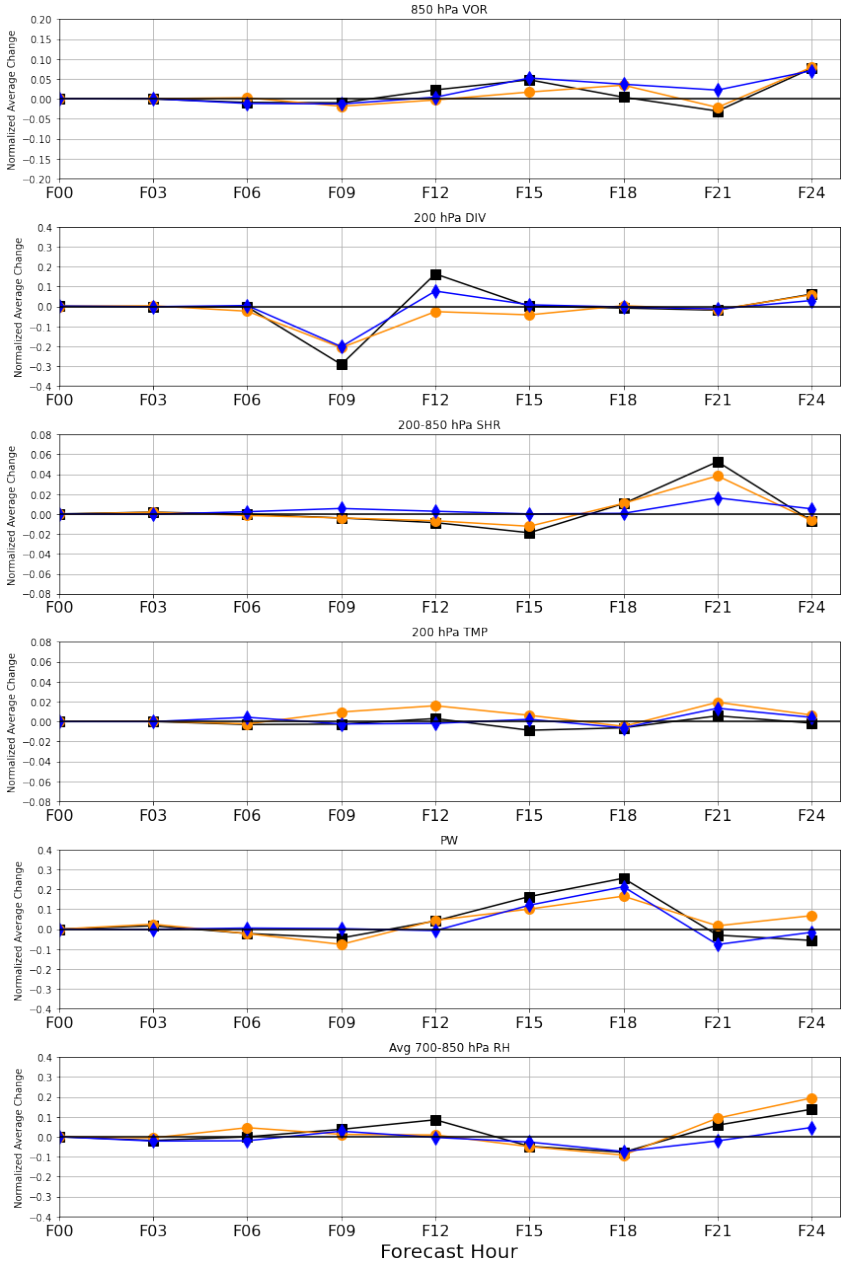

FIGURE 5.8: Same as Fig 5.5 except for experiment 2. Lines represent FPE (black, square marker), EXP2a (orange, circle marker), and EXP2b (blue, diamond marker).

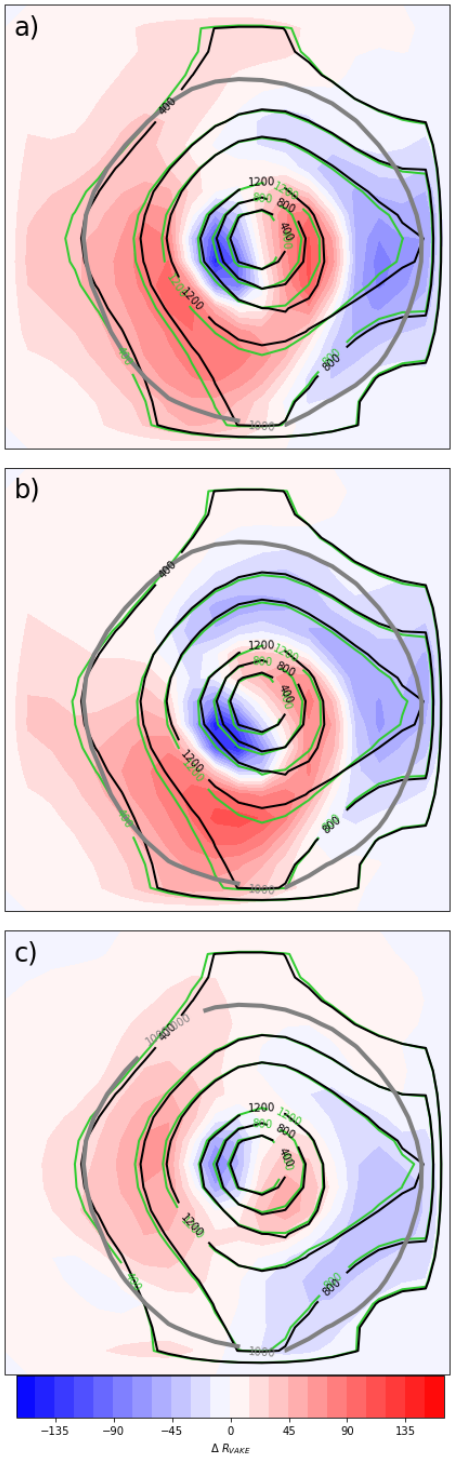

FIGURE 5.9: Same as Fig 5.6) except panel a) FPE, b) EXP2a, and c) EXP2b.

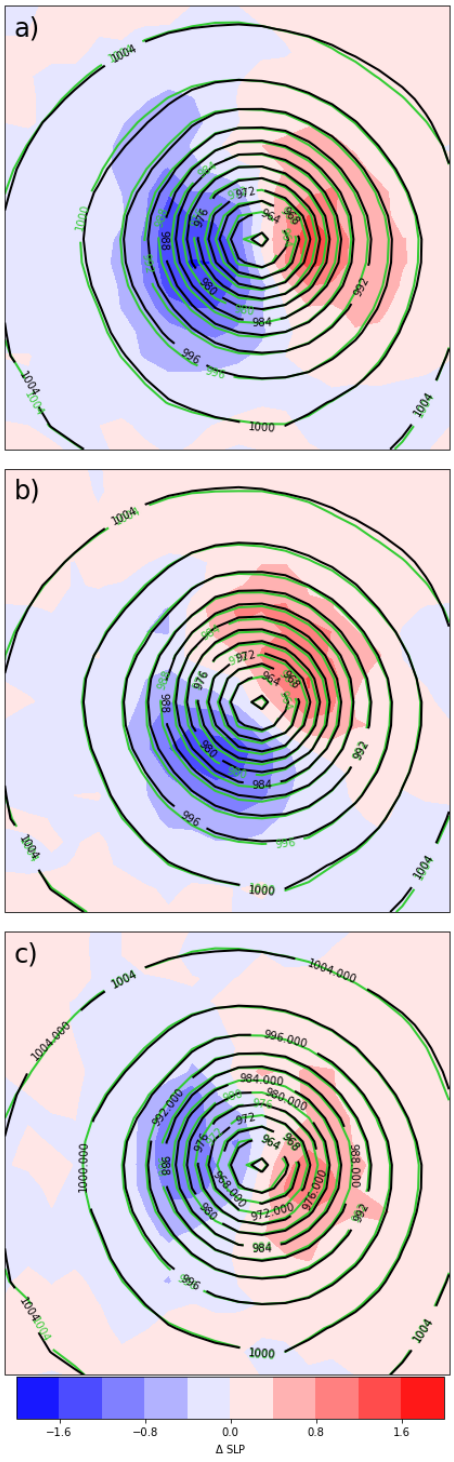

FIGURE 5.10: Same as Fig 5.7, except panel a) FPE, b) EXP2a, and c) EXP2b.

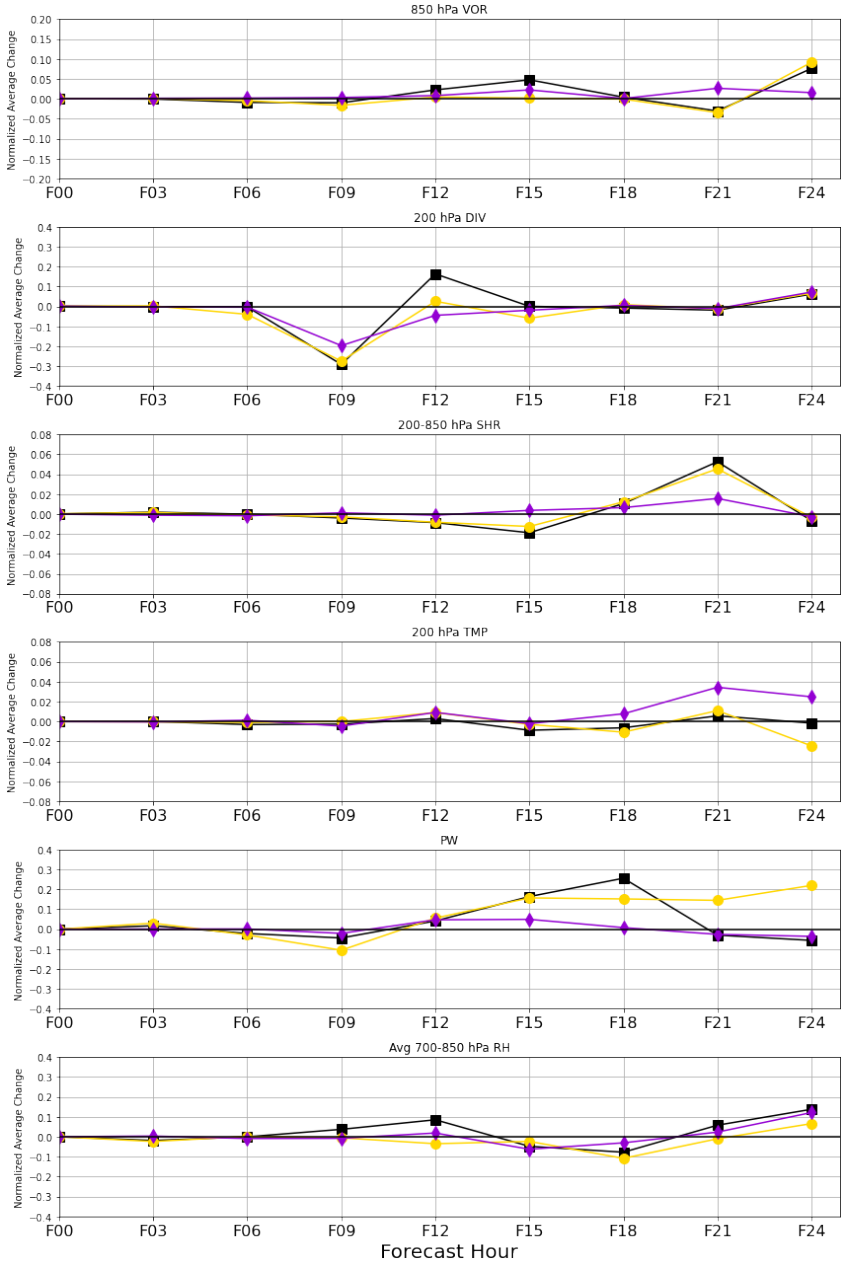

FIGURE 5.11: Same as Fig 5.5 except for experiment 3. Lines represent FPE (black, square marker), EXP3a (gold, circle marker), and EXP3b (purple, diamond marker).

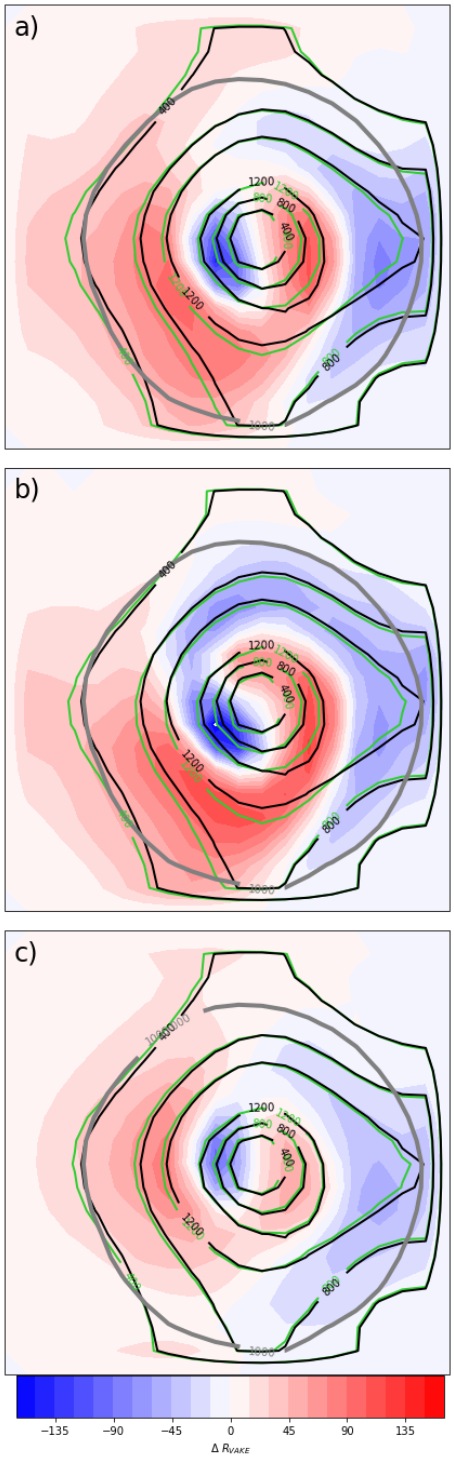

FIGURE 5.12: Same as Fig 5.6) except panel a) FPE, b) EXP2a, and c) EXP2b.

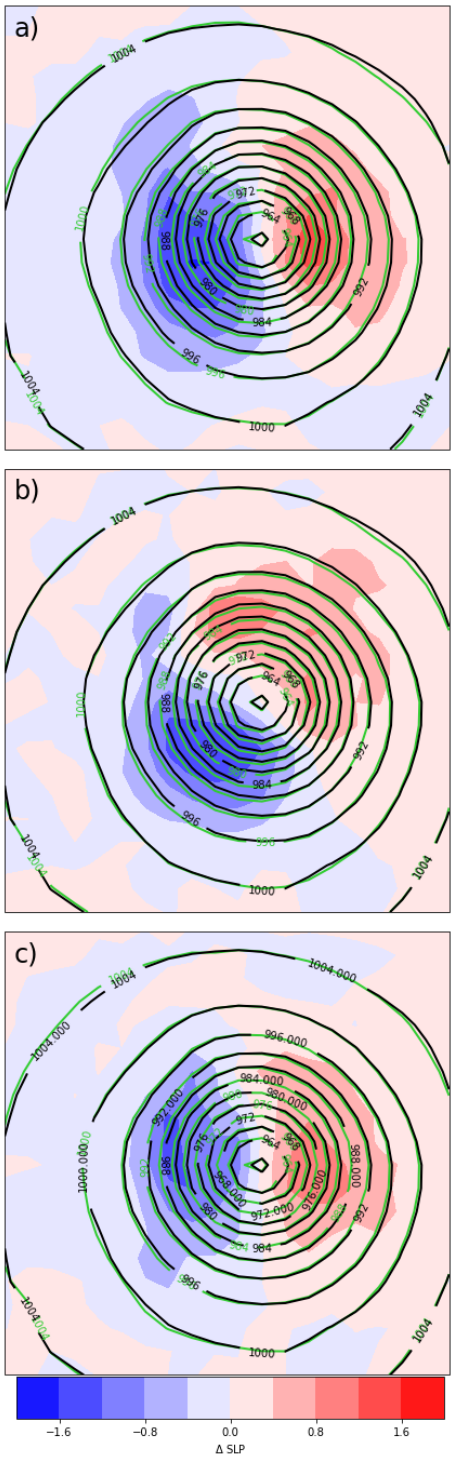

FIGURE 5.13: Same as Fig 5.7, except panel a) FPE, b) EXP3a, and c) EXP3b.

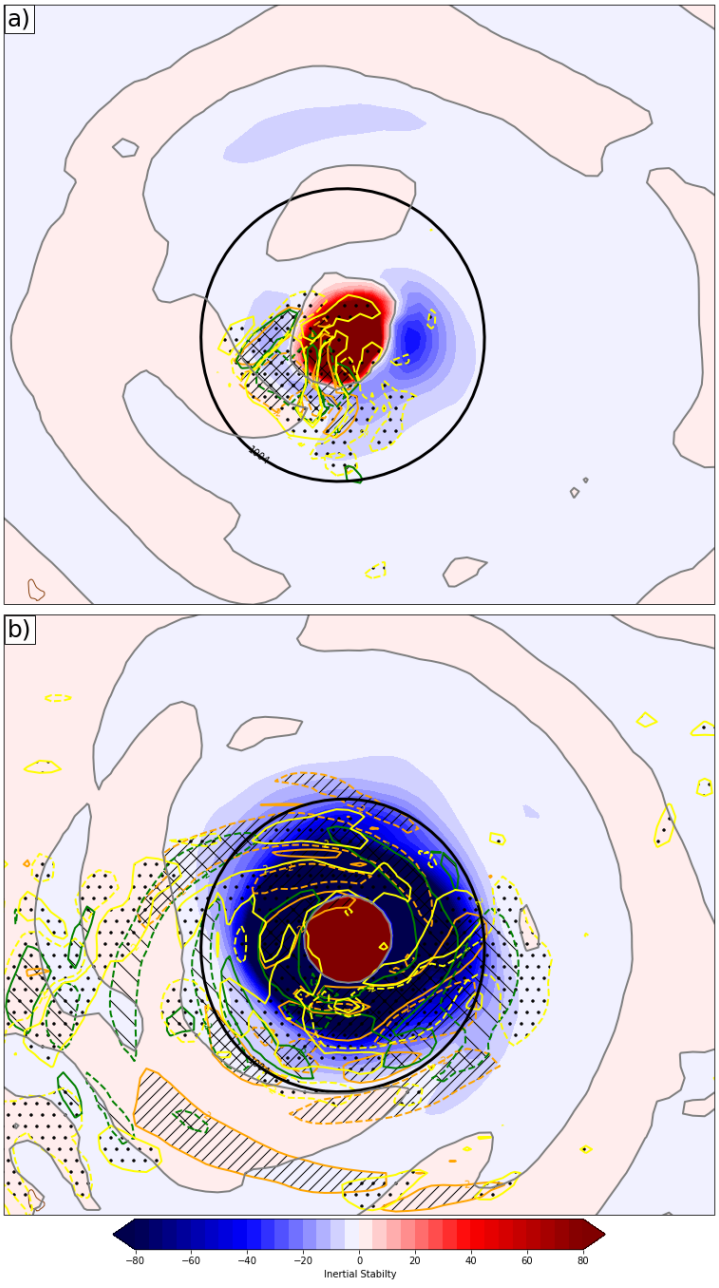

FIGURE 5.14: Valid at F00, 0000 UTC 5 September 2017. Inertial stability on a) 358 K and b) 312 K isentropic surface (fill; 5x10^{9} s^{-2}), zero line of inertial stability (grey), and the 1004 hPa sea level pressure contour (black, for spatial reference). Sensitivity to zonal wind (orange; hatched above and below 2 m^{2}s^{-2} / ms^{-1}), sensitivity to meridional wind (green; hatched above and below 2 m^{2}s$_{-2}$ / ms^{-1}), and sensitivity to potential temperature (yellow; dotted hatched above and below 2 m^{2}s^{-2} / K)

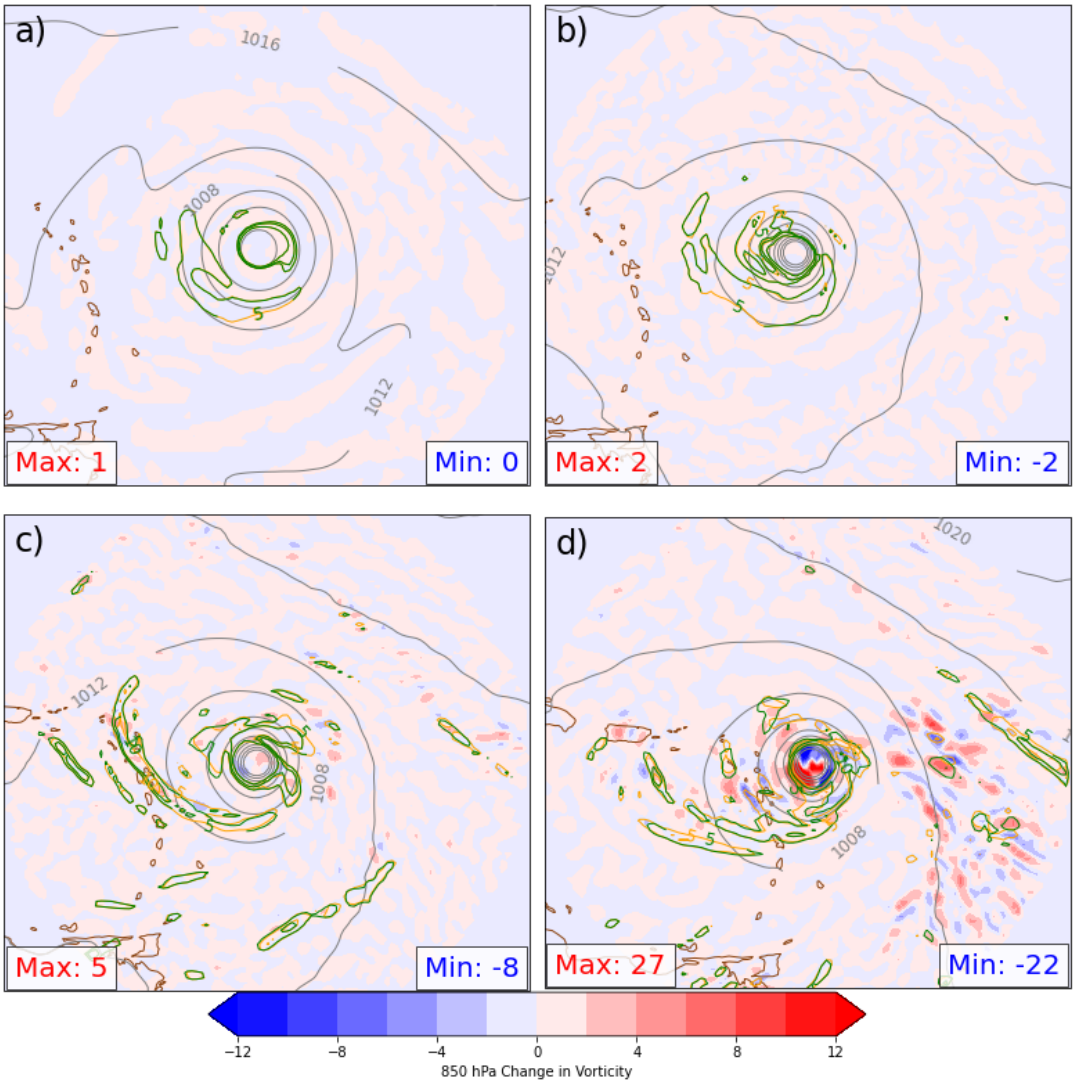

FIGURE 5.15: Perturbation 850 hPa vorticity (fill; s^{-1}), control positive relative vorticity (solid green scale by 1e5 every 5 s^{-1}), perturbed positive relative vorticity (solid orange scale by 1e5 every 5 s^{-1} below 15), SLP (solid gray every 4 hPa above 980 hPa). Valid at F00, F03, F12, and F24.

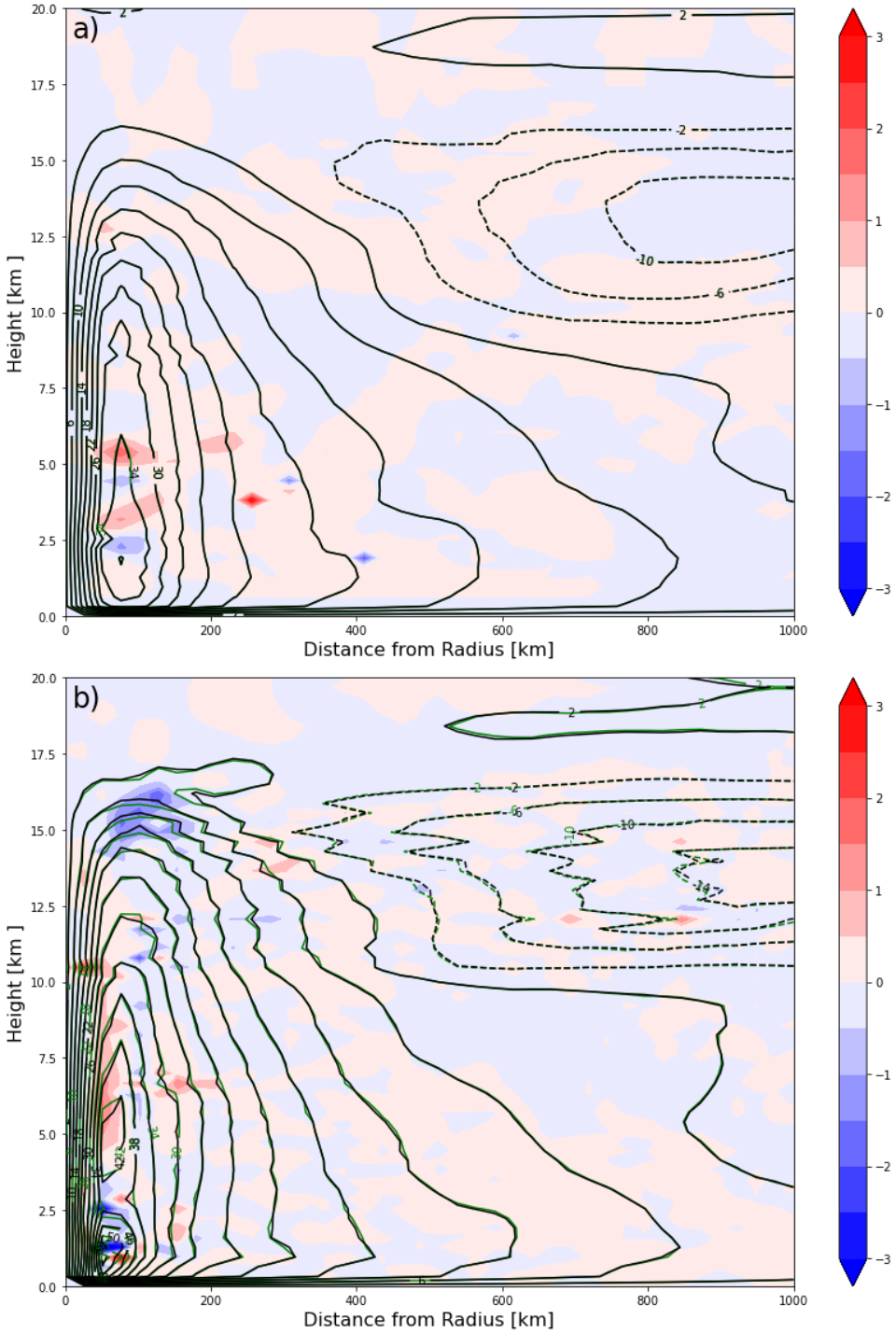

FIGURE 5.16: Azimuthally averaged from TC center to 1000 km for EXP3a: storm center relative difference azimuthal wind (fill; kts), control azimuthal wind (black contour every 4 kts) and perturbed azimuthal wind (green contour every 4 kts). Valid at a) F00 and b) F24.

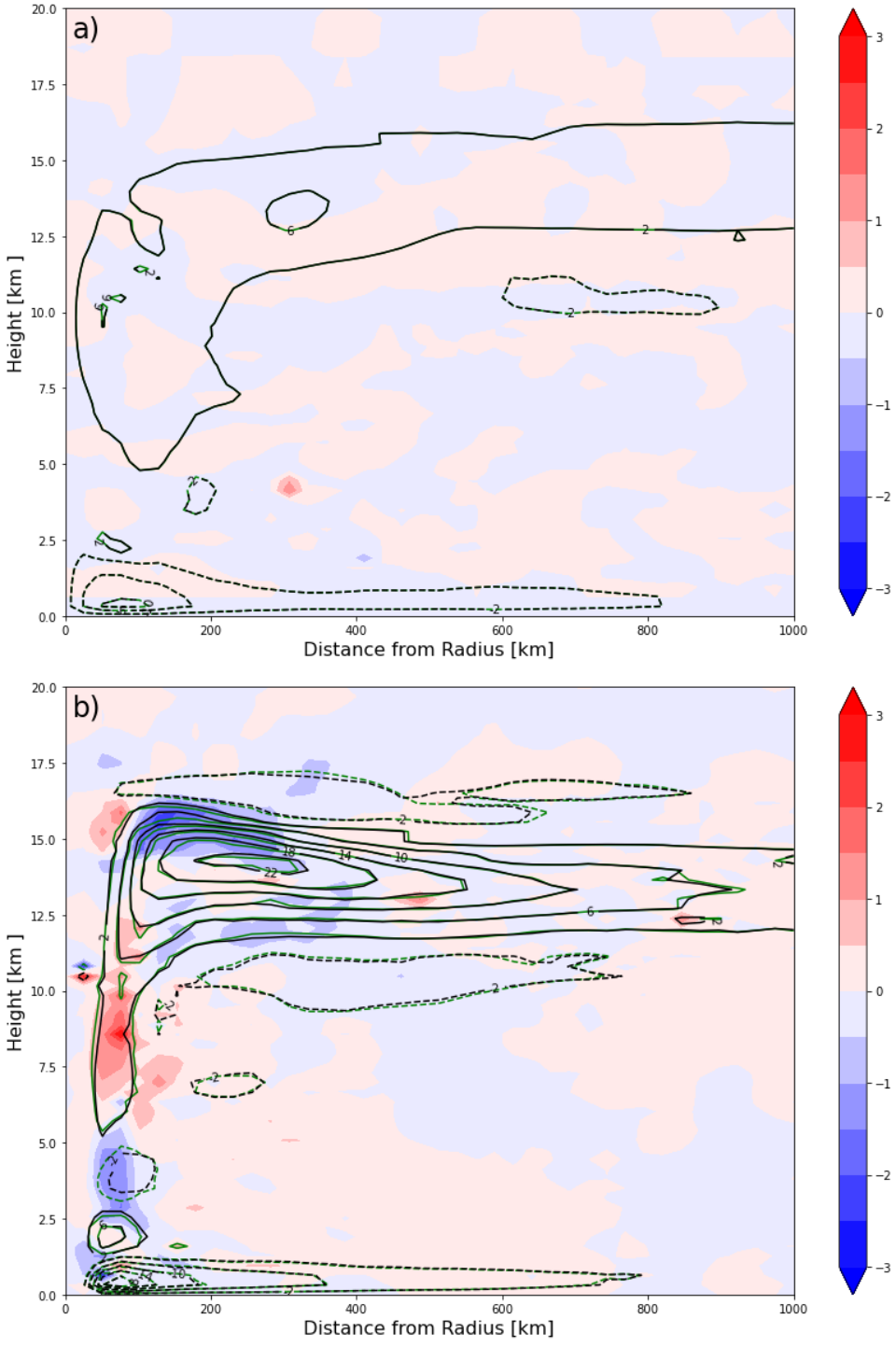

FIGURE 5.17: Azimuthally averaged from TC center to 1000 km for EXP3a: storm center relative difference radial wind (fill; kts), control radial wind (black contour every 4 kts), and perturbed radial wind (green contour every 4 kts). Valid at a) F00 and b) F24.

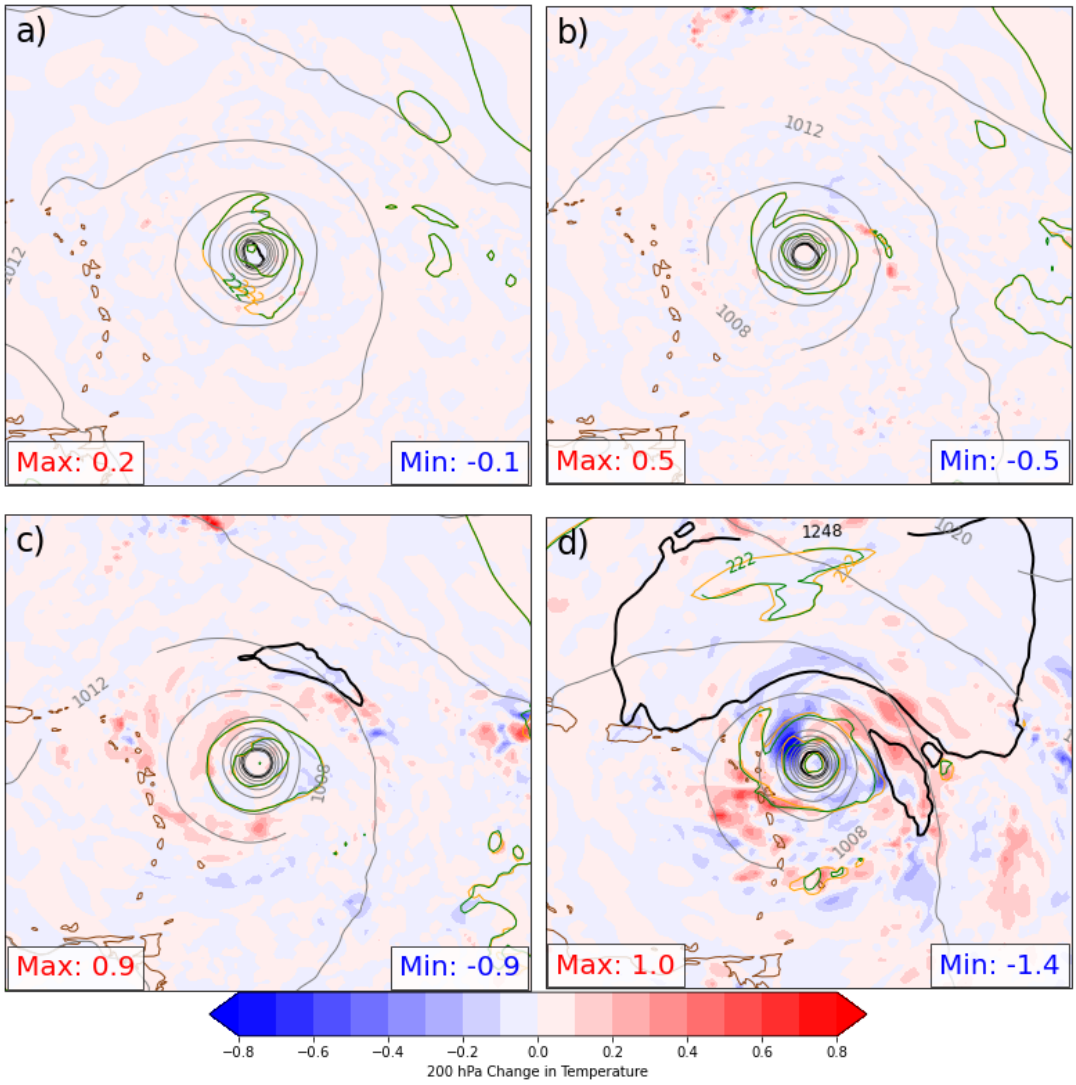

FIGURE 5.18: Perturbation 200 hPa temperature within 1000 km of TC center (fill; K), control temperature (solid orange; K), perturbed temperature (solid green; K), geopotential height (black every 8 dm) and SLP (solid gray every 4 hPa above 980 hPa). Valid at a) F03, b) F06, c) F12 and d) F24.

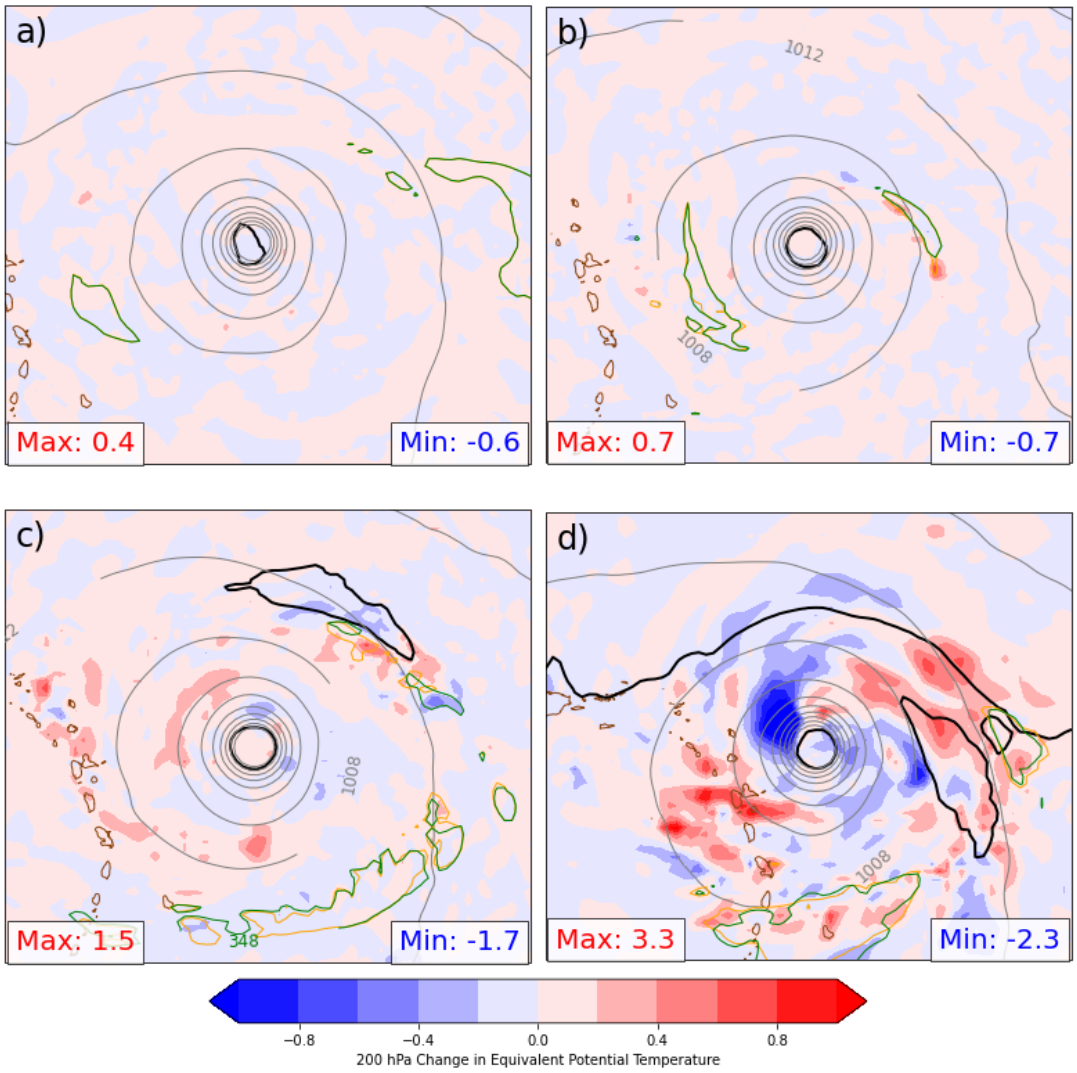

FIGURE 5.19: Same as Fig 5.18 except 200 hPa equivalent potential temperature.

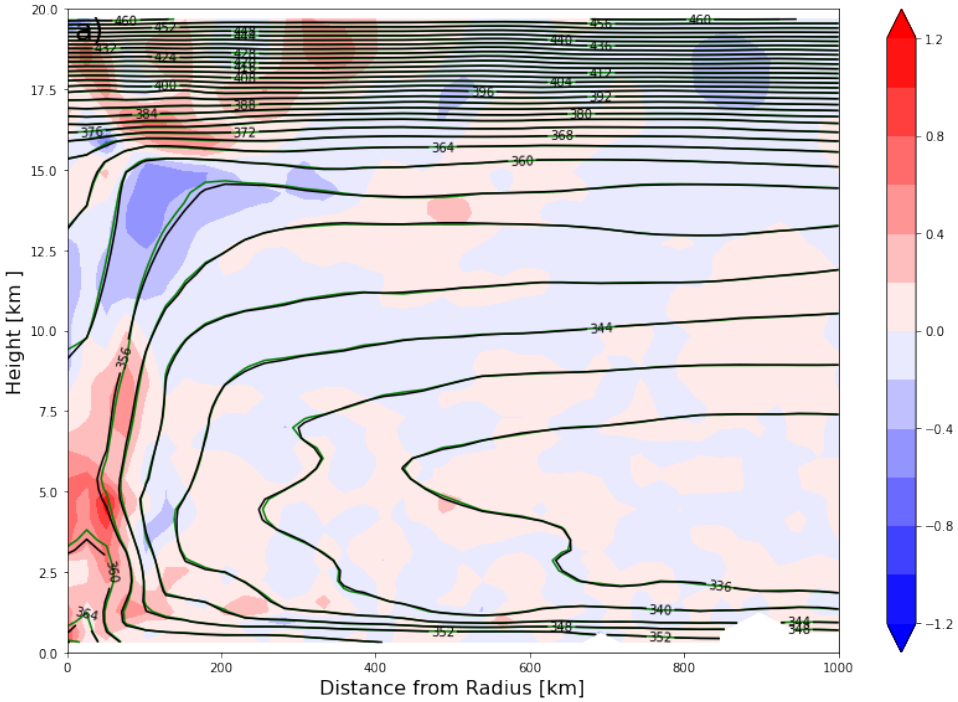

FIGURE 5.20: Azimuthally averaged from TC center to 1000 km for EXP3a: storm center relative difference equivalent potential temperature (fill; K), control equivalent potential temperature (black contour every 4 K), and perturbed equivalent potential temperature (green contour every 4 K). Valid at a) F24.

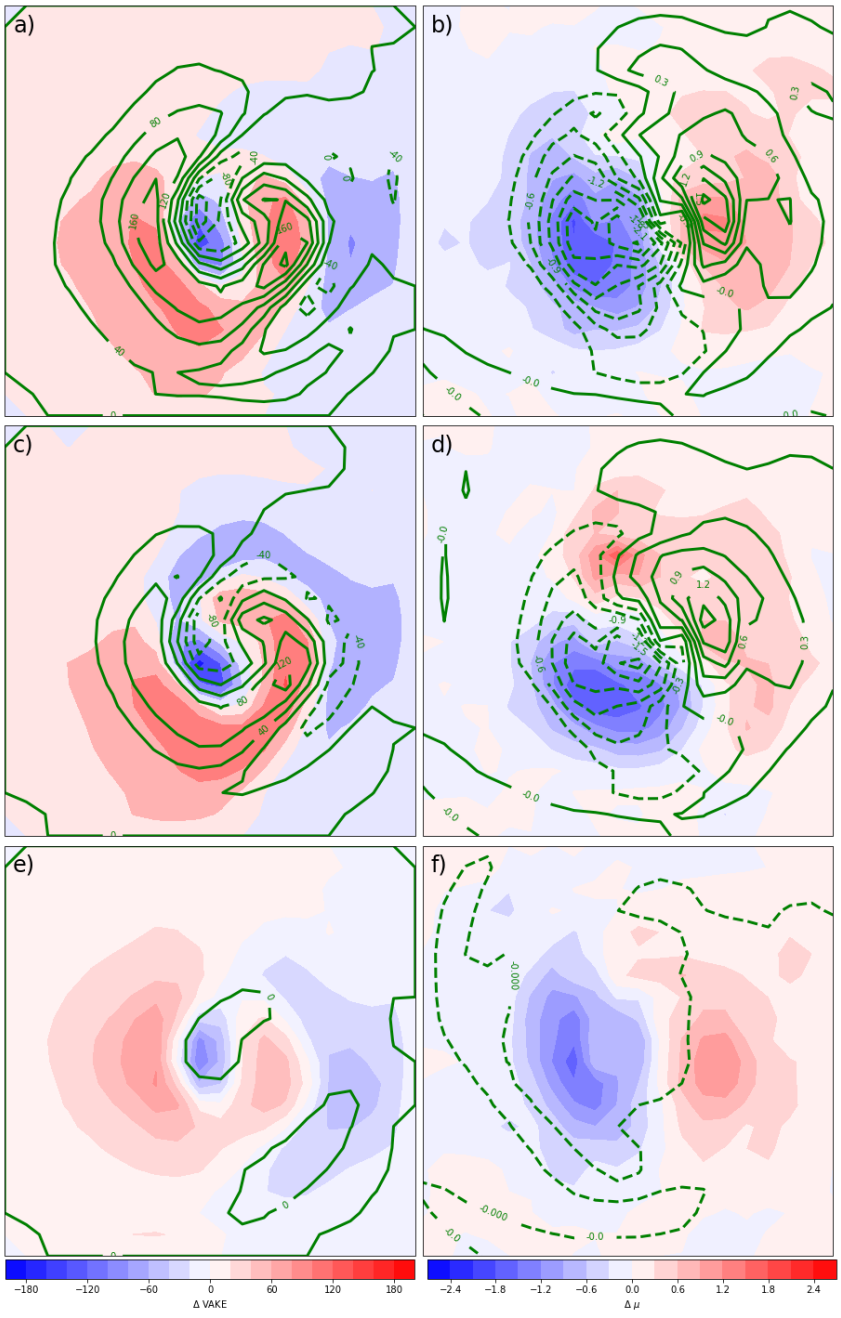

FIGURE 5.21: Valid F24, 0000 UTC 6 September 2017: a) FPE nonlinear model ΔR_{VAKE} (fill; m^2s^{-2}); tangent linear ΔR_{VAKE} (green contoured at same interval as fill), b) FPE nonlinear model $\Delta\mu$ (fill; hPa); tangent linear $\Delta\mu$ (green contoured at same interval as fill), panel c) and d) same as a and b, respectively, except EXP3a, and panel e) and f) same as a and b, respectively, except EXP3b

Chapter 6

Conclusions and Future Directions

6.1 Conclusions

The accurate and timely forecast of tropical cyclone intensity change is an area of active research. Numerous factors contribute to whether an NWP forecast can accurately capture observed tropical cyclone intensity and intensity change, including model resolution, model initial and boundary conditions, and model physics and parameterizations. Adjoint sensitivity studies are an effective means to reveal how model initial conditions influence the TC intensity as the sensitivity gradients provide dynamic and thermodynamic information that can lead to new insights if interpreted correctly. Constrained by the tangent linear assumption and simplified representations of moist processes, adjoint models can be used for case studies of short duration and modest resolutions. Provided

research questions are properly considered, the adjoint model is an effective tool for diagnosing processes impacting TC intensity change. While an initial stated goal of this work was to evaluate the sensitivities of rapidly intensifying TCs using an adjoint study framework, the emphasis and many of the new insights gained contribute more toward understanding the adjoint model as a tool than toward the physical processes contributing to intensification. This study does provide a firm foundation of additional investigations into the physical processes leading to TC intensity change.

Established literature contains a limited number of examples of adjoint sensitivity analysis applied to TC intensity (e.g., Chu et al. 2011; Ito et al. 2011; Doyle et al. 2012). Throughout the previous chapters, a framework was developed that aligned with previous studies, particularly implementing a traditional surface pressure response function to evaluate how adjoint sensitivity gradients project onto initial conditions in a case study of Hurricane Florence (2018). Consistent with previous studies, sensitivities were greatest in the lower troposphere and in the near proximity of the TC, but outside of the cyclone center. Additionally, consistent with Doyle et al. (2012), sensitivities were greatest for potential temperature, however, moisture had less of an importance than wind fields. This could be attributed to the life cycle of the TC, as Doyle et al. (2012) was analyzing TC genesis, when moisture is a larger constraining factor than after a well defined vortex is present. Additional differences in the magnitude of moisture sensitivities are likely associated with the sophistication of the adjoint model and the linearization methods for moisture parameterizations, as the WRF adjoint model only has a simple cumulus scheme and large-condensation scheme to parameterize moisture. As optimal perturbations to

initial conditions were made throughout the model atmosphere, the evolution showed a growth upward that resulted in the largest changes in perturbation KE and APE in the upper troposphere and lower stratosphere, consistent with previous studies of both tropical and extratropical cyclones (e.g., Doyle et al. 2012 Goldstein 2018; Doyle et al. 2019).

The growth of perturbations upward motivated the partitioning of the atmosphere into upper and lower tropospheric parts to evaluate whether, from the same prescribed change, the upper and lower tropospheric perturbations could intensify the TC. Upper tropospheric perturbations alone evolved to develop a more robust TC outflow earlier. The enhanced outflow layer anticyclone and radial outflow help evacuate mass from the low-level vortex. Viewed from a vorticity perspective, this better developed outflow supports lower-tropospheric vortex stretching thereby enhancing the spin-up of the low-level vortex, resulting in a stronger TC and nearly exact linearity ratio (LR). In contrast, lower tropospheric perturbations resulted in little change in the TC intensity and thus a poor LR. In addition to the nonlinear model resulting in a more robust TC in the upper tropospheric perturbation experiment, the tangent linear model evolved more extreme maximum and minimum in the response function (though still the same average change in response function). All experiments in the tangent linear model that used the response function $-\mu$ resulted in a shift in location in a nearly opposite direction of the nonlinear model shift. This emphasizes the careful consideration when defining a response function to include aspects of whether the response function incorporates any structure, which the response function $-\mu$ does not.

Additional partitions to the atmosphere were evaluated in a case study of Hurricane Irma (2017). Sets of partitioned experiments included: (1) vertical level, (2) proximity to the TC core, and (3) inertial stability. In this set of experiments, perturbations were not rescaled, such that the combination of each partition combined to the full perturbation simulation. Trends were found between experiments. One grouping of experiment subsets include perturbing only the upper troposphere (EXP1b), perturbing within the 1008 hPa contour (which corresponds to largest lateral gradients in the low-level cyclonic vortex) (EXP2a), and inertially unstable regions (EXP3a). All three experiments had the largest change at F00, around 400 hPa and a notable growth upward in perturbed KE by F03, particularly between EXP1b and EXP3a. These experiments also resulted in the highest LR and a similar shift and broadening oriented south and west of the control simulation. The experiments that resulted in low linearity (EXP1a, EXP2b, and EXP3b), at F00 all had initial perturbation amplitude concentrated in the lower troposphere, near the surface. Furthermore, the F24 change in response function and SLP was shifted westward relative to the control simulation.

There are numerous possible definitions of TC intensity possible for an adjoint response function. This definition influences the physical processes and structure that lead to changes in intensity. Three response functions were evaluated minus the perturbation dry air in a column (a proxy for surface pressure), kinetic energy (KE), and the TC vortex associated kinetic energy (VAKE). The VAKE response function is a novel approach to defining TC intensity in an adjoint study and was designed to elicit the specific response of increasing the kinetic energy of the winds associated with the vorticity of the TC.

Comparing the adjoint sensitivity gradients from each response function, the VAKE response function resulted in smaller amplitude high frequency waves that are associated with the adjoint adjustment process (Morgan, 2018) and boundary conditions. These high frequency waves diminished most rapidly for the VAKE response function as well, compared to the KE and surface pressure response functions. The wave patterns found in this study are consistent with known issues in adjoint studies, particularly when using a pressure response function (Errico and Vukicevic 1992; Morgan 2018). A benefit to using VAKE as a response function is the structural guidance it contains for how perturbations should evolved within the response function domain (e.g., superposition principle), which results in the tangent linear and nonlinear perturbations being co-located. Both traditional response functions, KE and surface pressure do not specify how the change in the nonlinear or tangent linear perturbations evolve. This can lead to changes in the response function that do not correspond to the metric intended to be evaluated as shown using the KE response function. The VAKE response function also performed more optimally, particularly compared to the KE response function to retain a higher LR as well as intensify the TC across other metrics such as low-level kinetic energy, vorticity, SLP, and latent heat release at the surface. The surface pressure also does well to intensify the TC across multiple metrics but has a slightly lower LR compared to the VAKE response function. Additionally, the orientation of the evolved perturbations is nearly reversed between the tangent linear and nonlinear model simulations for the surface pressure response function.

The scope of the outlined research discussed two case studies, evaluating multiple perturbed simulations to each case based on different definitions of response function and

where optimal perturbations were made. Further investigation and application of the newly developed response function VAKE is necessary to continue to contextualize the relationship between VAKE and other intensity metrics. Additionally, a deeper analysis of the physical mechanisms driving development in the case studies is necessary to further understand why certain regions of perturbations result in higher linearity ratios and the dynamic and thermodynamic processes that create that evolution. The next section will outline potential next steps.

6.2 Future Directions

Tropical cyclone outflow as response function

Tropical cyclone intensity is most commonly defined through (near) surface based metrics, as was done in this study. As seen in perturbed experiments, perturbations designed to increase the response function defined near the surface increase the upper-tropospheric outflow as well. Within the context of an adjoint study, a response function intended to define the strength of the outflow, which could be used to define optimal perturbations to increase the strength of the outflow could provide insights to whether outflow is driving surface development. Similar to typical surface based metrics for intensity, the construction of a response function measuring the strength of the outflow must carefully address some considerations such as the typical asymmetric aspects of more outflow fields and the impact of a shift in location, both horizontally and vertically. Also, depending the phase of development, whether an eye(-like) feature has developed must be accounted for as the characteristics of the eye (i.e, subsidence) may complicate the response function

definition. Potential metrics include the upper-tropospheric radial winds from the TC core or metrics for mass evacuation. Additionally, from the perspective of the Carnot cycle, the upward vertical motion within the eyewall, helping evacuate mass from the surface low could be considered as a response function. It is hypothesized that since the upper troposphere is dominated by dynamic over thermodynamic processes (unlike the surface) higher linearity could be achieved.

Quantifying Uncertainty

Adjoint sensitivity studies provide information for how the response function will be changed if the model initial state were perturbed. However, in the studies completed in this dissertation, no actual information about the uncertainties of the atmosphere are known or used. Future applications could contextualize adjoint sensitivities by weighting them by the uncertainty in the forecast. This could be completed by using analysis error covariance approximations for the analyses used to initialize the simulations. The concept proposed to quantify uncertainty can draw off of the ensemble Kalman Filter (EnKF; Hamill 2006), which uses an estimate of the flow dependent background-error covariances. By weighting adjoint sensitivities by the uncertainty of the initial state (so as to relax the penalty), practical information can be gained about the predictability of a given flow. This could be particularly useful for use in targeted observation campaigns, as if a highly sensitive region projects onto a region with very small uncertainty deploying more observations in that regions would not make practical sense. This would thereby highlight regions with a higher correlation between adjoint sensitivities and analysis uncertainties for additional sampling.

Adjoint derived ensemble

A future step with this research is the creation of an adjoint sensitivity-derived ensemble (e.g., Xu et al. 2001). As shown in this dissertation, adjoint sensitivities contain structured, synoptic-scale patterns with other small-scale, highly noisy patterns. These noisy patterns are likely due to small-scale convective features that result in sensitivities that are not rooted necessarily in physical processes. Through compositing ensemble members, it is expected that key physical mechanisms across forecasts will emerge and separate from the noise. Furthermore, an ensemble of trajectories can be used to create statistical information regarding the distribution of forecast variables and error variance-based measures of predictability, such as the forecast spread and error growth. Adjoint techniques allow for the evaluation of the sensitivity of a single variable (e.g., the sensitivity of intensity to the zonal wind) and evolve a perturbation of that variable alone without reference to changes in other variables. The objective would be to develop an ensemble from perturbations to combinations of adjoint sensitivities. Combinations to create an ensemble can include, but are not limited to, perturbing different subsets of model state variables, perturbing separately the upper and lower troposphere, and perturbations based on derived sensitivities. Additionally, initial perturbations can be constrained to specific geographic regions. Consistent with traditional ensemble methods, the ensemble members will have limited spread at the initial time step. As the forecast evolves, the spread of the forecasts will grow and that spread can be used to assess the predictability of the TC, including whether the forecast is more resistant to change. The partitioning completed in this dissertation support that through various partitioning of the atmosphere solutions will

diverge in their route to change the response function. With a sufficiently large ensemble, the statistical approach of using the empirical orthogonal function (EOF) analysis could be applied to elucidate the dominant structure of adjoint sensitivities.

Appendix A

SHIPS Related Variables Definitions

All values are calculated from a radius starting at the **TC center**. The **TC center** is defined as the 850 hPa maximum vorticity:

VRT 850 hPa relative vorticity (s^{-1}) from 0-1000 km radius

DIV 200 hPa divergence (s^{-1}) from 0-1000 km

SHR 850 to 200 hPa vertical wind shear (ms^{-1}) from 200-1000 km radius

TMP 200 hPa temperature (K) centered from 0-1000 km radius

PW precipitable water (m) centered from 100-200 km radius

RH 700 to 850 hPa average relative humidity (%) centered from 200-800 km radius

Bibliography

Aberson, S. D., 2003: Targeted observations to improve operational tropical cyclone track forecast guidance. *Monthly Weather Review*, **131**, 1613–1628.

Aberson, S. D. and J. L. Franklin, 1999: Impact on hurricane track and intensity forecasts of GPS dropwindsonde observations from the first-season flights of the NOAA gulfstream-IV Jet Aircraft. *Bulletin of the American Meteorological Society*, **80**, 421–427.

Ancell, B. C. and C. F. Mass, 2006: Structure, growth rates, and tangent linear accuracy of adjoint sensitivities with respect to horizontal and vertical resolution. *Monthly Weather Review*, **134**, 2971–2988.

Anthes, R. A., 1972: The development of asymmetries in a three- dimensional numerical model of tropical cyclone. *Monthly Weather Review*, **100**, 461–476.

Barrett, B. S., E. R. Sanabia, S. C. Reynolds, J. K. Stapleton, and A. L. Borrego, 2016: Evolution of the upper tropospheric outflow in Hurricanes Iselle and Julio (2014) in the

Navy Global Environmental Model (NAVGEM) analyses and in satellite and dropsonde observations. *Journal of Geophysical Research Atmospheres*, **121**, 13273–13286.

Brown, B. R. and G. J. Hakim, 2015: Sensitivity of intensifying Atlantic hurricanes to vortex structure. *Quarterly Journal of the Royal Meteorological Society*, **141**, 2538–2551.

Burpee, R. W., J. L. Franklin, S. J. Lord, R. E. Tuleya, and S. D. Aberson, 1996: The impact of Omega dropwindsondes on operational hurricane track forecast models. *Bulletin of the American Meteorological Society*, **77**, 925–933.

Cangialosi, J. P., A. Latto, and R. Berg, 2018: National Hurricane Center Tropical Cyclone Report Hurricane Irma (AL112017). *National Hurricane Center*, 1–111.

Chan, J. C., 2005: The physics of tropical cyclone motion. *Annual Review of Fluid Mechanics*, **37**, 99–128.

Chang, E. K. M., M. Zheng, and K. Raeder, 2013: Medium-range ensemble sensitivity analysis of two extreme Pacific extratropical cyclones. *Monthly Weather Review*, **141**, 211–231.

Chavas, D. R., K. A. Reed, and J. A. Knaff, 2017: Physical understanding of the tropical cyclone wind-pressure relationship. *Nature Communications*, **8**.

Chu, K., Q. Xiao, Z. M. Tan, and J. Gu, 2011: A forecast sensitivity study on the intensity change of Typhoon Sinlaku (2008). *Journal of Geophysical Research Atmospheres*, **116**, 1–13.

DeMaria, M., 2014: Is tropical cyclone intensity guidance improving? *Bulletin of the American Meteorological Society*, **95**, 387–398.

Demaria, M., J. L. Franklin, M. J. Onderlinde, and J. Kaplan, 2021: Operational Forecasting of Tropical Cyclone Rapid Intensification at the National Hurricane Center. *Atmosphere*, **12**, 683.

DeMaria, M. and J. Kaplan, 1994: A Statistical Hurricane Intensity Prediction Scheme (SHIPS) for the Atlantic Basin. *Weather and Forecasting*, **9**, 209–220.

— 1999: An updated statistical hurricane intensity prediction scheme for the Atlantic and eastern North Pacific basins. *Weather and Forecasting*, **14**, 326–337.

Doyle, J. D., C. A. Reynolds, and C. Amerault, 2011: Diagnosing tropical cyclone sensitivity. *Computing in Science and Enginering*, **13**, 31–39.

— 2019: Adjoint sensitivity analysis of high-impact extratropical cyclones. *Monthly Weather Review*, **147**, 4511–4532.

Doyle, J. D., C. A. Reynolds, C. Amerault, and J. R. Moskaitis, 2012: Adjoint sensitivity and predictability of tropical cyclogenesis. *Journal of the Atmospheric Sciences*, **69**, 3535–3557.

Doyle, J. D., C. A. Reynolds, and P. A. Reinecke, 2014: Initial condition sensitivity and predictability of a severe extratropical cyclone using a moist adjoint. *Monthly Weather Review*, **142**, 320–342.

Ehrendorfer, M., R. M. Errico, and K. D. Raeder, 1999: Singular-vector perturbation growth in a primitive equation model with moist physics. *Journal of the Atmospheric Sciences*, **56**, 1627–1648.

Emanuel, K., 1999: Thermodynamic control of hurricane intensity. *Nature*, **401**, 665–669.

— 2017: Will global warming make hurricane forecasting more difficult? *Bulletin of the American Meteorological Society*, **98**, 495–501.

Emanuel, K. A., 1986: An Air-Sea Interaction Theory for Tropical Cyclones. Part I: Steady State Maintenance. *Journal of the Atmospheric Sciences*, **43**, 585–604.

— 1988: The Maximum Intensity of Hurricanes. *Jounral of the Atmospheric Sciences*, **45**, 1143–1155.

Errico, R. M., 1997: What Is an Adjoint Model? *Bulletin of the American Meteorological Society*, **78**, 2577–2591.

Errico, R. M. and T. Vukicevic, 1992: Sensitivity Analysis Using an Adjoint of the PSU-NCAR Mesoseale Model. *Monthly Weather Review*, **120**, 1644–1660.

Gall, R., J. Franklin, F. Marks, E. N. Rappaport, and F. Toepfer, 2013: The hurricane forecast improvement project. *Bulletin of the American Meteorological Soceity*, **94**, 329–343.

Goldstein, A., 2018: *A methodology for modulating the intensification rates of forecast midlatitude cyclones with implications for predictability*. Ph.D. thesis, Univeristy of

Wisconsin - Madison.

URL https://aos.wisc.edu/aosjournal/Volume32/Goldstein_PhD.pdf

Gombos, D., R. N. Hoffman, and J. A. Hansen, 2012: Ensemble statistics for diagnosing dynamics: Tropical cyclone track forecast sensitivities revealed by ensemble regression. *Monthly Weather Review*, **140**, 2647–2669.

Gray, M. W., 1968: Global view of the origin of tropical disturbances and storms. *Monthly Weather Review*, **96**, 669–700.

Hakim, G. J. and R. D. Torn, 2008: Ensemble synoptic analysis. *Synoptic-Dynamic Meteorology and Weather Analysis and Forecasting: A Tribute to Fred Sanders,*, American Meteorological Society, 147–162.

Hamill, T. M., 2006: Ensemble-based atmospheric data assimilation. *Predictability of Weather and Climate*, T. N. Palmer and R. Hagedorn, Eds., Cambridge Press, 124–156.

Hart, R. and L. Cowan, 2018: The Potentially Deleterious Impact of Choice of Sea-Level Pressure Calculation in the GFS Model When Determining Cyclone Intensity and Track. *33rd Conference on Hurricanes and Tropical Meteorology*.

URL https://ams.confex.com/ams/33HURRICANE/webprogram/Paper340155.html

He, Z., 2018: *Development and application of adjoint tools for the WRF model: a case study of Hurricane Irma (2017)*. Ph.D. thesis, University of Wisconsin - Madison.

Holiday, C. R. and A. H. Thompson, 1979: Climatological characteristics of rapidly intensifying typhoons. *Monthly Weather Review*, **107**, 1022–1034.

Holland, G. J. and R. T. Merrill, 1984: On the dynamics of tropical cyclone structural changes. *Quarterly Journal of the Royal Meteorological Society*, **110**, 723–745.

Hoover, B. T., 2015: Identifying a barotropic growth mechanism in east pacific tropical cyclogenesis using adjoint-derived sensitivity gradients. *Journal of the Atmospheric Sciences*, **72**, 1215–1234.

Hoover, B. T. and M. C. Morgan, 2010: Validation of a tropical cyclone steering response function with a barotropic adjoint model. *Journal of the Atmospheric Sciences*, **67**, 1806–1816.

— 2011: Dynamical sensitivity analysis of tropical cyclone steering using an adjoint model. *Monthly Weather Review*, **139**, 2761–2775.

Hoover, B. T. and C. S. Velden, 2020: Adjoint-Derived Impact of Assimilated Observations on Tropical Cyclone Intensity Forecasts of Hurricane Joaquin (2015) and Hurricane Matthew (2016). *Journal of Atmospheric and Oceanic Technology*, **37**, 1333–1352.

Houze, R. A., 2010: Clouds in tropical cyclones. *Monthly Weather Review*, **138**, 293–344.

Ito, K., Y. Ishikawa, Y. Miyamoto, and T. Awaji, 2011: Short-time-scale processes in a mature hurricane as a response to sea surface fluctuations. *Journal of the Atmospheric Sciences*, **68**, 2250–2272.

Kaplan, J. and M. DeMaria, 1995: A simple empirical model for predicting the decay of tropical cyclone winds after landfall. *Journal of Applied Meteorology*, **34**, 2499–2512.

— 2001: On the decay of tropical cyclone winds after landfall in the New England area. *Journal of Applied Meteorology*, **40**, 280–286.

— 2003: Large-scale characteristics of rapidly intensifying tropical cyclones in the North Atlantic basin. *Weather and Forecasting*, **18**, 1093–1108.

Kaplan, J., M. DeMaria, and J. A. Knaff, 2010: A Revised Tropical Cyclone Rapid Intensification Index for the Atlantic and Eastern North Pacific Basins. *Weather and Forecasting*, **25**, 220–241.

Kaplan, J., C. M. Rozoff, M. DeMaria, C. R. Sampson, J. P. Kossin, C. S. Velden, J. J. Cione, J. P. Dunion, J. A. Knaff, J. A. Zhang, J. F. Dostalek, J. D. Hawkins, T. F. Lee, and J. E. Solbrig, 2015: Evaluating environmental impacts on tropical cyclone rapid intensification predictability utilizing statistical models. *Weather and Forecasting*, **30**, 1374–1396.

Kleist, D. T. and M. C. Morgan, 2005: Interpretation of the structure and evolution of adjoint-derived forecast sensitivity gradients. *Monthly Weather Review*, **133**, 466–484.

Kurihara, Y., M. A. Bender, R. E. Tuleya, and R. J. Ross, 1998: The GFDL hurricane prediction system and its performance in the 1995 hurricane season. *Monthly Weather Review*, **126**, 1306– 1322.

Langland, R. H., R. L. Elsberry, and R. M. Errico, 1995: Evaluation of physical properties in an idealized extratropical cyclone using adjoint sensitivity. *Quarterly Journal of the Royal Meteorological Society*, **121**, 1349–1386.

Lorenz, E. N. and K. A. Emanuel, 1998: Optimal sites for supplementary weather observations: Simulation with a small model. *Jounral of the Atmospheric Sciences*, **55**, 399–414.

Majumdar, S. J., S. D. Aberson, C. H. Bishop, C. Cardinali, J. Caughey, A. Doerenbecher, P. Gauthier, R. Gelaro, T. M. Hamill, and R. H. Langland, 2011: Targeted observations for improving numerical weather prediction: an overview. *World Weather Research Programme/THORPEX Publication*, **15**, 37.

Majumdar, S. J., C. H. Bishop, B. J. Etherton, and Z. Toth, 2002: Adaptive sampling with the ensemble transform Kalman filter. Part II: Field program implementation. *Monthly Weather Review*, **130**, 1356–1369.

Marks, F. D. and Coauthors, 2019: Hurricane forecast improvement program five-year plan: 2019-2024. Proposed framework for addressing Section 104 of the Weather Research Forecasting Innovation Act of 2017. National Oceanic and Atmospheric Administration Strategic Plan.

Merrill, R. T., 1988: Environmental Influences on Hurricane Intensification. *Jounral of the Atmospheric Sciences*, **45**, 1678–1687.

Merrill, R. T. and C. S. Velden, 1996: A three-dimensional analysis of the outflow layer of Supertyphoon Flo (1990). *Monthly Weather Review*, **124**, 47–63.

Morgan, M. C., 2018: On the dynamics of adjustment in the f-plane shallow water adjoint system. *Journal of the Atmospheric Sciences*, **75**, 1571–1585.

— 2021: Sensitivity of tropical cyclone intensity to outflow layer perturbations. *34th Conference on Hurricanes and Tropical Meteorology*.

Nolan, D. S. and B. F. Farrell, 1999: Generalized stability analyses of asymmetric disturbances in one- and two-celled vortices maintained by radial inflow. *Journal of the Atmospheric Sciences*, **56**, 1282–1307.

Nolan, D. S., Y. Moon, and D. P. Stern, 2007: Tropical cyclone intensification from asymmetric convection: Energetics and efficiency. *Journal of the Atmospheric Sciences*, **64**, 3377–3405.

Onderlinde, M. and M. DeMaria, 2018: Deterministic to Probabilistic Statistical Rapid Intensification Index (DTOPS): A New Method for Forecasting RI Probability. *33rd Conference on Hurricanes and Tropical Meteorology, American Meteorlogical Society*, Ponte Vedra, FL.

Ooyama, K. V., 1969: Numerical Simulation of the life cycle of tropical cyclones. *Jounral of the Atmospheric Sciences*, **26**, 3–40.

Peng, M. S. and C. A. Reynolds, 2006: Sensitivity of tropical cyclone forecast as revealed by singular vectors. *Journal of the Atmospheric Sciences*, **63**, 2508–2528.

Petterssen, S., 1953: On the relationship between vorticity, deformation, and divergence, and the configuration of the pressure field. Tellus 5, 231-237. *Tellus*, **5**, 231–237.

Pu, Z. and E. Kalnay, 1999: Targeting observations with the quasi-linear inverse and adjoint NCEP global models. *Quarterly Journal of the Royal Meteorological Society*, **125**, 3329–3338.

Pu, Z., E. Kalnay, J. Sela, and I. Szunyogh, 1997: Sensitivity of forecast error to initial conditions with a quasi-inverse linear method. *Monthly Weather Review*, **125**, 2479–2503.

Rappaport, E. N., J. L. Franklin, L. A. Avila, S. R. Baig, J. L. Beven, E. S. Blake, C. A. Burr, J. G. Jiing, C. A. Juckins, R. D. Knabb, C. W. Landsea, M. Mainelli, M. Mayfield, C. J. McAdie, R. J. Pasch, C. Sisko, S. R. Stewart, and A. N. Tribble, 2009: Advances and challenges at the national hurricane center. *Weather and Forecasting*, **24**, 395–419.

Rappin, E. D., M. C. Morgan, and G. J. Tripoli, 2011: The impact of outflow environment on tropical cyclone intensification and structure. *Journal of the Atmospheric Sciences*, **68**, 177–194.

Ratnam, V. J. and K. K. Kumar, 2005: Sensitivity of the simulated monsoon of 1987 and 1988 to convective parameterization schemes in MM5. *Journal of Climate*, **18**, 2724–2743.

Reynolds, C. A., J. D. Doyle, and X. Hong, 2016: Examining tropical cyclone-Kelvin wave interactions using adjoint diagnostics. *Monthly Weather Review*, **144**, 4421–4439.

Sanders, F., 1992: Skill of operational models in cyclone prediction out to five days during ERICA. Wea. Forecasting, 7, 3–25. *Weather and Forecasting*, **7**, 3–25.

Skamarock, W. C. and Coauthors, 2008: A description of the advanced research WRF version 3. NCAR Tech. *Note NCAR/ TN-4751STR*, 113.

Soden, B. J., C. S. Velden, and R. E. Tuleya, 2001: The Impact of Satellite Winds on Experimental GFDL Hurricane Model Forecasts. *Monthly Weather Review*, **129**, 835–852.

Stewart, S. R. and R. Berg, 2019: National Hurricane Center tropical cyclone report: Hurricane Florence (AL062018). *National Hurricane Center*, 1–98.

Torn, R. D. and G. J. Hakim, 2008: Ensemble-based sensitivity analysis. *Monthly Weather Review*, **136**, 663–677.

Tuleya, R. E. and S. J. Lord, 1996: The impact of dropwindsonde data on GFDL hurricane model forecasts using global analyses. *Weather and Forecasting*, **12**, 307–323.

Vukicevic, T. and K. D. Raeder, 1995: Using Adjoint to find Triggers for Alpine Lee Cyclogenesis. *Monthly Weather Review*, **123**, 800–816.

Wang, B., R. L. Elsberry, Y. Wang, and L. Wu, 1998: Dynamics in tropical cyclone motion: A review. *Chinese Journal of Atmospheric Sciences*, **22**, 535–547.

Wang, Y. and C. C. Wu, 2004: Current understanding of tropical cyclone structure and intensity changes - A review. *Meteorology and Atmospheric Physics*, **87**, 257–278.

Wu, C. C. and H.-J. Cheng, 1999: An observational study of environmental influences on the intensity changes of typhoons Flo (1990) and Gene (1990). *Monthly Weather Review*, **127**, 3003–3031.

Xiao, Q., Y. Kuo, Z. Ma, W. Huang, X. Huang, X. Zhang, D. Barker, J. Michalakes, and J. Dudhia, 2008: Application of an adiabatic WRF adjoint to the investigation of the May 2004 McMurdo, Antarctica, severe wind event. *Monthly Weather Review*, **136**, 3696–3713.

Xu, M., D. J. Stensrud, J.-W. Bao, and T. T. Warner, 2001: Applications of the Adjoint Technique to Short-Range Ensemble Forecasting of Mesoscale Convective Systems. *Monthly Weather Review*, **129**, 1395–1418.

Zhang, X., X. Y. Huang, and N. Pan, 2013: Development of the upgraded tangent linear and adjoint of the weather research and forecasting (WRF) model. *Journal of Atmospheric and Oceanic Technology*, **30**, 1180–1188.